Progress in Energy and Combustion Science 70 (2019) 89–118

Contents lists available at ScienceDirect

Progress in Energy and Combustion Science

journal homepage: www.elsevier.com/locate/pecs

Forced response of laminar non-premixed jet flames

Nicholas Magina, Vishal Acharya, Timothy Lieuwen*

School of Aerospace Engineering, Georgia Institute of Technology, Atlanta, GA 30332-0150, USA

ARTICLE INFO

Article history:
Received 29 March 2018
Accepted 21 August 2018
Available online 22 October 2018

Keywords:
Laminar non-premixed flame
Linear velocity coupled flame response
Combustion instabilities
Flame transfer function

ABSTRACT

This paper reviews current understanding of the manner in which non-premixed jet flames respond to flow disturbances, and compares these characteristics to premixed flames. Disturbances in flow velocity excite wrinkles on non-premixed flame sheets and perturbations in heat release. These disturbances convect axially along the flame at the local flow velocity and decay in amplitude. Sufficiently large disturbance amplitudes cause opposing sides of the flame to merge and pinch off, leading to multiply connected flame sheets. The space-time characteristics of flame wrinkles on premixed and non-premixed flame sheets are quite similar, as they are dominated by flow disturbances moving the flame around, convection of the wrinkles downstream, and dissipation of wrinkles. In contrast, the heat release dynamics are quite different, as heat release oscillations in premixed flames are nearly uniformly distributed along the flame, whereas in non-premixed flames they are concentrated near the burner outlet where mixture fraction gradients are highest. In addition, flame area fluctuations are the dominant mechanism leading to heat release oscillations in constant burning velocity premixed flames, while mass burning rate oscillations dominate non-premixed flames. The flame transfer function, i.e., the normalized ratio of heat release and flow oscillations, is of O(1) at low frequencies and transitions to a $1/St$ behavior at high frequencies, for both premixed and non-premixed flames, where St denotes the flame Strouhal number, physically representing the ratio of the convective and the forcing time-scale. While the mechanisms dominating heat release oscillations are quite different for premixed and non-premixed flames, these comparable asymptotic tendencies are actually the result of the same effects; namely, that the heat release is proportional to the instantaneous mass flux of reactants in the quasi-steady, low Strouhal number case, and phase cancellation associated with convecting regions of oscillatory heat release leads to the $1/St$ behavior in the $St \gg 1$ regime. Non-premixed flames have an additional $1/\sqrt{St}$ transfer function character at an intermediate range of Strouhal numbers, due to the sharply varying axial dependence of mean heat release near the burner exit.

Contents

---

* Corresponding author.
E-mail address: tim.lieuwen@aerospace.gatech.edu (T. Lieuwen).

https://doi.org/10.1016/j.pecs.2018.08.001
0360-1285/

1. Introduction

This paper reviews current understanding of the response of non-premixed flames to harmonic flow perturbations. This work is motivated by the problem of combustion instabilities and combustion noise, where narrowband acoustic oscillations associated with acoustic modes of a combustor, couple with and excite heat release oscillations [1]. Further, reacting flows are often globally hydrodynamically unstable, and exhibit intrinsic oscillations associated with natural hydrodynamic instabilities associated with shear (e.g., Kelvin-Helmholtz instability), density gradients (e.g., Rayleigh-Taylor instabilities) or thermo-diffusive instabilities [1]. Fig. 1 shows images of the forced response of a mixing layer, clearly denoting the rollup of the shear layer.

The feedback loop during combustion instabilities is depicted schematically in Fig. 2. They have been encountered during the development and operation of various propulsion devices, power generation equipment, heating systems, and industrial furnaces, and are problematic because of the large amplitude pressure and velocity oscillations they produce. Having amplitudes that in some cases, specifically rocket applications, exceed several thousand *psi*, these oscillations can result in thrust oscillations, severe vibrations that interfere with control-system operation, enhanced heat transfer and thermal stresses to combustor walls, oscillatory mechanical loads that result in component fatigue, and flame blowoff or flashback [3]. Each of these issues may result in degraded system performance, unsatisfied product specifications, or premature component/system wear leading to costly shutdown or even catastrophic failure. Thus, improved understanding of combustion instabilities is helpful for developing efficient, safe, and reliable combustion systems.

This paper reviews the physics and understanding behind the dynamics, both in position and heat release, of non-premixed, momentum dominated jet flames responding to fluctuations in flow velocity. A great deal of literature on the linear and nonlinear response of premixed flames to flow disturbances and the combustion instability characteristics of lean, premixed combustors has been generated over the last decade [4–11]. Several review papers on premixed flame dynamics have appeared recently [5, 12–14], including experimental investigations of various nozzle and combustor configurations [9, 15–18], numerical simulations with detailed diffusion, chemistry and turbulence [19–21], and modeling efforts using the *G*-equation for fuel-air ratio, velocity, and pressure fluctuations [9, 11, 16, 18, 22–26]. As a result of this work, the controlling physics governing the forced response of laminar, premixed flames is quite well understood and capabilities have been developed to predict the space-time dynamics of the flame position and heat release [5, 27]. Furthermore, while some fundamental questions remain in highly turbulent flames regarding the spatio-temporal nature of narrowband and broadband disturbances and their interaction with the flame, exciting progress has been made in obtaining similar predictive capabilities in turbulent flows as well [26, 28–30].

In contrast, the behavior of non-premixed flames responding to flow disturbances, both in terms of the space-time reaction sheet dynamics, as well as the temporally varying heat release, both local and spatially integrated, is much less well understood. Nonetheless, there has been a recent increase in research addressing this topic, both from a modeling and experimental viewpoint. This collective intellectual advancement motivated the present review, whose objective is to synthesize these results and identify areas that need further attention for future work.

This review will specifically focus on the forced dynamics of gaseous non-premixed flames, and does not address the phenomenon of inherent non-premixed flame instabilities. As such, we briefly summarize these intrinsic instabilities of both isolated flame sheets, as well as that on non-premixed jet flames in Table 1, and show experimental examples in Fig. 3. Following Matalon [31] and Lieuwen [1], non-premixed flames exhibit intrinsic instabilities, manifested as stationary or time varying cellular flame structures, or even bulk flame oscillations. In premixed flames, both fluid mechanics and the coupling of the flame and flow by gas expansion play important roles in intrinsic instability. In contrast, intrinsic instabilities of non-premixed flames are controlled by thermal-diffusive effects. In other words, gas expansion processes quantitatively influence stability boundaries, but do not introduce new instability mechanisms. Rather, controlling mechanisms for intrinsic non-premixed flame instabilities arise from differential diffusion of mass and heat, leading to regions of excess or deficient enthalpy. Instability mechanisms are closely tied to the fact that non-unity Lewis number or mass diffusivity ratios lead to non-similar temperature and fuel/oxidizer concentration fields. For similar reasons, heat loss leads to intrinsic instabilities by causing non-similarity in thermal and concentration profiles.

In addition, non-premixed jet flames, used in many industrial hardware components, also exhibit intrinsic instabilities [34]. In the buoyancy dominated regime where the Froude number, $Fr = U_0^2/(gR_f)$, is not too high, these jet flames are globally unstable and exhibit narrowband oscillations, resulting from periodic vortical structures traveling along the flame, manifested as flame flicker at low frequency [35, 36]. This global instability disappears at small Froude numbers, or when the flame becomes momentum dominated at large Froude numbers [37]. Additional studies have investigated instability (oscillatory) onset and mitigation characteristics, with dependence upon Damköhler and Lewis numbers [31, 38, 39].

Having briefly considered intrinsic instabilities, we next return to externally forced flames, which are the focus of this review. External excitation of non-premixed flames, such as by acoustic forcing, has also been studied extensively, often with the motivation of enhancing mixing and/or decreasing pollutant emissions, for reasons discussed below. When subjected to external excitation, nominally unstable (lower Froude number) flames exhibit a variety of response features that depend upon the frequency and magnitude of the excitation. For example, Chen et al. studied an acoustically excited non-premixed flame [40], showing oscillations in both the fuel jet flow and flame sheet position, both of which were dependent upon the forcing frequency and amplitude. They and others [41-43] also showed nonlinear behavior, such as the presence of the sum and difference in frequencies of the buoyant instability and external forcing frequencies, subharmonics and harmonics of the excitation frequency, and frequency locking – i.e., the disap-

Nomenclature

$\mathcal{D}$	Diffusion coefficient
Fr	Froude number, $Fr = U_0^2/(gR_f)$
G	Premixed scalar
L_f	Flame length measured in flow direction
Ma	Markstein number
Pe	Peclet number, see Eq. (12)
$\dot{Q}$	Spatially integrated heat release rate oscillations, Eq. (57)
R_f	Radial distance to fuel lip, see Fig. 8
R_w	Radial distance to confining wall, see Fig. 8
St	Strouhal number based on fuel port half-width, $f\,R_f\,/\,U_0$
St_{Lf}	Strouhal number based on flame length, $f\,L_{f,0}\,/\,U_0$
St_p	Strouhal number definition for premixed flames, $St_{Lf}\,/\,\cos^2\theta$
St_ω	Strouhal number utilizing angular frequency, $\omega\,R_f\,/\,U_0$
St_1	St_{Lf} value at which the O(1) to $1/St^{1/2}$ asymptotic transition occurs
St_2	St_{Lf} value at which the $1/St^{1/2}$ to $1/St$ asymptotic transition occurs
U	Axial flow velocity
U_c	Wrinkle convection velocity, see Table 5
Y	Species mass fractions
$\mathcal{Z}$	Mixture fraction, see Eq. (3)
$\mathcal{Z}_{st}$	Stoichiometric mixture fraction value, see Table 3
$\mathcal{A}_n,\beta_-,\ \beta_h,r_n$	Solution eigenvalues
$\mathcal{F}$	Flame transfer function, Eq. (58)
Ψ	Scalar field
f	Frequency
f_f	Experimental forcing frequency
$\mathcal{f}$	Inflow profile, see Fig. 7
g	Gravitational acceleration
$\mathcal{h}_R$	Heat release per unit mass of reactant consumed
k	Helical convective disturbance wavenumber, $k = \omega/U_c$
k_c	Normalized disturbance phase speed, $k_c = U_c/U_0$
m	Helical mode number
m_s	Maximum local response helical mode number, see Eq. (47)
$\dot{m}''_F$	Reactant mass consumption rate per unit area
n	Coordinate normal to unforced flame front
q	Local distribution of heat release per unit area, Eq. (48)
r	Coordinate in the radial direction
s	Ratio of fuel port radius to wall radius, $R_f\,/\,R_w$
s_c	Flame consumption speed
s_d	Flame displacement speed
t	Time
u	Flow velocity
u_c	Convective velocity
w	Surface velocity with respect to the flow, see Eq. (1)
x	Coordinate in the flow direction; axial
y	Coordinate normal to the flow direction; transverse
z	Coordinate perpendicular to x-y plane
θ	Local angle of flame surface *wrt* axial coordinate, 2D see Fig. 9
ψ	Local angle of flame surface *wrt* axial coordinate, 3D see Fig. 22
Ω	Angular rate of swirl
∇	Gradient operator
α	Premixed flame aspect ratio, $\alpha = L_f/R_f = \cot\theta$
γ	Flame wrinkle dispersion coefficient, see Table 5
δ	Model piecewise linear inlet mixture fraction profile thickness, Fig. 7
ε	Small perturbation amplitude parameter
ζ	Flame wrinkle dissipation coefficient, see Table 5
η	Gain in η-τ model, Eq. (66)
λ	Wavelength corresponding to u, $u\,/\,f$
λ_c	Wavelength corresponding to u_c, $u_c\,/\,f$
σ_c	Markstein length
σ_C	Scaled Markstein length, Eq. (35)
$\hat{\sigma}_c$	Rescaled Markstein length, $\hat{\sigma}_c = \sigma_c\sin\theta\tan\theta$
ξ	Flame position measured in y- , r-, or n-direction, see Fig. 9
ρ	Density
σ	Non-dimensional swirl parameter, $\sigma = \Omega/\omega$
τ	Time-delay in η-τ model, Eq. (66)
φ_{ox}	Stoichiometric mass ratio of oxidizer to fuel
χ	Azimuthal interference parameter, see Eq. (46)
ω	Angular frequency, $2\pi\ f$
$(\ )_{st}$	Stoichiometric value
$(\ )_{x,y,\theta,r}$	Scalar components in x, y, θ, and r direction, respectively
$(\ )_{n,t}$	Scalar components in normal and tangential directions
$(\ )^u$	Unburned quantity
$(\ )_0$	Mean/steady state component
$(\ )_1$	Fluctuating component
$(\hat{\ })$	Frequency domain variable
$(\tilde{\ })$	Non-dimensional form of a variable
$(\vec{\ })$	Directional vector
$(\bar{\ })$	Time average
$\angle$	Phase of quantity

pearance of oscillations associated with the natural buoyant instability at sufficient excitation amplitudes. Williams et al. [44] explored this lock-in behavior, showing that forcing the fuel stream at a frequency close to the natural buoyant instability frequency was accompanied by the presence of large vortices on the air side of the flame, leading to large amplitude oscillations of the overall flame response at the forcing frequency. They also observed that a related lock-in phenomenon could happen at the first subharmonic of the forcing frequency, when the forcing frequency was close to twice the natural instability frequency. Juniper and co-workers [45, 46] conducted a detailed study on the lock-in phenomenon and quasiperiodic evolution of acoustically forced jet diffusion flames. They identified the critical amplitudes at which lock-in occur for a range of forcing frequencies around the natural instability frequency.

As a result of the strong effect of forcing on the ambient/co-flowing air and its entrainment with the fuel jet, a number of studies have also noted significant influences on soot and NOx production from the flame [47–59] – sensitivities which are much stronger in non-premixed flames than in premixed flames. For example, Saito et al. [47] showed that soot can be suppressed in

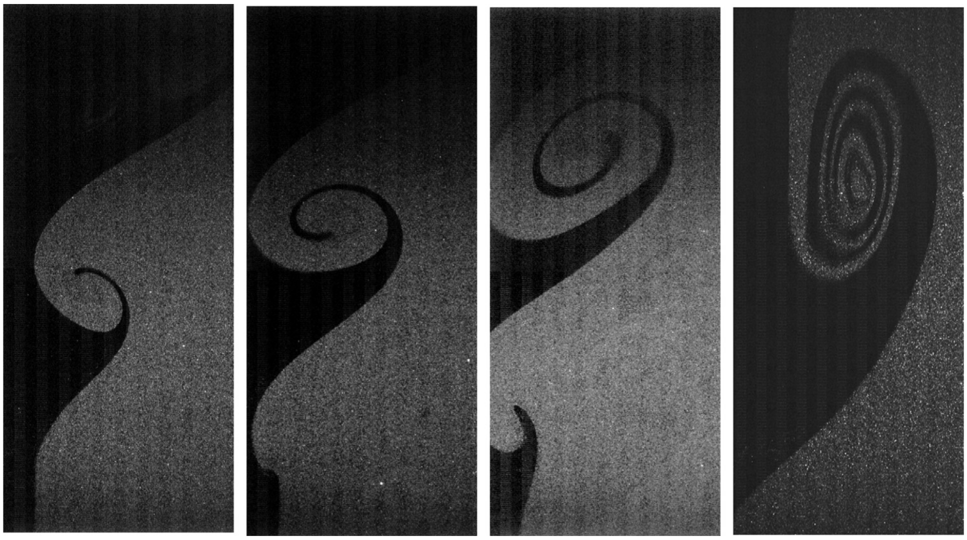

Fig. 1. Mie scattering images of a forced shear layer (taken from non-reacting experiments in the facility described in Magina et al. [2]). The first three images are at equal time intervals, while the last is from a delayed time where the roll-up has sufficiently evolved.

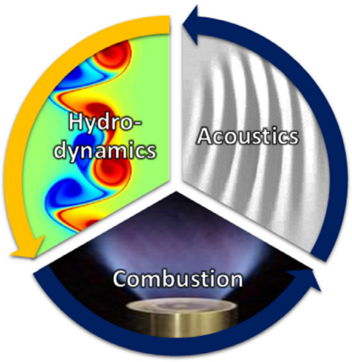

Fig. 2. Schematic depicting the combustion instability feedback loop.

acoustically excited non-premixed flames, with reductions of up to 50% in a laminar flame, and 90% for a turbulent flame.

In addition, several studies on forced counter-flow diffusion flames have analyzed the unsteady flame structure and flame response [60-62]. Finally, other forced flame studies have focused on the flame's space-time position dynamics due to velocity and equivalence ratio perturbations. The interaction between the acoustic field and the flame produces a spatially varying, oscillatory velocity component that is normal to the flame, causing wrinkling, as well as oscillatory reaction and heat release rates [50, 63]. Further, there are several experimental and numerical studies that examine the flow characteristics, flame dynamics, and mixing mechanisms of acoustically modulated jet diffusion flames [52, 56, 64–73].

The specific focus for this review paper is forced, non-premixed jet flames; particularly, the flame response and heat release dynamics. This review will not consider the combustor system dynamics (e.g., thermo-acoustic stability of combustor systems with non-premixed flames) where non-premixed flames are present, but note that an analytical and experimental literature exists on this topic, as well as an extensive wealth of industry experience in this area [74–77].

The review is organized as follows. Section 2 starts by investigating the governing features and properties of field and iso-surface dynamics. The mixture fraction governing equation, i.e. $\mathcal{Z}$-equation, is introduced and its features are compared with those of the premixed flame G-equation. Section 3 discusses the space-time dynamics of harmonically forced non-premixed flames through a series of model problems with increasing complexity. Section 4 presents a parallel discussion to Section 3, focusing on the heat release dynamics of these flames, including the low and high St asymptotic trends and transfer function characteristics. Finally, Section 5 summarizes key findings and highlights areas of needed future work.

2. Evolution of fields and iso-surface dynamics

While combustion always occurs over a distributed volumetric region, in many applications of interest its thickness is much smaller than other hydrodynamic and acoustic length scales, and so it can be treated as a surface, enabling the flame dynamics problem to be decoupled from that of its complex internal chemical kinetics. Flamelet models constitute one of the most common approaches for analyzing laminar and turbulent flames [97].

Table 1
Summary of sources of unsteadiness in gaseous, non-premixed flames.

Source of unsteadiness	Relative roles of buoyancy/momentum	References
Intrinsic instabilities - flame sheets		[1,31,39,78–81]
Intrinsic instabilities - jet flames	$Fr \leq O(1)$	[34–37, 82–84]
	$Fr > > 1$	[38,49,51,63,85]
Forced counterflow flames		[60–62]
Forced Jet Flames	$Fr \leq O(1)$	[32,41–44,47,64,65,69–71]
	$Fr > > 1$	[2,33,40,45,48,50,67,69,86–96]

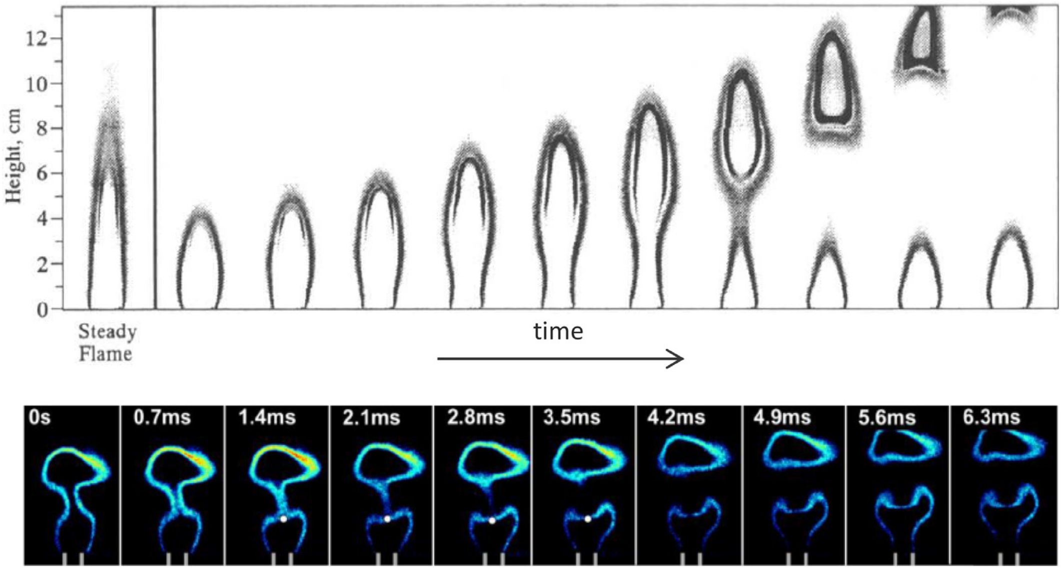

Fig. 3. (top) Experimental laser-induced fluorescence and soot scattering images in a steady and time-varying laminar CH_4/air diffusion flame that is undergoing intrinsic oscillations (reproduced from Shaddix et al. [32]) and (bottom) OH-PLIF of a forced H_2/CH_4 flame (Reprinted from Kim et al. [33] with permission from Elsevier).

Within the flamelet approximation, reactions are confined to a layer that is much thinner than other flow length scales, which may be substantially contorted and stretched by turbulent flow disturbances. For premixed systems, the flamelet surface separates unburnt reactants from burnt products, while for non-premixed systems it separates fuel and oxidizer–rich species. In the latter case, the flamelet occurs at the location where fuel and oxidizer diffuse into the flame sheet at a rate given by, and equivalently coexist at, their stoichiometric ratio.

This section discusses the dynamics and evolution of fields and isosurfaces, from both a general mathematical standpoint, and specifically for combustion related systems, and will closely follow the treatment of Pope [80]. Defining a general scalar field as Ψ, a surface can be defined implicitly, through an equation of the form $\Psi(\mathrm{X},t)=\Psi_{\mathrm{des}}$, or explicitly, as $\mathrm{X}\ (\vec{x},t)$, where the evolution of each respective entire surface is given by $\partial\Psi/\partial t$ or $\partial\mathrm{X}/\partial t$. Additionally, the evolution equation for the position of a surface is given by [80]:

$$\frac{d\mathrm{X}(\vec{x},t)}{dt}=\vec{u}\Big(X(\vec{x},t),t\Big)+w(\vec{x},t)\vec{n}(\vec{x},t) \tag{1}$$

where $\vec{u}$ is the velocity of the ambient medium, w is the velocity of the surface with respect to the flow, and $\vec{n}$ is the surface normal. From this, other various properties of the surface elements can be obtained, including the principal curvatures, principal directions, and the stretch factor [80]. The local geometry of surfaces is described by the spatio-temporal surface element properties, consisting of position, surface normal direction, principal curvatures, and fractional area increase.

We can define three types of surfaces, namely - *material* surfaces, *propagating* surfaces, and *constant-property* surfaces. A *material* surface (e.g. surface of passive tracer particles) is a passive interface between two fluids that is advected by the flow, $\vec{u}$. A *propagating* surface (e.g. premixed flame) is a surface which propagates normal to itself at a given velocity relative to the fluid. This relative propagation velocity, w, is referred to as the displacement speed, s_d, for premixed flamelets. A *constant-property* surface (e.g. non-premixed flame) is a surface where some given property, Ψ, is constant. Non-premixed flame sheets occur along the constant property surface where the mixture fraction, Z, has its stoichiometric value, $Z=Z_{st}$.

Following Pope [80], a helpful way to compare and contrast these three types of surfaces is to recast the surface dynamics of one surface type into the other, as shown in Table 2. For example, a constant property surface is defined as an isoΨ surface, but can alternatively be considered as a propagating surface with front velocity relative to the flow given by $w=-(D\Psi/Dt)/|\nabla\Psi|$.

For both a material surface or propagating surface with constant w, the evolution of any surface element is fully described for a given velocity field and initial condition, and thus each surface element evolves independently. However, the temporal evolution of any surface element of a constant property surface is controlled by the entire property field at each instant [80]. This has important implications for the solution methods, since rather than considering evolution equations for a constant-property surface, an alternative approach is to deduce the surface properties from the property field and its evolution [80].

Consider a surface that is initially (1) "regular", defined as having finite curvature everywhere with no-self intersections, critical points, or cusps [98], and (2) simply-connected, defined as having no fully penetrating holes passing through it. A material and constant-property surface remains regular during its evolution, while a propagating surface can develop singularities, i.e. values of infinite local curvature, and self-intersections [80]. For premixed flames, this manifests itself as the formation of cusps, shown in Fig. 4– i.e. discontinuities in flame slope for constant w (s_d) flames [4]. As will be seen later, external forcing complicates (yet still follows) this behavior, producing multi-connected, i.e. segregated, material surfaces and constant-property surfaces; a feature known as flame clipping for non-premixed flames, which occurs under certain critical conditions.

In addition to the local properties discussed, the evolution equations for global properties of level surfaces can also be expressed [100]. This is of particular interest for combustion systems, as total heat release and surface area are significant dynamical parameters of interest. The nature of the resulting equation to be established will be kinematic, expressing the time rate of change of global variables in terms of the progression velocity and geometric parameters of the level surface. A global variable can be defined as:

$$\mathrm{Y}_{\Psi}(\Psi,t)\equiv\oint_{\Psi}f(\vec{x},t)dA(\vec{x}) \tag{2}$$

Table 2
Uniform casting of material, propagating, and constant property surfaces, following Pope [80], where Ψ_0 is a specified value.

	Treated as a Propagating Surface with...	Treated as a Constant Property Surface with...
Material Surface	$w = 0$	$\frac{D\Psi}{Dt} = 0$
Propagating Surface	$w = s_d$ (controlled by internal flame structure)	$\frac{D\Psi}{Dt} = -w\lvert\nabla\Psi\rvert$
Constant-Property Surface	$w = -\frac{D\Psi}{Dt} / \lvert\nabla\Psi\rvert$	$\Psi = \Psi_0$

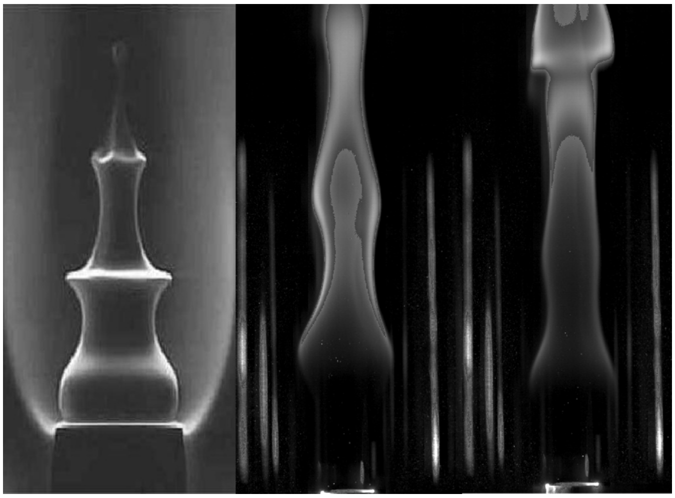

Fig. 4. Schlieren image of a conical methane-air forced premixed flame at 150 Hz (left) (reproduced from Ducruix et al. [99]) along with line of sight luminosity images of forced methane-air non-premixed flames at 30 Hz (middle) and 50 Hz (right) forcing frequency (Reprinted from Magina et al. [2] with permission from Elsevier).

Table 3
Stoichiometric mixture fraction for hydrogen and various hydrocarbon fuels in air and oxygen.

Fuel	$\mathcal{Z}_{st}$ ***value in air***	$\mathcal{Z}_{st}$ ***value in oxygen***
CH_4	$\mathcal{Z}_{st} = 0.055$	$\mathcal{Z}_{st} = 0.200$
C_3H_8	$\mathcal{Z}_{st} = 0.060$	$\mathcal{Z}_{st} = 0.216$
C_8H_{18}	$\mathcal{Z}_{st} = 0.063$	$\mathcal{Z}_{st} = 0.222$
H_2	$\mathcal{Z}_{st} = 0.029$	$\mathcal{Z}_{st} = 0.112$

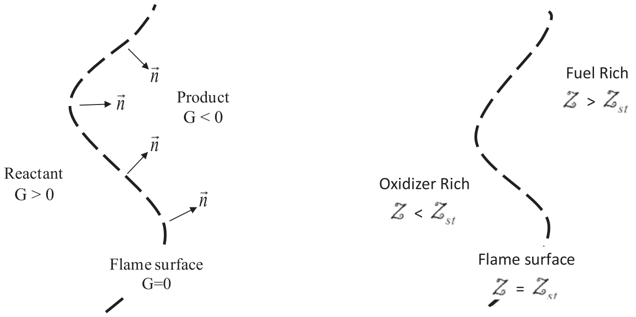

Fig. 5. Schematic of the premixed G-field (left) and non-premixed $\mathcal{Z}$-field (right) with denoted isocontours representing the flame sheet.

where $f(\vec{x}, t)$ denotes a scalar of Ψ, and is a smooth function of location and time. This global variable concept will be elaborated upon in Section 4.

2.1. Field equations for premixed and non-premixed flames

Virtually all analytical work on non-premixed flame dynamics has utilized the Shvab-Zeldovich mixture fraction formulation, due to its analytical tractability in the absence of source terms, and we shall follow this framework in this section. The mixture fraction is defined as the mass ratio of material at each spatial location having its origin in the fuel stream, i.e., $\mathcal{Z} = \mathcal{Z}(\vec{x}, t)$. Thus, $\mathcal{Z}$ takes values of zero and unity in the pure oxidizer and pure fuel streams, respectively, and is given for a simplified three-species system (consisting of fuel and oxidizer reacting to form a single product), by:

$$\mathcal{Z} = Y_F + \frac{Y_{\mathrm{Pr}}}{(\varphi_{ox} + 1)} \tag{3}$$

where φ_{ox} is the stoichiometric oxidizer-to-fuel ratio. A foundation for the analytical work, the governing equation for the mixture fraction has no source term if all species have equal diffusivity coefficients, $\mathcal{D}$, and is given by:

$$\rho\frac{D\mathcal{Z}}{Dt} - \nabla \cdot (\rho\mathcal{D}\nabla\mathcal{Z}) = 0 \tag{4}$$

To solve this equation, the density must be related to the mixture fraction. The simplest approach to proceed is to assume an isodensity field, although certainly an oversimplification for combustion applications. However, rather than assuming constant density, the less restrictive assumption of constant $\rho\mathcal{D}$ can be utilized (although it actually varies as $T^{1/2}$ for perfect gases). The final modified form of the mixture fraction equation, to be referred to throughout this work as the $\mathcal{Z}$-equation, is given by:

$$\frac{\partial\mathcal{Z}}{\partial t} + \vec{u} \cdot \nabla\mathcal{Z} = \mathcal{D}\nabla^2\mathcal{Z} \tag{5}$$

Consistent with Table 2, the flame lies on the locus of points, defining the flame sheet, given by the parametric equation $\mathcal{Z}(\vec{x}, t) = \mathcal{Z}_{st}$. Typical representative $\mathcal{Z}_{st}$ values are shown in Table 3.

For premixed combustion the mixture fraction is uniform everywhere, assuming equi-diffusive species, and thus a similar conservation equation would provide no new information. Rather, the G-equation is used for premixed flames in the reaction sheet limit [5, 101, 102], given by:

$$\frac{\partial G}{\partial t} + \vec{u} \cdot \nabla G = s_d\lvert\nabla G\rvert \tag{6}$$

The flame lies on the locus of points, defining the flame sheet, given by the parametric equation $G(\vec{x}, t) = 0$. Both of these flame front kinematic equations relate the motion of the flame front with various flow/flame parameters implicitly, meaning the flamelet is treated as a gas dynamic discontinuity in three-dimensional space described by a specific isosurface. Simple schematics of the two fields are shown in Fig. 5.

It is helpful to compare the dynamics and governing features of the $\mathcal{Z}$-equation, given by Eq. (5) for non-premixed flames, with the G-equation, given by Eq. (6) for premixed flames. The two expressions have the same convection operator on the left-hand side which illustrates the importance of flow perturbations in the direction normal to the flame sheet in moving the flame sheet around. However, the right-hand sides of these two expressions are different; the premixed flame expression has the normal flame propagation operator, $s_d\lvert\nabla G\rvert$, while the non-premixed flame expression has a diffusion operator, $\mathcal{D}\nabla^2\mathcal{Z}$. This difference is significant and reflects, among other things, the fact that non-premixed flames

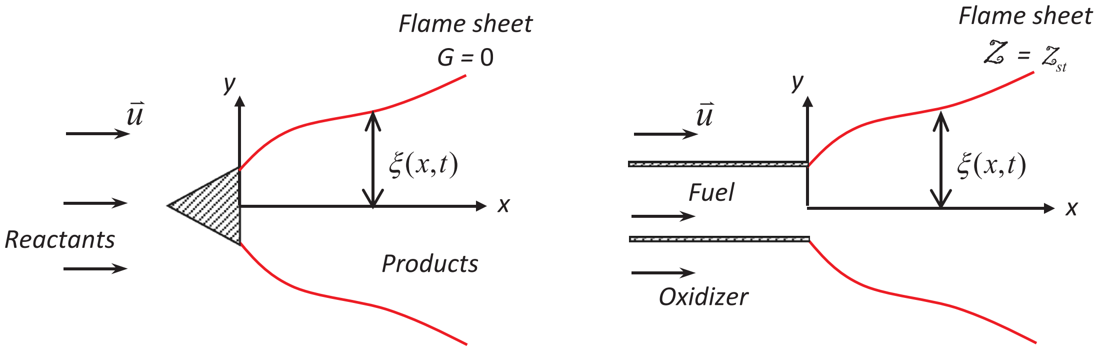

Fig. 6. Schematic of bluff-body stabilized premixed flame (left) and jet non-premixed flame (right) with its corresponding coordinates and flame front dynamical parameter, $\xi(x,t)$.

do not propagate. Moreover, this propagation term makes the premixed flame dynamics equation nonlinear, while the non-premixed flame dynamics equation is linear (assuming $\vec{u}$ and $\mathcal{D}$ are not functions of $\mathcal{Z}$).

Another significant, yet subtle, difference is that the G-equation is physically meaningful and valid *only* at the flame itself where $G(\vec{x},t) = 0$ (i.e., although it can be solved away from the flame, the resulting G values have no physical significance [103]). In contrast, the $\mathcal{Z}$-equation describes the physical values of the mixture fraction field *everywhere*. This point was alluded to earlier as well for constant property surfaces, whose dynamics are determined by the instantaneous property field, rather than simply the velocity at the surface. Thus, the entire mixture fraction field must be solved in the non-premixed problem and the $\mathcal{Z}(\vec{x},t) = \mathcal{Z}_{st}$ surface extracted from the resulting solution field (which generally cannot be expressed explicitly). Consequently, developing explicit solutions for the non-premixed flame problem is not as straightforward as for the premixed problem. This observation has important consequences for both solution approaches of these problems, as well as the $\mathcal{Z}(\vec{x},t) = \mathcal{Z}_{st}$ flame sheet dynamics that are discussed next.

Consider next the case where the flame position is a single valued function of some coordinate. For example, in the two-dimensional case, the instantaneous position of the reaction sheet is given by $y = \xi(x, t)$, shown in Fig. 6 for representative two-dimensional premixed and non-premixed systems.

A useful transformation of the G-equation can be done by expressing Eq. (6) in terms of the flame position, ξ, through use of the substitution $G(x, y, t) = y - \xi(x, t)$. Although the resulting equation for the flame position becomes less general (being only valid for a flame whose position is single-valued), it enables an explicit governing equation for the flame position dynamics. With these explicit expressions dynamical quantities, such as flame surface area fluctuations and flame curvature, can be obtained and investigated. Implementing this transform yields the following explicit expression for the premixed flame position:

$$\frac{\partial \xi}{\partial t} + u_x \frac{\partial \xi}{\partial x} - u_y = s_d \sqrt{1 + \left(\frac{\partial \xi}{\partial x}\right)^2} \tag{7}$$

Note that the substitution for G arbitrarily assigns values to the G field away from the flame itself, namely that G varies linearly with coordinate y away from the flame. Since the G field is completely arbitrary away from the flame this is allowable, however, we cannot make an analogous substitution for the non-premixed system, such as $\mathcal{Z}(\vec{x},t) - \mathcal{Z}_{st} = y - \xi(x,t)$, as this assigns values to the $\mathcal{Z}$ field away from $\mathcal{Z}(\vec{x},t) = \mathcal{Z}_{st}$. As mentioned earlier, unlike the G-equation which is valid *only* at the flame front, the $\mathcal{Z}$-equation describes the *entire* spatial distribution of the mixture fraction field.

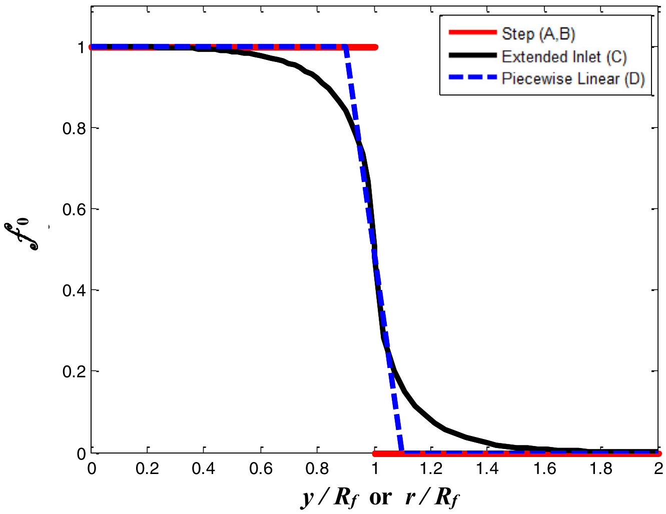

Fig. 7. Model problem steady inlet mixture fraction profiles, f_0, for the analytically imposed step (Table 4A, Table 4B), computed extended inlet (Pe= 10, Table 4C), and analytically imposed piecewise linear smoothed profile (Table 4D), where the mixture fraction transition occurs linearly over a non-dimensional distance δ. Transverse and radial coordinate y and r utilized for the 2D and 3D problems, respectively.

This discussion reflects important underlying physics of the two flames. Consider a premixed and non-premixed flame embedded in a velocity field given by $\vec{u}(x,y,z,t)$, where the velocity field at the flame sheet is given by $\vec{u}(x,\xi(x,z,t),z,t) = \vec{u}^u$. The premixed flame dynamics are only a function of $\vec{u}^u$; this implies that for a given $\vec{u}^u$, its space-time dynamics are the same for a variety of different velocity fields. In contrast, the space-time dynamics of the non-premixed reaction sheet are a function of the entire velocity field, $\vec{u}(x,y,z,t)$, not just its value at the reaction sheet.

2.2. Description of model problems

In this review, we shall present multiple model problems, with increasing levels of complexity, in order to understand and isolate the effects of different physics. These model problems are summarized in Table 4 and will be detailed further in the section where they are first introduced. The key differences between these model problems is their inclusion of axial diffusion, as well as the transverse profiles of the steady state mixture fraction at the burner exit, i.e. $\mathcal{Z}_0(x=0)$. The various steady inflow profiles utilized, denoted as $f_0(y) = \mathcal{Z}_0(x=0, y)$, are shown in Fig. 7.

Table 4
Model problems and boundary description.

Model problem identification	Axial diffusion included in governing equation?	Inflow boundary condition (see Fig. 7)
A	No ($b=0$ in Eq. (10))	Step profile, see Fig. 8 and Eq. (8)
B	Yes ($b=1$ in Eq. (10))	Step profile, see Fig. 8 and Eq. (8)
C	Yes ($b=1$ in Eq. (10))	Extended inlet, see Fig. 20
D	No ($b=0$ in Eq. (10))	Smoothed profile over transition distance, δ

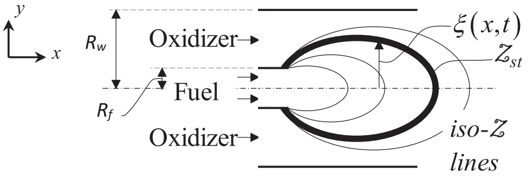

Fig. 8. Schematic of the forced two-dimensional non-premixed flame model problem.

3. Space-Time dynamics of the reaction sheet

This section examines the basic dynamical characteristics of a non-premixed flame responding to harmonic flow perturbations. We focus on the flame position in this section, and the integrated heat release in Section 4. This section is organized by first presenting a basic model problem – the response of a non-premixed flame to bulk, harmonic forcing. This analysis utilizes a variety of simplifying assumptions in order to allow for analytically tractable explicit expressions for the flame position. While additional effects like non-isothermal heat release and spatial temperature gradients are neglected in this model problem, it enables us to describe some key physics which will be seen in computations and experiments presented later that include these neglected effects.

3.1. Two-dimensional bulk axial forcing - Model Problem A

This section presents the results of a model problem to illustrate key physics that influence the spatiotemporal flame dynamics. It closely follows the analysis from a suite of analytical studies which have also considered the response of non-premixed flames [87-93]. This work builds from the significant theoretical literature on the unforced problem, such as the Burke-Schumann flame [49, 81, 104].

As discussed in Section 2.1, the $\mathcal{Z}$-equation is utilized for this formulation, with accompanying key assumptions of infinitely fast chemistry, wherein the flame sheet collapses to the $\mathcal{Z}_{st}$ surface, equal species diffusivities, constant diffusion coefficients, specified disturbance fields, and small perturbation amplitudes (see Miklavčič [94] for recent generalization of this work to include finite amplitudes). As such, the space-time dynamics of a non-premixed flame can be described by the mixture fraction field using the $\mathcal{Z}$-equation, Eq. (5). The steady and fluctuating velocity fields are imposed, thus decoupling the momentum equation from the energy and species equations; this, however, implicitly assumes an isothermal field.

Consider first a two-dimensional flame as depicted in Fig. 8, in a uniform axial flow field whose value in the absence of forcing is given by U_0. At the inlet, i.e. $x=0$, fuel and oxidizer flow into the domain as indicated in the figure, leading to the following step inflow conditions:

$$\mathcal{Z}(x=0,y)=\begin{cases}1 & \text{for } 0\le |y| <R_f\\ 0 & \text{for } R_f\le |y| <R_w\end{cases} \tag{8}$$

Enforcing this boundary condition enables an analytic solution of the problem. In reality, however, there is transverse diffusion of fuel just downstream of the inlet followed by axial diffusion of fuel into the oxidizer port and vice versa, so that the solution must actually be solved over a larger upstream domain that includes the fuel/oxidizer supply systems [95]; this effect is captured and investigated in Model Problem C in Section 3.3. As such, the boundary condition in Eq. (8) implicitly neglects axial diffusion at $x=0$, a point which will be returned to in Section 3.3. Assuming symmetry at $y=0$, no penetration through the walls at $y=R_w$, and requiring finite mixture fraction values throughout makes this boundary value problem fully defined.

For analytical tractability, the solution is derived in the limit of small perturbations, and thus each variable is expanded as $(\ )(x, y, t) = (\ )_0(x, y) + (\ )_1(x, y, t)$. Neglecting higher order terms, the unforced mixture fraction field, for a system with no transverse flow, i.e. $u_{y,0}=0$, can be acquired from Eq. (5) as:

$$U_0\frac{\partial \mathcal{Z}_0}{\partial x}=\mathcal{D}\frac{\partial^2 \mathcal{Z}_0}{\partial y^2}+b\mathcal{D}\frac{\partial^2 \mathcal{Z}_0}{\partial x^2} \tag{9}$$

where the velocity scalar $u_{x,0}=U_0$ is the spatially constant axial flow velocity and "b" is an axial diffusion indicator, taking values of unity and zero, depending upon whether axial diffusion effects are included or neglected, respectively (see Table 4); this will be elaborated on in Section 3.3. Similarly, the dynamical equation for the fluctuating mixture fraction field can be obtained from Eq. (5) and written in the frequency domain (indicated with an overhat $(\widehat{\ })$) as:

$$-i\omega\hat{\mathcal{Z}}_1+U_0\frac{\partial \hat{\mathcal{Z}}_1}{\partial x}-\mathcal{D}\frac{\partial^2 \hat{\mathcal{Z}}_1}{\partial y^2}-b\mathcal{D}\frac{\partial^2 \hat{\mathcal{Z}}_1}{\partial x^2}=-\hat{u}_{x,1}\frac{\partial \mathcal{Z}_0}{\partial x}-\hat{u}_{y,1}\frac{\partial \mathcal{Z}_0}{\partial y} \tag{10}$$

The solution to these equations can be derived using separation of variables. The full solution, including axial diffusion ($b=1$), for the steady state mixture fraction field, i.e. Eq. (9), utilizing Eq. (8) as the inlet condition, is given by:

$$\mathcal{Z}_0=\frac{R_f}{R_w}+\sum_{n=1}^{\infty}\frac{2}{n\pi}\sin(\mathcal{A}_n)\cos\left(\mathcal{A}_n\frac{y}{R_f}\right)\exp\left(\frac{x}{PeR_f}\left[\frac{Pe^2-\sqrt{Pe^4+4Pe^2\mathcal{A}_n{}^2}}{2}\right]\right) \tag{11}$$

where $\mathcal{A}_n=n\pi(R_f/R_w)$ are the eigenvalues and the Peclet number, Pe, is given by the expression:

$$Pe=\frac{U_0R_f}{\mathcal{D}} \tag{12}$$

physically corresponding to the relative time scales for convective and diffusive processes to transport mass over a distance R_f.

The subsequent analysis will focus on a simplified version of the solution that neglects axial diffusion, since we have already done so implicitly in formulating the boundary condition in Eq. (8). Denoted Model Problem A in Table 4, the resulting steady state mixture fraction field solution is given by:

$$\mathcal{Z}_0=\frac{R_f}{R_w}+\sum_{n=1}^{\infty}\frac{2}{n\pi}\sin(\mathcal{A}_n)\cos\left(\mathcal{A}_n\frac{y}{R_f}\right)\exp\left(-\mathcal{A}_n{}^2\frac{x}{PeR_f}\right) \tag{13}$$

and can be derived by solving Eq. (9) and neglecting the axial diffusion term, i.e. setting $b=0$, or equivalently, taking the $Pe\to\infty$ limit of Eq. (11).

Consider next the solution for the fluctuating flame position responding to uniform bulk axial fluctuations in flow velocity,

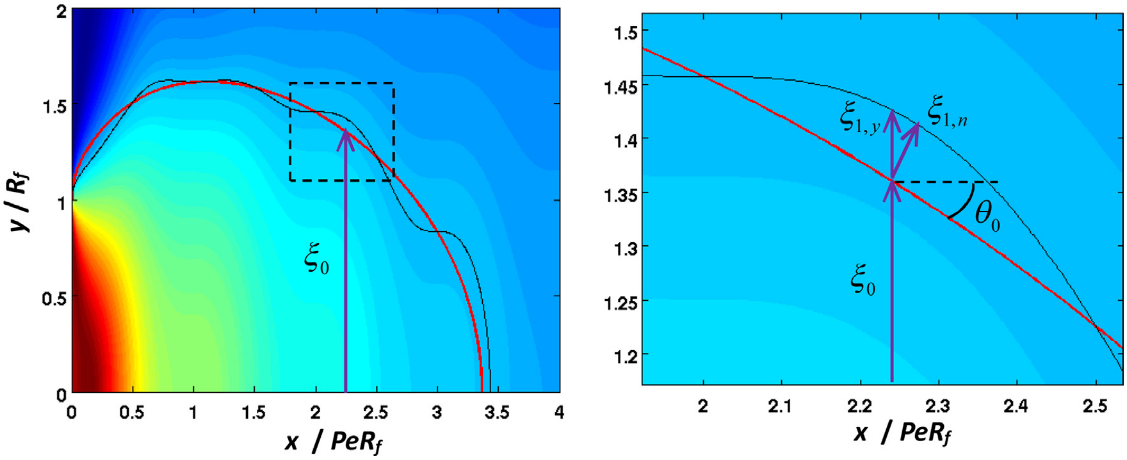

Fig. 9. Representative two-dimensional non-premixed flame mixture fraction field (left) with steady state (red) and instantaneous (black) flame sheet location denoted. A close-up view of a "flame wrinkle" (right) shows the steady, $\xi_0(x)$, and fluctuating wrinkle location denoted radially, $\xi_{1,y}(x,t)$, and normally to the mean flame, $\xi_{1,n}(x,t)$. The mean flame angle, $\theta_0(x)$, is also denoted.

$u_{x,1} = \varepsilon\, U_0 \exp[-i\omega t]$. The resulting full solution for the fluctuating mixture fraction field, $\mathcal{Z}_1$, is:

$$\mathcal{Z}_1 = \sum_{n=1}^{\infty}\left[\frac{2/(n\pi)\sin(\mathcal{A}_n)\varepsilon\beta_-}{2\pi\, i Pe St}\right]\cos\left(\mathcal{A}_n\frac{y}{R_f}\right)\left\{\exp\left(\frac{x}{PeR_f}\beta_-\right)-\exp\left(\frac{x}{PeR_f}\beta_{h-}\right)\right\}\exp[-i\omega t] \quad (14)$$

where the Strouhal number based on the half-width of the fuel nozzle is defined by $St = fR_f/U_0$, and

$$\beta_- = \frac{Pe^2-\sqrt{Pe^4+4Pe^2\mathcal{A}_n{}^2}}{2} \qquad \beta_{h-} = \frac{Pe^2-\sqrt{Pe^4+4Pe^2\mathcal{A}_n{}^2-8\pi i Pe^3 St}}{2} \quad (15)$$

Again, we will focus the subsequent analysis in the absence of axial diffusion, i.e. in the $Pe\to\infty$ limit, whose solution is:

$$\mathcal{Z}_1 = \sum_{n=1}^{\infty}\left[\frac{i\varepsilon\mathcal{A}_n{}^2(2/n\pi)\sin(\mathcal{A}_n)}{2\pi\, St\, Pe}\right]\cos\left(\mathcal{A}_n\frac{y}{R_f}\right)\exp\left(-\mathcal{A}_n{}^2\frac{x}{Pe\,R_f}\right)\left\{1-\exp\left(2\pi\, i St\frac{x}{R_f}\right)\right\}\exp[-i\omega t] \quad (16)$$

Alternatively, this expression can also be written in terms of $\mathcal{Z}_0$ as:

$$\mathcal{Z}_1 = \left[\frac{-i\varepsilon R_f}{2\pi\, St}\right]\frac{\partial\mathcal{Z}_0}{\partial x}\left\{1-\exp\left(2\pi\, i St\frac{x}{R_f}\right)\right\}\exp[-i\omega t] \quad (17)$$

Representative solutions are shown in Fig. 9. The reaction sheet is defined by the locus of points where $\mathcal{Z}(x, y=\xi(x,t), t) = \mathcal{Z}_{st}$. Note, the flame position, $\xi(x,t)$, is implicitly contained in this expression. Expanding this implicit equation for the fluctuating flame in terms of $\mathcal{Z}$and $\xi(x,t)$, to first order, results in:

$$\mathcal{Z}_0(x, y=\xi_0(x)+\xi_{1,n}(x,t)) + \mathcal{Z}_1(x, y=\xi_0(x)+\xi_{1,n}(x,t), t) = \mathcal{Z}_{st} \quad (18)$$

while subsequently expanding this equation in a Taylor-series yields:

$$\mathcal{Z}_0(x, y=\xi_0(x)) + \xi_{1,n}(x)|\nabla\mathcal{Z}_0(x, y=\xi_0(x))| + \mathcal{Z}_1(x, y=\xi_0(x), t) + O(\varepsilon^2) = \mathcal{Z}_{st} \quad (19)$$

Grouping the leading order terms results in the following implicit equation for the steady flame position:

$$\mathcal{Z}_0(x, y=\xi_0(x)) = \mathcal{Z}_{st} \quad (20)$$

while the first order terms lead to the following *explicit* expression for fluctuating flame position:

$$\xi_{1,n}(x,t) = -\frac{\mathcal{Z}_1(x, y=\xi_0(x), t)}{|\nabla\mathcal{Z}_0(x, y=\xi_0(x))|} \quad (21)$$

The perturbation in flame position can be measured radially or normally to the mean flame surface in the direction of the oxidizer, as shown in Fig. 9. Generally, throughout this work, the normal displacement, i.e. $\xi_{1,n}$, is utilized for quantifying flame motion due to the substantial change in the angle of the reaction sheet with axial location (in contrast, if flame motion is measured as radial displacement, its value at the flame tip becomes ambiguous, potentially taking infinite values).

An implicit expression for the flame sheet position, $\xi_0(x)$, can be determined from Eq. (20), yielding:

$$\mathcal{Z}_{st} = \frac{R_f}{R_w} + \sum_{n=1}^{\infty}\frac{2}{n\pi}\sin(\mathcal{A}_n)\cos\left(\mathcal{A}_n\frac{\xi_0(x)}{R_f}\right)\exp\left(-\mathcal{A}_n{}^2\frac{x}{PeR_f}\right) \quad (22)$$

Similarly, from Eq. (21), the position of the fluctuating flame can be written as:

$$\frac{\xi_{1,n}(x,t)}{R_f} = \left(\frac{\partial\mathcal{Z}_0/\partial x}{|\nabla\mathcal{Z}_0|}\right)_{(x,y=\xi_0(x))}\left[\frac{i\varepsilon}{2\pi\, St}\right]\left\{1-\exp\left(2\pi\, i St\frac{x}{R_f}\right)\right\}\exp[-i\omega t] \quad (23)$$

From here, the $(\partial\mathcal{Z}_0/\partial x)/|\nabla\mathcal{Z}_0|$ term can be written in terms of the local angle of the flame, using the geometric relation:

$$|\nabla\mathcal{Z}_0| = \left[\left(\frac{\partial\mathcal{Z}_0}{\partial x}\right)^2+\left(\frac{\partial\mathcal{Z}_0}{\partial y}\right)^2\right]^{1/2} = \frac{\partial\mathcal{Z}_0/\partial x}{\sin\theta_0(x)} \quad (24)$$

where θ_0 denotes the angle of the mean flame with respect to the axial coordinate (as shown in Fig. 9). Using these results, and a modified definition for Strouhal number for ease of comparison ($St_{L_f} = L_{f,0}/R_f \times St$), the solution for $\xi_{1,n}(x,\ t)$ can be written as [92]:

$$\xi_{1,n}(x,t) = \frac{i\varepsilon U_0}{2\pi f}\sin\theta_0(x)\left\{1-\exp\left(i2\pi St_{L_f}\frac{x}{L_{f,0}}\right)\right\}\exp[-i2\pi ft] \quad (25)$$

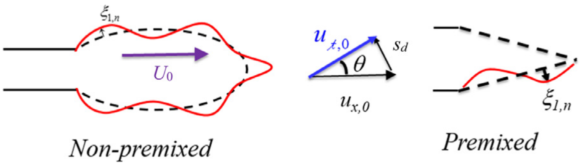

Fig. 10. Schematics depicting the difference in wrinkle convection speed for non-premixed and premixed flame systems.

For reference, the corresponding fluctuations of an attached premixed flame with constant burning velocity subjected to bulk flow oscillations are given by [105]:

$$\xi_{1,n}(x,t) = \frac{i\varepsilon U_0}{2\pi f}\sin\theta\left\{1-\exp\left(i2\pi St_p\frac{x}{L_{f,0}}\right)\right\}\exp\left[-i2\pi ft\right] \tag{26}$$

where St_p is the flame Strouhal number for premixed flames, defined as $St_p = St_{L_f}/\cos^2\theta$, and the flame angle, θ, is a constant (the expression is more involved if θ is varying, which would occur if the flow or flame speed varies spatially).

3.2. Model problem results and experimental data - Discussion

This section discusses the key physics embodied in the solutions derived in Section 3.1, as well as comparison of these results with measurements. Due to the similarities in the expression for the premixed and non-premixed flame, the equations are discussed comparatively. Note first that both expressions are multiplied by an amplitude term of the form, $(\varepsilon U_0/2\pi f)\times\sin\theta$. This is equal to $|u_{1,n}|\ /\ 2\pi f$; i.e., the magnitude of the velocity fluctuations normal to the flame, divided by the frequency. Thus, the flame sheet fluctuations act as a low pass filter and the sinθ term simply converts the axial velocity fluctuation into the component normal to the flame sheet. Likewise a cosθ term appears if the flame is transversely forced [93]. Note that the particle displacement associated with a velocity fluctuation of magnitude $|u_1|$ at a frequency of f is given by $|u_1|\ /\ 2\pi f$, showing that this low pass filter characteristic is simply a manifestation of the reduced particle displacement for a given magnitude velocity fluctuation with increasing frequency. Referring back to the formulating assumptions of Eq. (5) in Section 2.1, note that differential diffusion effects would alter the time averaged flame shape, which implicitly influences its response through the local flame angle and flame length. It is not clear whether it introduces additional explicit effects on the flame response to disturbances [106].

Both expressions also contain a term of the form, $1-e^{i2\pi fx/U_0}$; the first term which describes spatially invariant bulk fluctuations, arises from the homogeneous boundary condition (i.e., no flame position fluctuation at $x=0$ which is implicitly imposed by Eq. (8)), while the second describes downstream convection of wrinkles whose axial speed is equivalent to the axial mean flow. The primary difference in the premixed and non-premixed solutions is contained within this waveform term, and reflects the influence of premixed flame propagation on wrinkle convection speeds. The non-premixed flame does not propagate, and wrinkles convect axially downstream at the bulk flow speed, U_0. In contrast, wrinkles on the premixed flame convect in the axial direction at the speed $U_0/\cos^2\theta$, which is the vector superposition of the axial flow velocity and the axial projection of a vector pointing normal to the flame (into the reactants) with a magnitude equal to the burning velocity, s_d, as is depicted in Fig. 10.

In both cases, local maxima and minima arise through this $1-e^{i2\pi fx/U_0}$ waveform term,[1] due to interference between wrinkles generated at the $x=0$ boundary and disturbances excited locally.

$$1-e^{i2\pi fx/U_0} = 2\sin\left(\pi fx/U_0\right)e^{i(\pi fx/U_0-\pi/2)} \tag{27}$$

For both premixed and non-premixed flames, wrinkles are generated at the boundary because of flame attachment. For the premixed flame, this is invoked directly through the attachment boundary condition i.e., $\xi_{1,n}(x=0,\ t)=0$. In the non-premixed case, wrinkles are generated through the assumption of constant mixture fraction at the burner outlet, i.e., $\mathcal{Z}_1(x=0,\ t)=0$. This assumption will be relaxed in Model Problem C.

We next present several illustrative solutions of the space-time dynamics for the flame position. Note that the solution is a function of the four dimensionless parameters St_{Lf}, $R_f\ /\ R_w$, Pe, and $\mathcal{Z}_{st}$. Although only St_{Lf} appears directly in Eq. (25), the others are concealed and influence through the sinθ term, as demonstrated by Eq. (24). The temporal evolution of the flame position is plotted in Fig. 11 at two representative Strouhal numbers. Note the bulk axial pulsing of the flame at lower Strouhal numbers, and the presence of multiple spatial wrinkles within the flame length at higher values. The unforced flame is indicated by the dashed lines.

Mohammed et al. [50] have reported measurements and computations of a forced CH_4-air diffusion flame, which are reproduced in Fig. 12 (left). In this experiment, only the fuel flow rate was perturbed, as opposed to both fuel and air flow oscillations in these calculations. However, it is still useful to compare results, using conditions that approximately simulate those from the experiment. Fig. 12 (right) shows calculations of the unsteady flame position at several instants over a forcing cycle for similar conditions. Similar bulk axial pulsing of the flame is evident in the measurements.

An alternative way to visualize these results is through the magnitude and phase of $\xi_{1,n}$, illustrated in Fig. 13. The nodes and local maxima and minima referred to above are clearly evident in the figure. The phase rolls off linearly with axial distance, again reflecting the convection process described by the interference waveform term in Eq. (27), and jumps 180° across the nodes.

These results can be qualitatively compared with the experimental results of Magina et al. [2] of an axially forced jet flame, where both the fuel and oxidizer were forced. Representative results showing the measured, instantaneous spatial dependence of $\xi(x,t)$ at different time instances over a forcing period are shown in Fig. 14. Notice the clear downstream axial convection of the flame wrinkle crests with time, a result predicted by the waveform portion of the above equations. Also shown is an x-t diagram, showing the temporal position of the wrinkle crests, also demonstrating their downstream convection.

Flame wrinkle convection can also be directly inferred from the phase of $\hat{\xi}(x,f=f_f)$. Note that a wrinkle convecting axially at a constant speed, U_c, leads to a linear phase-axial location dependence, with a slope given by:

$$U_c = \left|\frac{2\pi f_f}{\partial\angle\hat{\xi}(x,f=f_f)/\partial x}\right| \tag{28}$$

In real flames with temperature gradients, complex shear flows, and convecting vortical disturbances, it can be anticipated that the evolution of flame wrinkles will be more complex than predicted by the bulk forcing model given by Eq. (25). Nonetheless, the results from the model problem provide useful interpretative insight

---

[1] Note that this wrinkle convection term can be generalized in the case of axially varying mean velocity, $U_0(x)$, to $\left[\int_0^{x/R_f}\frac{\exp[-2\pi iSt\psi]}{U(\psi)Pe(\psi)}d\psi\right]$ where $\mathcal{U}(x)=\frac{\varepsilon U_0(x)}{\hat{u}_{x,1}}$.

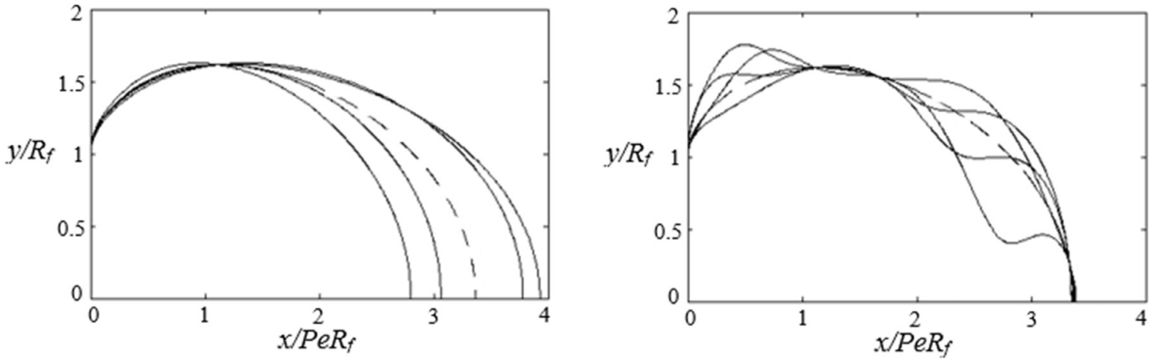

Fig. 11. Snapshots showing four instantaneous positions of a forced non-premixed flame at two different forcing frequencies using nominal values of $Z_{st} = 0.3$, $Pe = 50$, and (left) $\varepsilon = 0.2$, $St = 0.0018$, $St_{L_f} = 0.3$ (right) $\varepsilon = 1.0$, $St = 0.012$, $St_{L_f} = 2.0$ (Reprinted from Magina et al. [92] with permission of Elsevier).

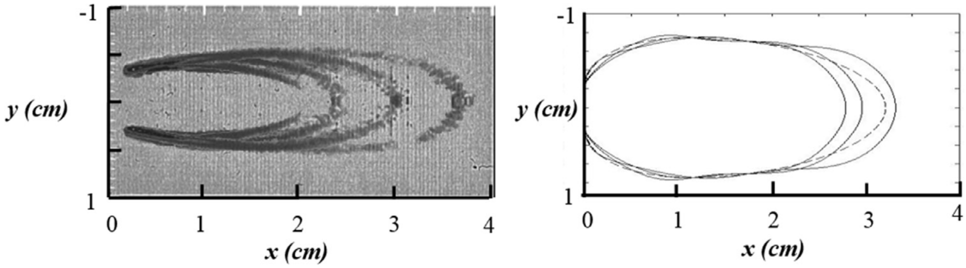

Fig. 12. (left) CH mole fraction experimental isopleths of the steady and time-varying laminar CH_4-air diffusion flame at steady state, 0.00, 0.01, 0.02, 0.03, and 0.04 s (Reprinted from Mohammed et al. [50] with permission of Elsevier). (right) Theoretical results using parameters chosen to match experiments of Pe=0.86, St_{L_f} = 1.82, $Z_{st} = 0.13$ (adjusted from theoretical value shown in Table 3 to match experimental flame length), and ε = 0.5 for a CH_4-air diffusion flame [107].

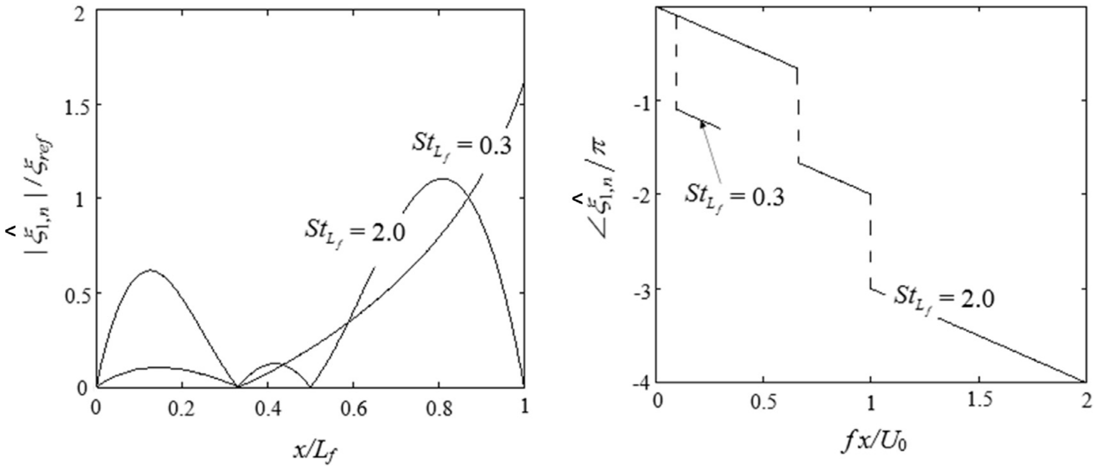

Fig. 13. Axial dependence of (left) magnitude and (right) phase of flame response, where $\xi_{ref} = (\varepsilon \cdot U_0)/(Pe \cdot 2\pi f)$, and using conditions consistent with Fig. 11. Note the abscissa, $(x/U_0/f)$, can equivalently be written as $x/L_{f,0}{}^{*}St_{L_f}$(Reprinted from Magina et al. [92] with permission of Elsevier).

into these data. For example, representative results for the magnitude and phase of the measured flame wrinkle are shown in Fig. 15.

Note the nearly stationary behavior of the flame at the base near the burner lip, i.e. $\hat{\xi}_1(x \sim 0, f = f_f) \sim 0$, indicative of flame attachment – results consistent with the theoretical results developed for non-premixed flames in the fast chemistry, $Pe \to \infty$ limit, which will be examined more explicitly with Model Problem C. Additionally in this near base region, the response magnitude grows with downstream distance, while further downstream the magnitude of flame wrinkling peaks at $x/R_f \sim 6$ and oscillates. This behavior is suggestive of an interference phenomenon, consistent with the model predictions. Similar interference results have been observed for axially forced premixed flame systems [108]. The phase rolls off nearly linearly with axial distance, for the reasons discussed earlier in the context of Fig. 14.

The results from the model problem cannot be directly compared with experimental data because the assumed mean and unsteady velocity fields differ from the actual values. However, direct comparisons can be made by extracting the actual velocity fields from measurements and solving Eqs. (9) and (10) computationally. This was done by Magina et al. [2] and a sample result is shown in Fig. 16. Note similar features as described above and the reasonable correspondence between the measured and predicted flame position fluctuations. The primary differences occur in the near-base region and are discussed in detail by Magina et al. [2]. In another study, the fully nonlinear problem including axial diffusion effects was numerically investigated by Li et al. [109]. They analyzed the effect of Pe on the flame base oscillation and the distribution of

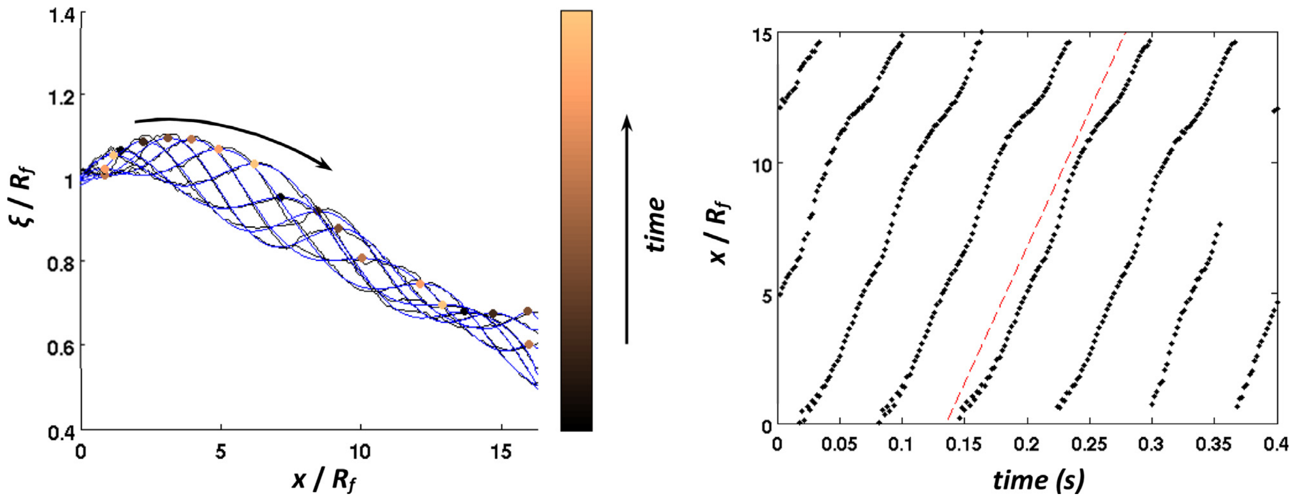

Fig. 14. (left) Instantaneous flame positions at various time instances over a forcing period (black and blue lines indicate raw and smoothed experimental data, respectively, while arrows indicate increasing time) (Reprinted from Magina et al. [2] with permission of Elsevier), and (right) representative axial evolution of the wrinkle crests for a coflowing natural gas non-premixed flame with conditions R_f/R_w=0.1, $U_0 \sim 0.4 m/s$, forcing frequency=30Hz, and ε=0.05. The dashed line indicates a convective velocity of 0.4m/s (Reprinted from Magina [106]).

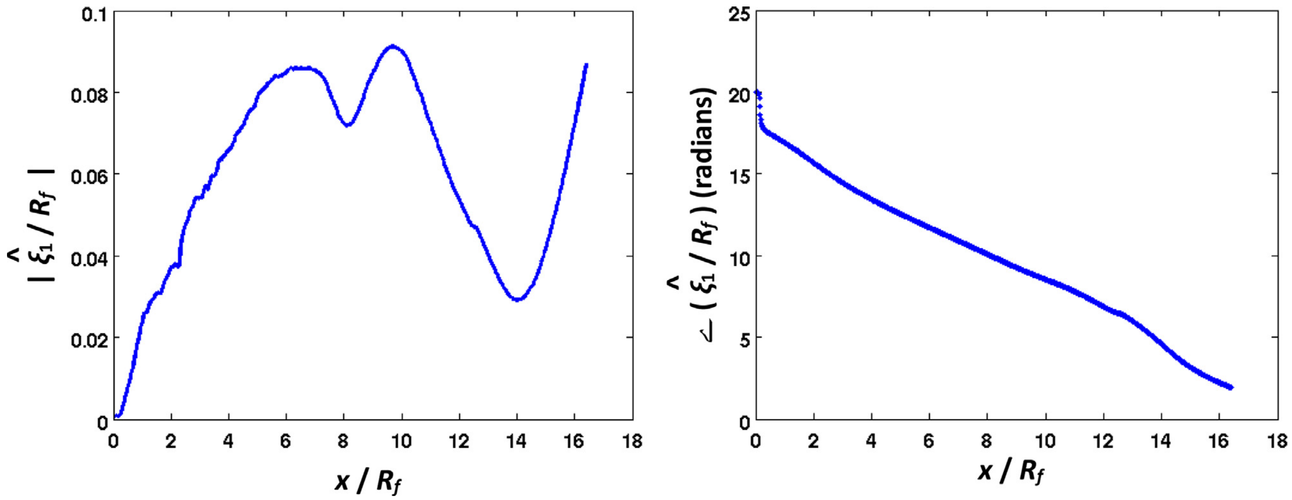

Fig. 15. Measured flame wrinkle amplitude (left) and phase (right) results for a coflowing natural gas non-premixed flame with same conditions as Fig. 14 (Reprinted from Magina et al. [2] with permission of Elsevier).

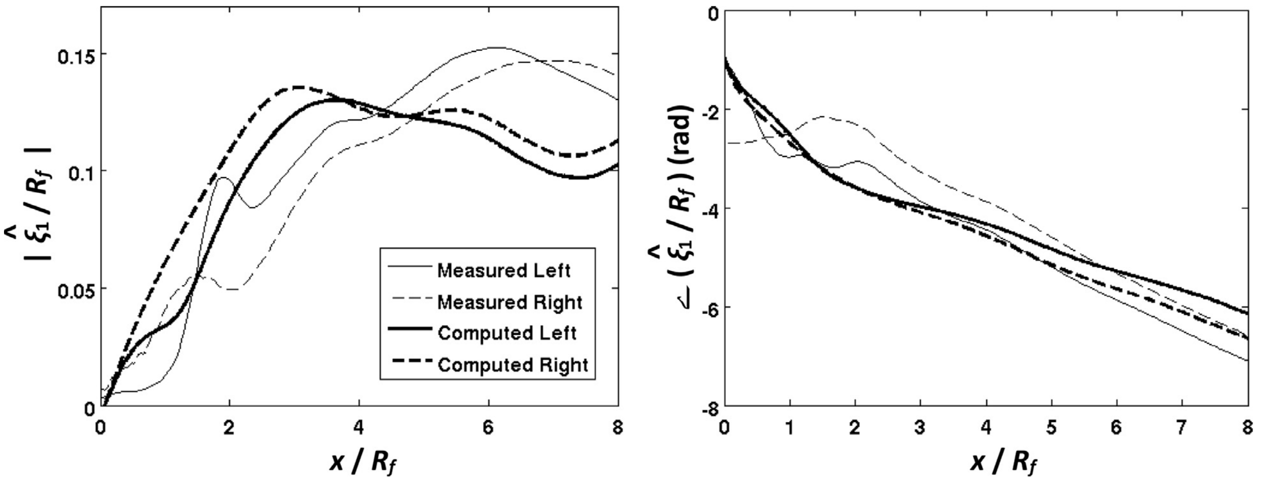

Fig. 16. Axial dependence of magnitude (left) and phase (right) for an axially forced coflowing natural gas non-premixed flame with conditions $R_f/R_w = 0.1$, $U_0 \sim 0.2$ m/s, forcing frequency = 20 Hz, and $\varepsilon = 0.05$. Shown are comparisons between experimental (measured) and modeling (computed) results for both the left and right flame branches (Reprinted from Magina et al. [2]with permission of Elsevier).

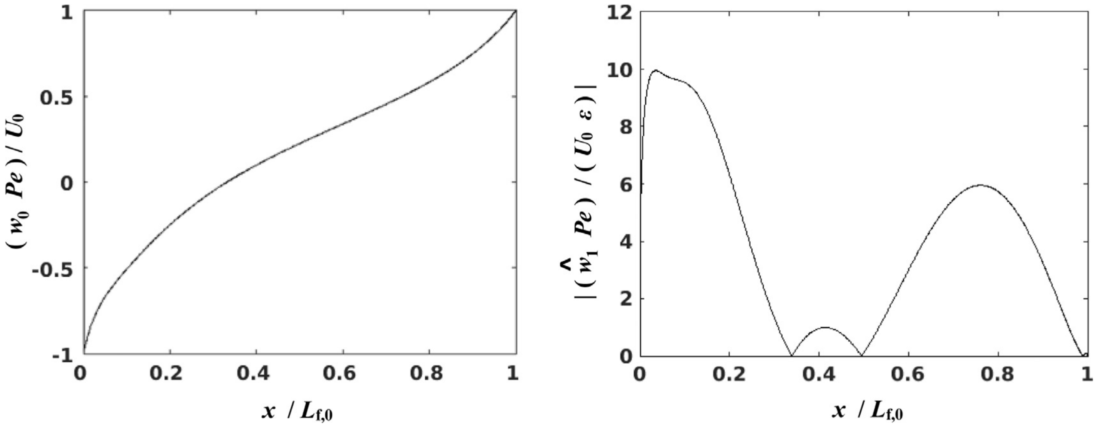

Fig. 17. Non-dimensional velocity of the non-premixed flame surface (see Table 2), using nominal values of Z_{st} **= 0.3**, ***Pe*** **= 20** , *St*= 0.05 , and, ε = 0.01.

mixture fraction field in the near-base region in the presence of the nonlinear terms.

Returning to the model problem presented, it is of interest to discuss the speed of the non-premixed flame sheet with respect to the flow, referred to as w in Table 2. For a premixed flame, this speed is simply the displacement speed, s_d (x,t). Recognizing that the non-premixed flamelet does not propagate, yet is also not a passive scalar that moves with the flow where $w=0$, the speed w can be obtained from the expression in Table 2, $w=-(DZ/Dt)/|\nabla Z|$. This can be made evident by recasting Eq. (5) in the following form:

$$\frac{\partial Z}{\partial t}+\vec{u}\cdot\nabla Z=\mathfrak{D}\nabla^2 Z=-w|\nabla Z| \tag{29}$$

Recalling the flame attachment assumption, this spatio-temporally varying quantity can be non-dimensionalized and expressed as:

$$\frac{w(x,t)}{U_0}=\frac{-R_f}{Pe}\left.\frac{\nabla^2 Z}{|\nabla Z|}\right|_{\xi_0(x)}=-\sin\theta(x,t) \tag{30}$$

where w is defined normal to the flame surface in the direction of the fuel. Similarly, this expression can be decomposed into steady and fluctuating components as:

$$\frac{w_0(x)}{U_0}=\frac{-R_f}{Pe}\left.\frac{\nabla^2 Z_0}{|\nabla Z_0|}\right|_{\xi_0(x)}=-\sin\theta_0(x) \tag{31}$$

$$\begin{aligned}\frac{w_1(x,t)}{U_0}=&\left[\frac{-R_f}{Pe}\left(\frac{\nabla^2 Z_1+\xi_{1,n}\nabla^2(|\nabla Z_0|)}{|\nabla Z_0|}\right)\right.\\&\left.\left.-\frac{w_0(x,t)}{U_0}\left(\frac{\nabla Z_0\cdot\nabla Z_1+\xi_{1,n}\nabla Z_0\cdot\nabla(|\nabla Z_0|)}{|\nabla Z_0|^2}\right)\right]\right|_{\xi_0(x)}\\=&-\sin\theta_1(x,t)\cos\theta_0(x,t)\end{aligned} \tag{32}$$

Representative results are shown in Fig. 17. Interestingly, w can be positive or negative, and varies with both x and t, whereas for premixed flames, s_d is strictly positive and may be a constant. Also, note how the fluctuating burning speed amplitude looks similar in shape to the flame wrinkle amplitude plot, having the same interference node patterns.

3.3. Axial Diffusion effects – model problems B and C

The theoretical analysis in Section 3.1 neglected axial diffusion in order to demonstrate the key physics of flame wrinkle excitation and convection, and the resulting constructive and destructive interference effects this introduced. Of course, this and all other physics were implicitly included in the experimental results. This section analyzes axial diffusion (or equivalently, finite Peclet number effects) in order to explicitly demonstrate how they influence the results.

We start with Model Problem B in Table 4, due to analytical tractability. Recall, Eqs. (11) and (14) provide solutions to the mixture fraction field for the axially forced problem (other forcing configurations can be found in Magina et al. [93]), subject to the step inlet condition, given by Eq. (8), and the flame attachment boundary condition, i.e. $Z_1(x=0,\ y,\ t)=0$. The corresponding solution for $\xi_{1,n}(x,\ t)$ can be written generally, utilizing Eq. (21) and defining $St_\omega=2\pi St$, as:

$$\frac{\xi_{1,n}(x,t)}{R_f}=-\left[\frac{\varepsilon\sin\theta_0(x)e^{-i\omega t}}{iSt_\omega}\right]\frac{\sum_{n=1}^{\infty}\frac{2\beta_-}{n\pi Pe}\cos\left(\mathcal{A}_n\frac{\xi_0(x)}{R_f}\right)\sin(\mathcal{A}_n)e^{\left(\beta_-\frac{x}{PeR_f}\right)}\left[1-e^{\left(\{\beta_{\mathrm{h}-}-\beta_-\}\frac{x}{Pe\,R_f}\right)}\right]}{\sum_{n=1}^{\infty}\frac{2\beta_-}{n\pi Pe}\cos\left(\mathcal{A}_n\frac{\xi_0(x)}{R_f}\right)\sin(\mathcal{A}_n)e^{\left(\beta_-\frac{x}{PeR_f}\right)}} \tag{33}$$

Insight into wave propagation, dissipation, and dispersion effects, as well as direct comparisons between the non-premixed and premixed flame wrinkle dynamics can be obtained by expanding these expressions around the $Pe\rightarrow\infty$ limit in inverse powers of Pe. For example, the $(\beta_{\mathrm{h}-}-\beta_-)/Pe$ term in Eq. (33) can be expanded as:

$$\frac{\{\beta_{\mathrm{h}-}-\beta_-\}}{Pe}=\left\{iSt_\omega-\frac{St_\omega^2}{Pe}-\frac{2iSt_\omega\left(\mathcal{A}_n^2+St_\omega^2\right)}{Pe^2}+\frac{6\mathcal{A}_n^2St_\omega^2+5St_\omega^4}{Pe^3}+\mathrm{O}\left(Pe^{-4}\right)\right\} \tag{34}$$

and will be referred to as the $Pe>>1$ limit. Comparatively, for premixed flames the results of Wang et al. [110] can be similarly expanded for flames that are thin relative to the burner radius; i.e., where $\sigma_C<<1$, σ_C being the scaled Markstein number, Ma, defined by:

$$\sigma_C=\frac{Ma}{2R_f}\left(\frac{1+\alpha^2}{\alpha^2}\right) \tag{35}$$

where $\alpha=L_f/R_f=\cot\theta$ is the premixed flame aspect ratio. By following this procedure to $\mathrm{O}(1/Pe^2)$ and $\mathrm{O}(\sigma_C^2)$, we can develop the following general result, valid for axial or transversely forced premixed or non-premixed flames in the $Pe>>1$ limit:

$$\begin{aligned}\frac{\xi_{1,n}(x,t)}{R_f}=&-\left[\frac{\varepsilon\mathscr{I}(\theta(x))\exp(-i\omega t)}{iSt_\omega}\right]\left[1-\exp\left(\frac{i\omega x}{U_c}\right)\right.\\&\left.\exp\left(\frac{-\zeta x}{R_f}\right)\exp\left(\gamma St_\omega^2\frac{i\omega x}{U_c}\right)\right]+O\left(\frac{1}{Pe^3},\sigma_C^3\right)\end{aligned} \tag{36}$$

Table 5
Propagation, dissipation, and dispersion terms in Eq. (36).

	Premixed	Non-premixed
Propagation speed, U_c	$U_0 \cos^2\theta$	$U_0 + O(1/Pe^2)$
Dissipation, ζ	$St_\omega^2 \sigma_C$	$\frac{St_\omega^2}{Pe}$
Dispersion, γ	$-2\sigma_C^2 \frac{\alpha}{\sqrt{1+\alpha^2}}$	$\frac{-2}{Pe^2}$

where the waveform term is parameterized by a convection speed, U_c, axial dissipation rate, ζ, and dispersion term, γ, defined in Table 5. Additionally, $\mathscr{I}(\theta(x))$ is a forcing configuration parameter taking a value of $\sin\theta_0(x)$ and $\pm\cos\theta_0(x)$ for the axial and transverse forced cases, respectively [93].

Consider the various terms in Eq. (36). Similar to Eqs. (25) and (26), the expression is led by a group of terms which describe the wave magnitude and harmonic time dependence, $[\varepsilon/(iSt_\omega)]\mathscr{I}(\theta(x))\exp(-i\omega t)$, showing the familiar low-pass filter characteristic of flame wrinkle amplitude. The wave magnitude also has an axial dependence whose form depends upon whether the flame is forced axially or transversely. This shows the controlling nature of velocity fluctuations normal to the flame sheet, and how the top and bottom flame branches are in-phase, i.e. mirror images of each other, for axial forcing, and are out-of-phase for transverse forcing. Finally, the non-premixed steady state flame angle is a function of axial coordinate, while for premixed flames with a comparable spatially uniform inflow, U_0, $\mathscr{I}(\theta(x))$ is not.

We next consider the general wave propagation term, contained in the expression $1 - \exp(i\omega x/U_c)\exp(-\zeta x/R_f)\exp(i\gamma St_\omega^2 \omega x/U_c)$. Consistent with the discussion in Section 3.2, the leading unity term derives from the particular solution of the equation, and lacks spatial dependence because of the nature of the assumed bulk forcing. The second term describes a decaying, dispersive traveling wave generated at the boundary, $x = 0$, resulting from the assumption of flame attachment, i.e., $\xi_{1,n}(x=0,\ t)=0$, or fixed mixture fraction at the burner outlet, $\mathcal{Z}_1(x=0,\ y,\ t)=0$, for the premixed and non-premixed cases, respectively.

The leading order expansion of this expression, $1 - \exp(i\omega x/U_c)$, was previously presented and discussed in Sections 3.1 and 3.2. It demonstrates how flame wrinkles propagate without dissipation and non-dispersively in the $Pe\to\infty$ or $\sigma_C \to 0$ limits. In this limit, the major difference between the space-time dynamics of non-premixed and premixed flame dynamics comes from the U_c parameter defined in Table 5. In both cases, local maxima and minima in flame wrinkle amplitude arise through interference between the two terms, revealed in Eq. (27).

Consider next $O(1/Pe)$ or $O(\sigma_C)$ terms which, as shown in Table 5, cause wrinkles to decay exponentially with downstream distance. This causes the interference effect discussed above to become imperfect, an effect that increases quadratically with St_ω. The mechanism for wave dissipation for the two flame types are entirely different – for premixed flames, it is due to the dependence of the flame speed on flame surface curvature, which causes positive Markstein length flames to be thermo-diffusively stable. For non-premixed flames, it is due to the progressive smoothing by diffusion of the spatial variations in the $\mathcal{Z}$ field with downstream distance. Lastly, $O(1/Pe^2)$ and $O(\sigma_C^2)$ effects introduce dispersion, as shown explicitly in Table 5 – i.e., a frequency dependent wave propagation speed.

Illustrative solutions using Eq. (36) are presented for the instantaneous non-premixed flame position at several time instances over a forcing cycle in Fig. 18, as well as the amplitude and phase of the wrinkles in Fig. 19, for constant values of St_{Lf}. The generation and downstream propagation of flame wrinkles can be observed, with a larger number of flame wrinkles being present within the flame length for increasing frequencies. Again, the spatial variation in the amplitude comes from the $\mathscr{I}(\theta(x))$ term, specifically $\sin\theta_0(x)$ for this axially forced case depicted, as well as the spatial interference effect in Eq. (36). The local maxima and minima referred to above are clearly evident in the figures for the weakly dissipative solutions. The phase rolls off linearly with axial distance, reflecting the convection process described, and jumps 180° across the nodes. Note the smoothing of the wrinkles that occurs in the mid and far field with decreasing Pe, due to wave dissipation discussed in the context of Eq. (34). This effect reduces the overall peak-to-crest wrinkle amplitudes, as well as eliminating previously spatially stationary nodes, represented by the liftoff from the vertical axis. This leads to a complete loss of the spatial interference pattern for the $Pe = 5$ case relative to the $Pe\to\infty$ case. In addition, the phase does not roll off linearly in the axial direction, and the discontinuous phase jumps are smoothed. Lastly, the steady state flame position becomes modified by axial diffusion. Both the flame tip location (i.e. overall flame length), and the location of maximum width move downstream, as can be seen from Fig. 19 by the movement of the flame angle forced node, an effect which was shown to impact the dynamics in Section 3.1.

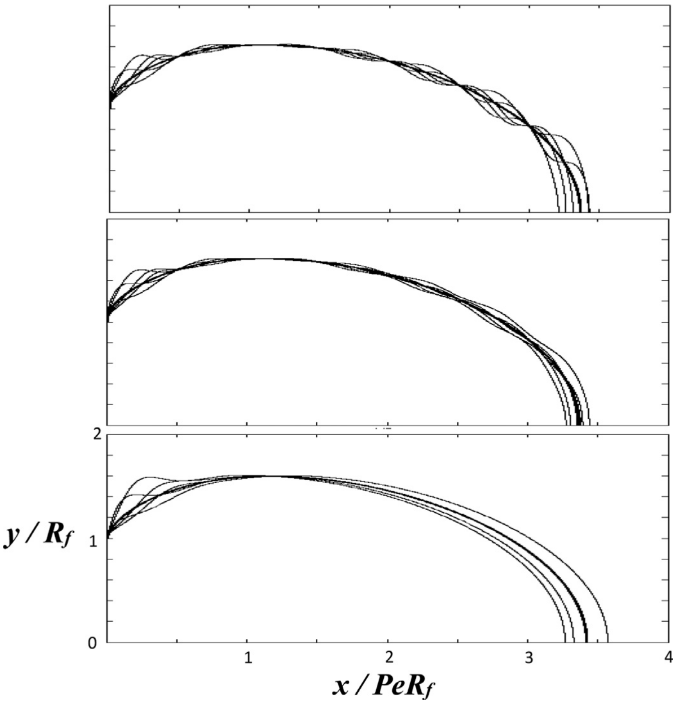

Fig. 18. Instantaneous snapshots of axially forced flame position at several time instances for Model Problem A, i.e. $Pe\to\infty$ solution, (top) and Model Problem B, i.e. general $Pe >> 1$ solution, at two representative Pe values of 20 (middle), and 5 (bottom) for $PeSt_\omega = 4\pi$ and $\mathcal{Z}_{st} = 0.3$. Note the x-axis is rescaled by Pe (Reprinted from Magina et al. [93] with permission of Elsevier).

It is important to note that although these solutions include axial diffusion in the governing equation, they utilize the step inlet boundary condition at $x = 0$, given by Eq. (8). As noted earlier, this boundary condition itself implicitly neglects axial diffusion. It also creates a non-physical infinite transverse gradient in mixture fraction at the fuel port lip, a singularity that dominates certain solution characteristics such as the flame attachment and asymptotic heat release characteristics (to be discussed in Section 4). In reality, axial diffusion smoothes out this step boundary condition, as fuel diffuses upstream into the oxidizer "port" and vice versa. These additional boundary condition effects can be treated with Model Problem C, first considered by Magina et al. [95], by considering a modified domain with an extended inlet, as shown in Fig. 20. Note

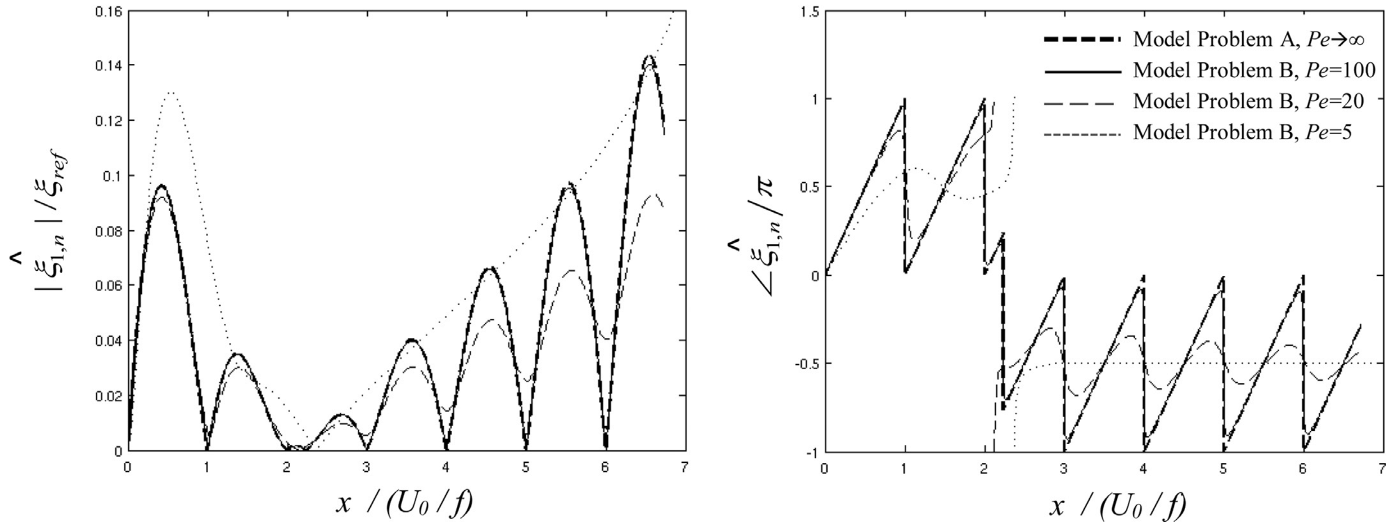

Fig. 19. Axial dependence of the magnitude (left) and phase (right) of $\hat{\xi}_{1,n}$, plotted against the ratio of axial coordinate to convective wavelength for Model Problem A, i.e the $Pe\to\infty$ limit, and Model Problem B, i.e. general $Pe > > 1$ solution, at three representative Pe values of 100, 20, and 5 for $PeSt_\omega = 4\pi$ and $Z_{st} = 0.3$(Reprinted from Magina et al. [93] with permission of Elsevier).

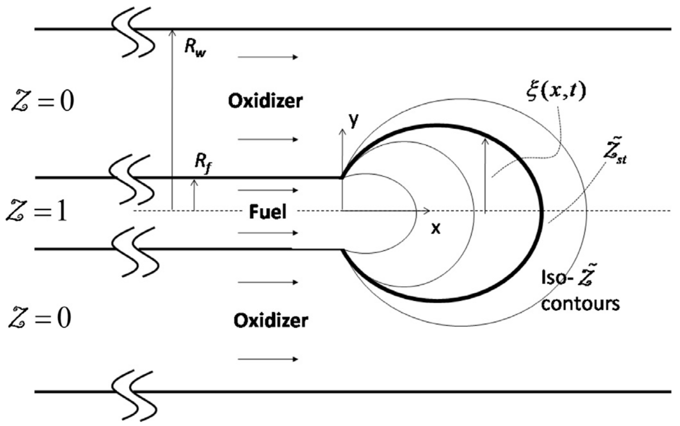

Fig. 20. Illustration of the forced non-premixed flame Model Problem C, referred to as the "extended inlet" geometry. The $x < 0$ and $x > 0$ domains are denoted the fuel/oxidizer ports and combustion region, respectively.

the fuel and oxidizer reservoirs, located at $x = -\infty$, where:

$$Z(x=-\infty,y) = \begin{cases} 1 & 0<|y|<R_f \\ 0 & R_f<|y|<R_w \end{cases} \tag{37}$$

In other words, to properly and consistently include and account for axial diffusion effects, and to properly describe the fuel/oxidizer gradients near the burner lip, we must include the $x < 0$ fuel and oxidizer ports, since fuel can diffuse back into the oxidizer port and vice versa, altering the inlet profile. In addition, no diffusion through the side walls and fuel port walls implies the following additional conditions:

$$\frac{\partial Z}{\partial y}(x,y=\pm R_w)=0 \qquad \frac{\partial Z}{\partial y}\left(x<0,y=\pm R_f\right)=0 \tag{38}$$

Numerical solutions of this equation show that inclusion of axial diffusion, in addition to direct effects on the wrinkle dynamics discussed above, influences the instantaneous flame attachment point, i.e. the location where the reaction sheet intersects with the fuel port wall. In the $Pe\to\infty$ limit, this location is stationary and always positioned at the fuel port lip, $x = 0$ and $y = R_f$, valid for all values of Pe and Z_{st}, directly resulting from the inlet condition, i.e. $Z_1(x=0,\ y,\ t)=0$. This is the justification for the analytical $|\xi_{1,n}|$ curves starting from zero at $x = 0$ in Fig. 13 and Fig. 19. However, coupled axial and transverse diffusion effects move this flame attachment point away from the outlet and into the fuel or oxidizer ports (depending on the specific Z_{st} and Pe values); i.e., into the $x < 0$ domain. This effect can be observed in the experimental $|\xi_{1,n}|$ curves starting from a slightly positive value at $x = 0$ in Fig. 16, or other data in Magina et al. [95].

Relatedly, the instantaneous attachment point moves over a forcing period. Fig. 21 shows a sample result for the magnitude and phase plots of the instantaneous flame attachment point transfer function for a range of St values. The transfer function, defined as $(x_{\text{attach}}/R_f)\ /\ (u_1/U_0)$ quantifies the input-output relation between forcing and flame attachment point motion. Notice how the magnitude of this axial motion depends upon the forcing frequency. Consistent with the discussion in Section 3.2, this is due to the low-pass filter characteristic of the flame position, as the time derivative of the flame position is related to the local flow velocity through Eq. (5). In addition, there is increased motion at low Pe values, due to the increased contribution of axial diffusion. The Z_{st} value also has an influence upon the transfer functions, an effect which is coupled to Pe [95]. For example, very low and high Z_{st} values have larger transfer function amplitudes than intermediate values.

3.4. Multi-dimensional forcing effects

The previous sections have covered the idealistic case of two dimensional non-premixed flames excited by unidirectional, spatially uniform, fluctuations in flow velocity. However, real combustion systems are not this simple, being inherently three-dimensional, and are often times exposed to multi-dimensional disturbances (e.g., helical vortices or transverse acoustic waves) and have multi-dimensional time averaged flow fields (e.g., swirling jet flows), effects which introduce rich flame dynamics, such as azimuthal wrinkle convection. This section presents the results for round jets (note the prior sections considered two-dimensional jets) subjected to these disturbances, closely following Magina et al. [111].

Still working within the mixture fraction formulation, the instantaneous position of the three-dimensional reaction sheet, in

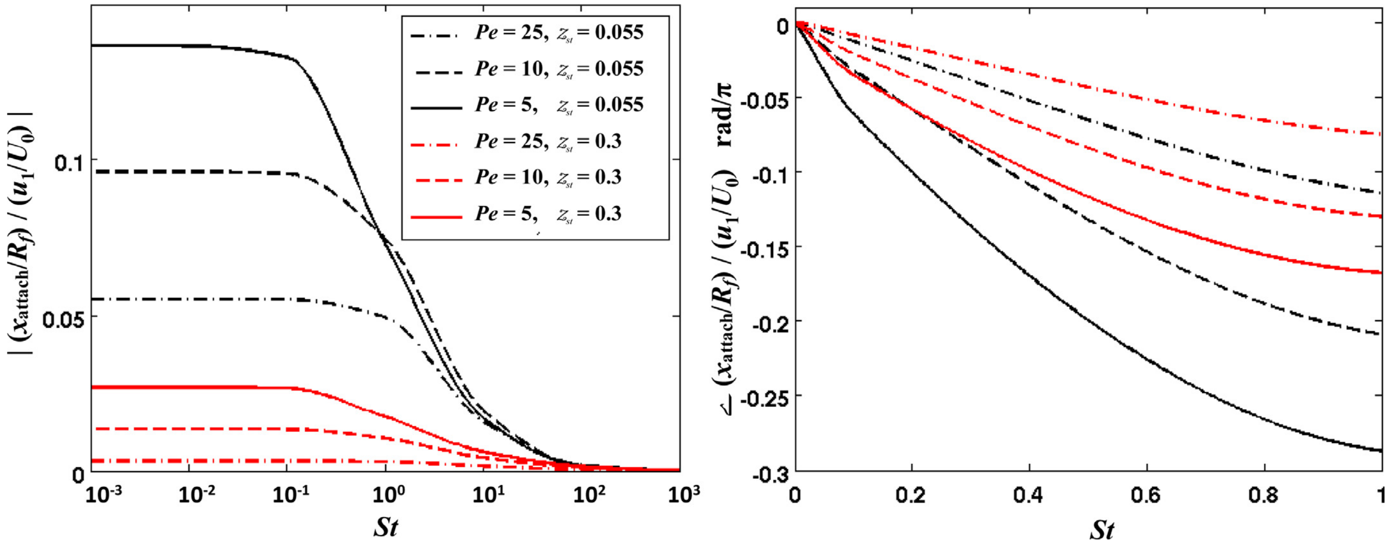

Fig. 21. Magnitude (left) and phase (right) of the instantaneous attachment point transfer function for Model Problem C (Reprinted from Magina et al. [95] with permission of Elsevier).

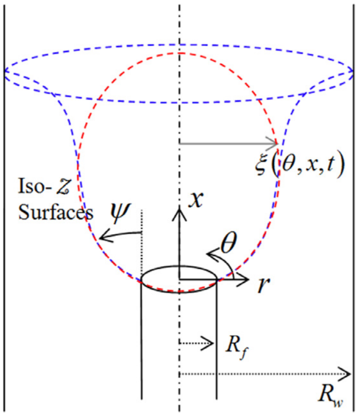

Fig. 22. Schematic of the model three-dimensional swirling non-premixed flame. Images show a steady over (red dashed line) and under (blue dashed line) ventilated flame.(For interpretation of the references to colour in this figure legend, the reader is referred to the web version of this article.)

cylindrical coordinates, is defined by $r = \xi(\theta, x, t)$, as shown in Fig. 22.

The previously implemented boundary conditions can be reformulated for this three-dimensional domain. In order to isolate and spotlight the new dynamics features introduced, a step inlet boundary condition is once again utilized (three-dimensional variant of Eq. (8)) and the solution derived in the limit of small perturbations, and thus each variable is expanded as $(\ )(r, \theta, x, t) = (\ )_0\,(r,\theta, x) + (\ )_1(r,\theta, x, t)$. The solution to the zeroth order form of the $\mathcal{Z}$-equation, Eq. (5), in cylindrical coordinates, subject to the flow conditions of uniform axial velocity, U_0, swirl velocity, $u_{\theta,0} = \Omega r$ (where Ω is the angular rate of swirl), and no radial velocity, $u_{r,0} = 0$, is given by:

$$\mathcal{Z}_0(r, x, \zeta) = s^2 + \sum_{n=1}^{\infty} \frac{2sJ_1(r_n s)}{J_0(r_n)^2 r_n} J_0\left(r_n s \frac{r}{R_f}\right) \exp\left[\frac{\mathcal{B}_-}{Pe}\frac{x}{R_f}\right] \tag{39}$$

where r_n is the n^{th} root of the first order Bessel function of the first kind, i.e. $J_1(r_n) = 0$, and $\mathcal{B}_-$ is given by (noting the similarities to the two-dimensional jet eigenvalues in Eq. (15)):

$$\mathcal{B}_- = \frac{Pe^2 - \sqrt{Pe^4 + 4(r_n s)^2 Pe^2}}{2}$$
$$\mathcal{B}_h = \frac{Pe^2 - \sqrt{Pe^4 + 4Pe^2(r_n s)^2 - 8\pi i Pe^3 St}}{2} \tag{40}$$

This form of the swirl velocity represents solid body rotation, and can also be written as $u_{\theta,0} = 2\pi St\sigma(r/R_f)U_0$, where $\sigma = \Omega/\omega$ is the non-dimensional swirl parameter. The first order form of the $\mathcal{Z}$-equation, in cylindrical coordinates takes the following form:

$$\frac{\partial \mathcal{Z}_1}{\partial t} + u_{r,0}\frac{\partial \mathcal{Z}_1}{\partial r} + \frac{u_{\theta,0}}{r}\frac{\partial \mathcal{Z}_1}{\partial \theta} + u_{x,0}\frac{\partial \mathcal{Z}_1}{\partial x} - \mathcal{D}\left[\frac{1}{r}\frac{\partial \mathcal{Z}_1}{\partial r} + \frac{\partial^2 \mathcal{Z}_1}{\partial r^2} + \frac{1}{r^2}\frac{\partial^2 \mathcal{Z}_1}{\partial \theta^2} + \frac{\partial^2 \mathcal{Z}_1}{\partial x^2}\right]$$
$$= -u_{r,1}\frac{\partial \mathcal{Z}_0}{\partial r} - \frac{u_{\theta,1}}{r}\frac{\partial \mathcal{Z}_0}{\partial \theta} - u_{x,1}\frac{\partial \mathcal{Z}_0}{\partial x} \tag{41}$$

We can identify several canonical forcing configurations, characterized by the forcing velocity field sets shown in Table 6. Bulk axial forcing of the round jet is conceptually similar to the two-dimensional case discussed in Sections 3.1 thru 3.3, the key difference being mean flame shape; i.e. $\theta_0(x)$, which will be referred to as $\psi_0(x)$ for the cylindrical configuration (see Fig. 22).

The next case shown in Table 6 is bulk transverse forcing, which is substantially different from the two-dimensional case discussed in Section 3.3. Significantly, the angle of the transverse forcing with respect to the sheet ranges from normal incidence (as in the two-dimensional case) to grazing (where it causes no wrinkle excitation). If there is no swirl, this causes the largest wrinkling to occur on the opposing sides of the flame that are subjected to the normally incident velocity disturbance, and no wrinkling at all to occur on the opposing sides with grazing incidence. However, in the presence of swirl azimuthal transport of these wrinkles causes flame wrinkling to occur at all azimuthal locations [111]. The combined action of both axial and azimuthal convection of flame wrinkles leads to interference in both axial and azimuthal directions. The last case shown in Table 6 is helical forcing, for which there is no two-dimensional analogue. For this reason, this problem is considered in more detail in the next section.

3.4.1. Convecting helical disturbance solutions

Round jets, whether swirling or non-swirling, often exhibit organized vortical disturbances that wind helically around the jet

Table 6
Forcing fluctuating velocity set for various forcing configurations, with reference to Eq. (41).

	$u_{r,1}$	$u_{\theta,1}$	$u_{x,1}$
Bulk Axial	$u_{r,1}=0$	$u_{\theta,1}=0$	$u_{x,1}=\varepsilon\ U_0\exp\left[-i\omega t\right]$
Bulk Transverse	$u_{r,1}=\varepsilon\ U_0\cos\theta\exp\left[-i\omega t\right]$	$u_{\theta,1}=-\varepsilon\ U_0\sin\theta\exp\left[-i\omega t\right]$	$u_{x,1}=0$
Convecting Helical	$u_{r,1}=0$	$u_{\theta,1}=0$	$u_{x,1}=\varepsilon U_0\exp\left[-i\omega t+ikx+im\theta\right]$

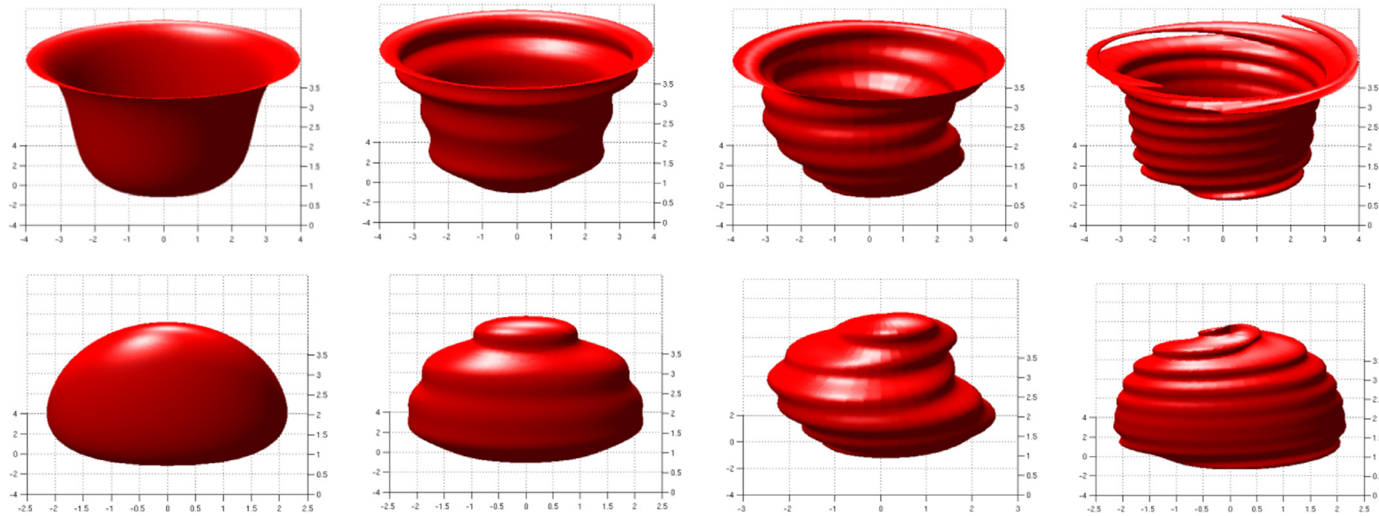

Fig. 23. Steady state and instantaneous mixture fraction field isocontours for an under (top row, $\mathcal{Z}_{st}$ = 0.055) and over (bottom row, $\mathcal{Z}_{st}$ = 0.08) ventilated non-premixed flame in a swirling convecting mean flow, subject to axial bulk disturbance, transverse bulk disturbance, and a helical disturbance with $m = -1$, $k_c = 5$ (from left to right) for parameters $Pe = 10$, $St = 0.1$, $s = 0.25$.

shear layers. In this formulation, $k=\omega/U_c$ is the helical convective disturbance velocity, $k_c=U_c/U_0$ is the phase speed of the disturbance normalized by the axial flow velocity, and m is the helical mode number; note that $m=0$ is the axisymmetric mode, whereas, for a positive axial wavenumber, $m>0$ and <0 denote the co-swirling, counter-winding and counter-swirling, co-winding modes, respectively. In both non-premixed and premixed flames, it is well known that important interference effects control the axial flame wrinkling character, as vortices disturbing the flame, and the flame wrinkles excited by these convecting vortices, do not generally travel at the same speed.

The analytical solution of Eq. (41) is considerably simplified by neglecting azimuthal diffusion, a good approximation for realistic σ and St values [111], without losing any key dynamical features. Considering a variant of Model Problem B to this round jet configuration, the general solution for the fluctuating mixture fraction field, subject to the flame attachment boundary condition, $\mathcal{Z}_1(r,\theta, x=0)=0$, at the fuel port lip is:

$$\mathcal{Z}_1(r,\theta,x,t)=\sum_{n=0}^{\infty}\frac{-2\varepsilon\mathcal{B}_-sJ_1(r_ns)\exp[im\theta]\exp[-i\omega t]J_0\left(r_ns\frac{r}{R_f}\right)\exp\left(\frac{\mathcal{B}_-}{Pe}\frac{x}{R_f}\right)}{J_0(r_n)^2r_n\left(-2\pi iPeSt\left(1-\sigma m-\frac{\sqrt{Pe^4+4Pe^2(r_ns)^2}}{k_cPe^2}\right)+\left(\frac{2\pi St}{k_c}\right)^2\right)}\left\{\exp\left[\frac{2\pi iSt}{k_c}\frac{x}{R_f}\right]-\exp\left[\frac{\{\mathcal{B}_{hm}-\mathcal{B}_-\}}{Pe}\frac{x}{R_f}\right]\right\} \tag{42}$$

where

$$\mathcal{B}_{hm}=\frac{Pe^2-\sqrt{Pe^4+4Pe^2(r_ns)^2-8\pi iPe^3St(1-\sigma m)}}{2} \tag{43}$$

Fig. 23 shows representative instantaneous $\mathcal{Z}=\mathcal{Z}_{st}$ isocontours for the unforced case and each forced problem denoted in Table 6, for both the over- and under-ventilated non-premixed flame configurations. Notice the clear wrinkling of the flame and its azimuthal dependence in the transverse and helically forced cases, a feature that will be discussed further next.

Following the procedure outlined in Section 3.1, the first order flame position fluctuations can be extracted from this solution and written explicitly as:

$$\frac{\xi_{1,n}(\theta,x,t)}{R_f}=\sum_{n=0}^{\infty}\frac{\varepsilon\exp[im\theta]\exp[-i\omega t]}{\left(-2\pi iSt\left(1-\sigma m-\frac{\sqrt{Pe^4+4Pe^2(r_ns)^2}}{k_cPe^2}\right)+\frac{(2\pi St)^2}{k_c^2Pe}\right)}\left[\frac{\partial\mathcal{Z}_{0,n}/\partial x}{|\Delta\mathcal{Z}_0|_{(r=\xi_0(x),x)}}\right]\left\{\exp\left[\frac{2\pi iSt}{k_c}\frac{x}{R_f}\right]-\exp\left[\frac{\{\mathcal{B}_{hm}-\mathcal{B}_-\}}{Pe}\frac{x}{R_f}\right]\right\} \tag{44}$$

where $\partial\mathcal{Z}_{0,n}/\partial x$ is the n^{th} term of the $\partial\mathcal{Z}_0/\partial x$ summation and $\xi_{1,n}$ is the wrinkle fluctuation measured normal to the mean flame surface.

As was demonstrated by Section 3.2, more insight into this solution in the high Pe limit can be obtained by formally expanding it in inverse powers of Pe, following the work by Magina et al. [93]. Retaining terms up to order $1/Pe$ yields[2]:

$$\frac{\xi_{1,n}(\theta,x,t)}{R_f}=\frac{-\varepsilon\exp[im\theta]\exp[-i\omega t]}{2\pi iSt\chi-\frac{4\pi^2St^2}{k_c^2Pe}}\sin\psi_0(x)\exp\left[\frac{2\pi iSt}{k_c}\frac{x}{R_f}\right]\left\{1-\exp\left[2\pi iSt\chi\frac{x}{R_f}\right]\exp\left[-\frac{4\pi^2St^2(1-m\sigma)^2}{Pe}\frac{x}{R_f}\right]\right\}+O\left(\frac{1}{Pe^2}\right) \tag{45}$$

where

$$\chi=1-m\sigma-1/k_c \tag{46}$$

---

[2] The equivalent $Pe>>1$ solutions for an axially and transversely forced system, respectively, are:

$$\frac{\xi_{1,n}(x,t)}{R_f}=\frac{i\varepsilon\exp[-i\omega t]}{2\pi St}\sin\psi_0(x)[1-\exp[2\pi iSt\frac{x}{R_f}]\exp[-\frac{4\pi^2St^2}{Pe}\frac{x}{R_f}]]+O(\frac{1}{Pe^2})$$

$$\frac{\xi_{1,n}(\theta,x,t)}{R_f}=\frac{i\varepsilon\exp[-i\omega t]}{4\pi St}\cos\psi_0(x)\left[\begin{array}{l}\frac{\exp(i\theta)}{(1-\sigma)}\{1-\exp[2\pi iSt(1-\sigma)\frac{x}{R_f}]\exp[-\frac{4\pi^2St^2(1-\sigma)^2}{Pe}\frac{x}{R_f}]\}+\\ \frac{\exp(-i\theta)}{(1+\sigma)}\{1-\exp[2\pi iSt(1+\sigma)\frac{x}{R_f}]\exp[-\frac{4\pi^2St^2(1+\sigma)^2}{Pe}\frac{x}{R_f}]\}\end{array}\right]+O(\frac{1}{Pe^2})$$

This solution has similar low-pass filter and mean flame angle axial dependence as the previous bulk forced solutions, however, the leading wrinkle magnitude and waveform terms are more complicated due to the convective nature of the disturbance and the parameter χ; thus significantly, azimuthal interference changes the axial amplitude and phase dependence. To leading order in *Pe*, the denominator shows how the complex interaction of swirl strength, helical mode, and disturbance phase speed act to alter the flame wrinkle magnitude, an interaction which produces a maximum in local spatial response for $\chi = 0$, or corresponding mode number given by:

$$m_s\sigma = 1 - 1/k_c \tag{47}$$

Similar criterion holds for premixed flames [112], and corresponds to the case where the azimuthal forcing exactly mirrors the wrinkle convection, so that no destructive interference occurs; rather they constructively superpose to cause the magnitude of flame wrinkling to grow monotonically with downstream distance [111]. Significantly for this axisymmetric mean flow, helical modes in the flow excite a corresponding helical motion in the flame response.

In the presence of swirl, there are no azimuthal locations at which the flame is unwrinkled, due to simultaneous azimuthal and axial propagation of wrinkles by the flow. Swirl acts to azimuthally transport wrinkles around the flame to other θ angles, contributing to the imperfect nature of the spatial interference at a given angle, thus eliminating previously existing spatial nodes due to azimuthal convection.

The two new additional parameters which emerge as significant controllers of flame wrinkle dynamics are k_c and σm; note that σ and m always appear together in this form, indicating that swirl only influences the flame response through helical modes. Both terms alter the wrinkle interference pattern as well as the flames relative sensitivity to various co- and counter-rotating helical modes, an effect which can be more easily observed by rewriting Eq. (46) as, $\chi = \sigma(m_s - m)$. To leading order in *Pe*, mode numbers closer to the value m_s produce a lower value of χ and hence a higher flame motion response amplitude, and vice versa.

An additional important point is that to leading order in *Pe*, the wrinkle magnitude is independent of the sign of χ, whereas this is important for the phase of the flame response. At a given azimuthal location, the axial phase varies linearly with downstream distance with a slope given by $\pi St(\chi - 2/k_c)$. Thus, for the delineating case of $\chi = 2/k_c$, the flame response fluctuations at all axial locations, for a given azimuthal location, are in phase with each other. When $\chi > 2/k_c$, the phase roll off is positive, indicating an apparent negative phase speed (at a fixed azimuthal location), an aliasing previously discussed for helically forced, premixed flames [112]. In reality, the flame wrinkles are always convecting downstream, but if imaged via their projection through a plane (such as with a laser sheet), the helical flame wrinkle slicing through the plane can provide the impression of the wrinkle moving backward for certain parameter combinations [113].

These points are slightly modified if order $1/Pe$ terms are included, due to the additional term in the denominator of the magnitude term, which acts to alter the wrinkle magnitude and phase roll off. In addition, the $O(1/Pe)$ waveform term $(1 - \sigma m)^2$ acts to alter the dissipation term non-monotonically, leading to minimum wrinkle dissipation when $\sigma m = 1$. These features can be seen in Fig. 24 which shows illustrative solutions of the axial dependence of flame wrinkle magnitude and phase for various values of χ for a near-bulk ($k_c = 20$) and convecting disturbance ($k_c = 3.33$) case. Notice, that results are shown for both Model Problem A ($Pe \to \infty$) and Model Problem B ($Pe >> 1$) from Table 4.

These results can be compared to those obtained for axisymmetric swirling premixed flames under similar forcing conditions using the results of Acharya et al. [112, 113]. These expressions are almost identical in form to those for the non-premixed case, with a few subtle differences common to the discussion in Section 3.2. First, the premixed flame angle term is independent of the axial coordinate, owing to the flat nature of the steady state flame sheet, whereas for the non-premixed case this term is a complex function of *x*, *Pe*, $\mathcal{Z}_{st}$, and *s*. Second, the wrinkle convection parameter for the premixed case has an additional $\cos^2\psi$, due to the mechanism of premixed flame normal propagation.

3.4.2. Large amplitude forcing and pocket formation

As was discussed in Section 2, at large disturbance amplitudes, non-premixed flame sheets can become multiply connected. This effect has been referred to as “clipping”, where the upper portion of the flame becomes detached from the main body and convects downstream, much like a burning droplet [32, 114]. Premixed flames similarly become multi-connected, an effect greatly enhanced by the front propagation. Dworkin et al. [63] showed how large amplitude modulation can lead to pinch-off of the top portion of the flame into a pocket. The considerable corrugation of the flame front causes it to self-intersect and split, and the resulting disconnected region collapses while convecting downstream, even while the remainder of the surface enlarges near the base [90]. As this phenomenon occurs with large particle displacement, it has been found in experimental and computational studies to only occur *below* a certain frequency of excitation and *above* a critical amplitude for that frequency.

Experimental [114] and computational [32] studies of soot volume fraction in flickering CH_4/air non-premixed flames have shown that for conditions in which the tip of the flame is clipped, soot production is significantly greater than similar unclipped flames, as well as being 4–5x greater than that measured for steady flames. This effect can be explained by the maximum downstream location obtained by a portion of clipped flame exceeding that for a similar conditioned, i.e. forcing frequency, unclipped flame, resulting in considerably longer soot growth times. Fig. 3 shows two examples of flames with large amplitude oscillations where the flame becomes multi-connected at the tip, one due to a natural instability and the other due to external forcing.

4. Heat release analysis

Having introduced the local space-time wrinkling characteristics of the flame, this section discusses the heat release dynamics. The subsequent discussion considers the local heat release, $q(x, t)$, followed by a treatment of the spatially integrated heat release, $\dot{Q}(t)$.

4.1. Local heat release analysis

The heat release per unit surface area of the flamelet is given by:

$$q(\vec{x}, t) = \dot{m}_F''(\vec{x}, t)\, \mathscr{h}_R(\vec{x}, t) \tag{48}$$

where $\dot{m}_F''$ is the fuel (reactant) mass consumption rate per unit area, and $\mathscr{h}_R$ is the heat release per unit mass of fuel (reactant) consumed for the non-premixed (premixed) flame case. For the two-dimensional flame to be considered next to illustrate key concepts, the terms in Eq. (48) take the form (x,t), while equivalently these expressions would be written as $(x,\theta,\ t)$ for a jet flame. This mass burning rate term is controlled by quite different processes for premixed and non-premixed flames [92]. For premixed flames, the mass burning rate is given by:

$$\textit{Premixed flame}: \quad \dot{m}_F'' = \rho^u s_c^u \tag{49}$$

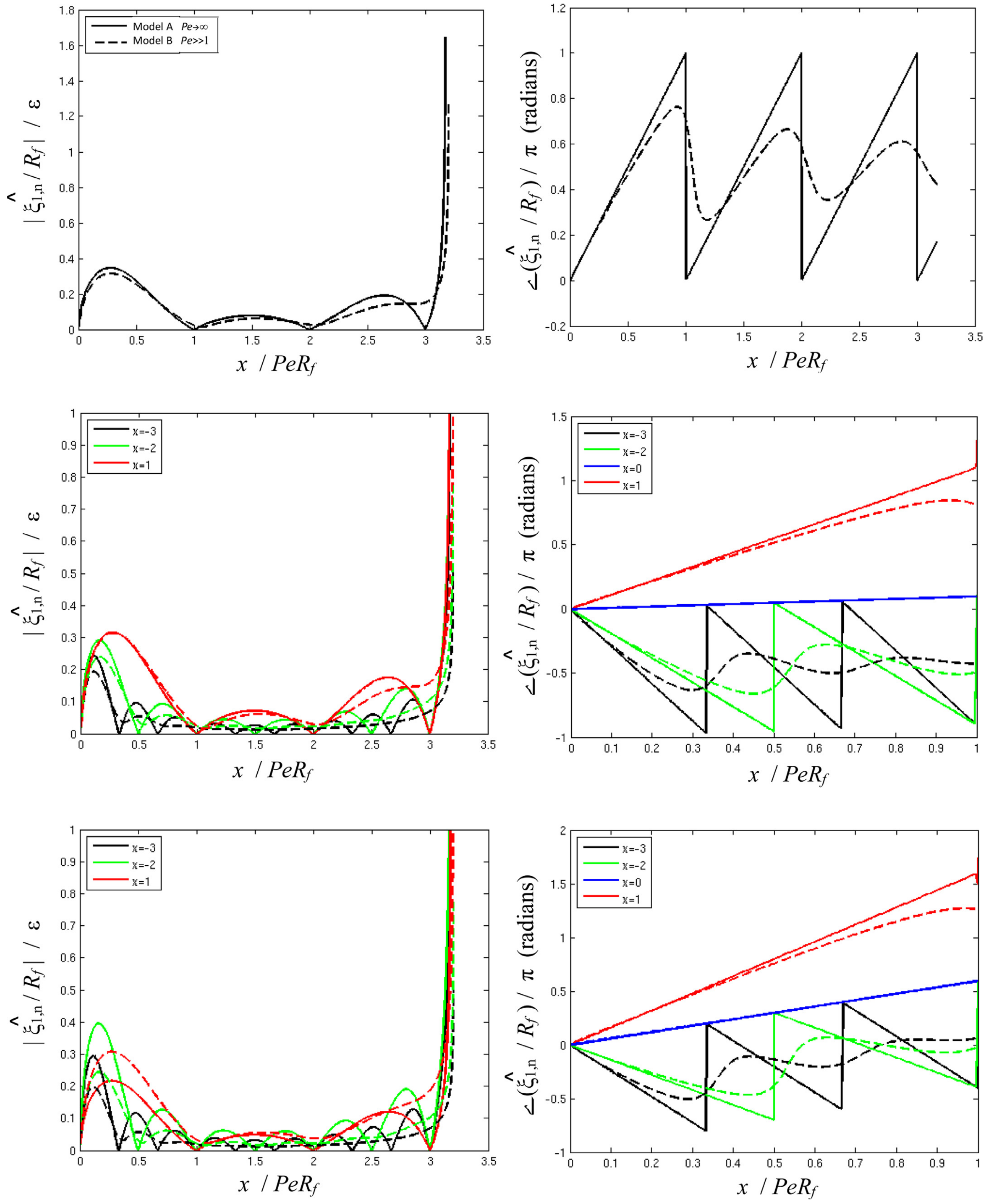

Fig. 24. Axial dependence of flame wrinkle amplitude (left) and phase (right) for (top) the axial bulk forced case and axial convecting helical disturbance case for various χ values and $k_c = 20$ (middle) and $k_c = 3.33$ (bottom), and parameters $Pe = 10$, $St = 0.1$, $\varepsilon = 0.01$, $s = 0.25$, and $Z_{st} = 0.055$. Results are shown for both Model Problem A ($Pe \to \infty$) via solid lines and Model Problem B ($Pe >> 1$) via dashed lines.

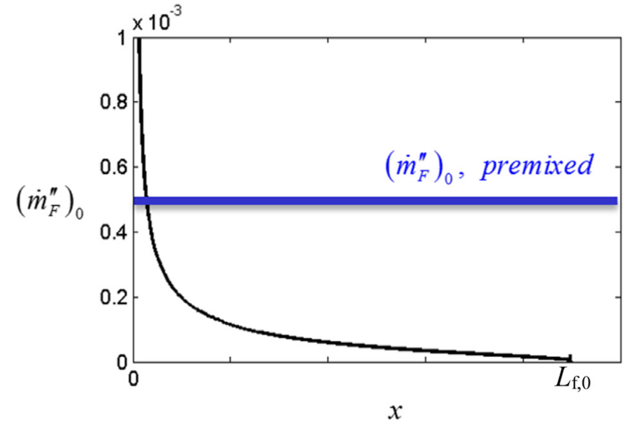

Fig. 25. Depiction of the time averaged burning rate plotted along the flame surface for non-premixed and premixed flames.

where ρ^u is the density and s_c^u is the laminar consumption speed of the unburned reactant. For non-premixed flames, this term is given by [92]:

$$Non-premixed\ flame:\quad \dot{m}''_F = \frac{-(1+\varphi_{Ox})^2}{\varphi_{Ox}}\rho\mathfrak{D}\frac{\partial \mathcal{Z}}{\partial n} \tag{50}$$

where n represents the direction normal to the flame surface into the oxidizer. For example, considering the two-dimensional flames shown in Fig. 8 or Fig. 20, $\partial \mathcal{Z}/\partial n$ is given by:

$$\frac{\partial \mathcal{Z}}{\partial n} = \frac{\partial \mathcal{Z}}{\partial x}\sin\theta - \frac{\partial \mathcal{Z}}{\partial y}\cos\theta \tag{51}$$

The remainder of this section will consider the axial distribution of the local heat release. We will assume that the reactant composition is fixed, such that k_R does not vary, resulting in the local heat release rate being directly proportional to the mass burning rate. The solutions to the model problems detailed in Section 3 can then be utilized, along with Eq. (50) to calculate the heat release and other useful metrics.

A key result that controls many of the non-premixed heat release characteristics, as well as provides significant differences with premixed flames, is that the local heat release distribution is extremely non-uniform – for large Pe value flames, the majority of the heat release occurs near $x=0$ [95]. This can be seen by taking the solutions for Model Problem A, detailed in Section 3.1 (specifically Eqs. (13) and (17)[3]), and writing the solution for $\partial \mathcal{Z}/\partial n$ from Eq. (51) (neglecting the axial diffusion term, $\partial \mathcal{Z}/\partial x$):

$$Means:\quad \frac{\partial \mathcal{Z}_0}{\partial n} = -\frac{\partial \mathcal{Z}_0}{\partial y}\cos\theta = \cos\theta\sum_{n=1}^{\infty}\frac{2\mathcal{A}_n}{n\pi R_f}\sin(\mathcal{A}_n)$$
$$\sin\left(\mathcal{A}_n\frac{y}{R_f}\right)\exp\left(-\mathcal{A}_n{}^2\frac{x}{PeR_f}\right) \tag{52}$$

$$Fluctuating:\quad \frac{\partial \mathcal{Z}_1}{\partial n} = -\frac{\partial \mathcal{Z}_1}{\partial y}\cos\theta = \cos\theta\left[\frac{i\varepsilon R_f}{2\pi St}\right]\frac{\partial^2 \mathcal{Z}_0}{\partial xy}$$
$$\left\{1-\exp\left(2\pi iSt\frac{x}{R_f}\right)\right\}\exp[-i\omega t] \tag{53}$$

The mean expression for $\partial \mathcal{Z}/\partial n$ is plotted in Fig. 25 below, along a representative flame surface. Note how the time averaged burning rate is a very strong function of the axial coordinate for non-premixed flames, having a singularity at the flame base, i.e. $x=0$, when axial diffusion is neglected. In contrast, for a premixed flame with no stretch sensitivity, the burning rate is constant (even if there were stretch sensitivity, that correction would only be important at the flame tip).

These results hint at a point which will be emphasized repeatedly – the high transverse gradients near the nozzle exit cause substantial variations in mass burning rate distribution and, moreover, cause the burner exit profile details to dominate the mean and fluctuating heat release characteristics, both locally and spatially integrated. Given these points, and the consequent limitations of the prescribed step inflow boundary condition (Eq. (8) utilized in Model Problems A and B) in describing these near $x=0$ details, the results in the remainder of this section will focus on solutions extracted from Model Problem C, the extended inflow configuration (see Fig. 20) with axial diffusion, closely following the treatment by Magina et al. [95]. The alternate model problems will be returned to while examining various asymptotic characteristics in Section 4.2.

Fig. 26 shows the steady state distribution of heat release per unit area, $q_0(x)$, evaluated along the flame sheet, $\xi_0(x)$, for various Pe values. The cumulative heat release distribution, $q_{0,c}$, is also plotted, defined as:

$$q_{0,c}(x) = \frac{\int_0^x q_0(x)dx}{Q_0} \tag{54}$$

where Q_0 is the total steady state heat release defined as:

$$Q_0 = \int_0^{L_{f,0}} q_0(x)dx \tag{55}$$

Also plotted for reference is the axial distribution for a constant burning velocity premixed flame, indicated by “PM Flame” in the legend. This abbreviation will be used throughout to denote the values for a corresponding premixed flame.

For the steady state distribution, the $Pe\rightarrow\infty$ limiting case has a singularity at the inlet due to the discontinuity in mixture fraction at the burner exit, that can be shown analytically[4] to scale as $\dot{m}''_F \sim x^{-1/2}$, as also shown in Fig. 26 [106]. With finite Pe values, the inlet profile is smoothed and the peak value at $x=0$ is reduced. In addition, the heat release contribution from the tip (where only axial diffusion contributes) increases with decreasing Pe value. Comparing the premixed and non-premixed flame curves shows that half of the average heat release occurs in roughly the first 15–20% of the non-premixed flame, while it occurs at the 50% flame midpoint for the premixed flame. This result clearly shows the need for particular care in accounting for inflow conditions that influence the $x / R_f << 1$ region for non-premixed flame problems.

Fig. 27 shows the corresponding unsteady heat release distribution, $\hat{q}_1(x)$, for various Pe and St values. The cumulative heat release distribution is plotted in Fig. 28 with two different normalizations, defined as:

$$q_{1,c_1} = \frac{\int_0^x \hat{q}_1(x)dx}{\varepsilon Q_0} \qquad q_{1,c_2} = \frac{\int_0^x \hat{q}_1(x)dx}{\int_0^{L_{f,0}} \hat{q}_1(x)dx} \tag{56}$$

The first normalization definition, given by Eq. (56), uses the steady state heat release for normalization so that its value at x

---

[3] Equivalently, Eq. (16) could have been utilized resulting in an alternate form of the fluctuating term: $\frac{\partial \mathcal{Z}_1}{\partial n} = -\frac{\partial \mathcal{Z}_1}{\partial y}\cos\theta = \cos\theta\sum_{n=1}^{\infty}[\frac{i\varepsilon\mathcal{A}_n{}^3(2/n\pi)\sin(\mathcal{A}_n)}{2\pi\, St\, PeR_f}]\sin(\mathcal{A}_n\frac{y}{R_f})\exp(-\mathcal{A}_n{}^2\frac{x}{PeR_f})\{1-\exp(2\pi\, i\, St\frac{x}{R_f})\}\exp[-i\omega t]$

[4] The infinite summation obscures this point from Eq. (52). However, the solutions for the unconfined system, presented in Magina & Lieuwen [95] Magina NA, Lieuwen TC. Effect of axial diffusion on the response of diffusion flames to axial flow perturbations. Combustion and Flame. 2016;167:395-408., make this point easily observable, noting that as $x\rightarrow 0$, $\xi_0\rightarrow R_f$.

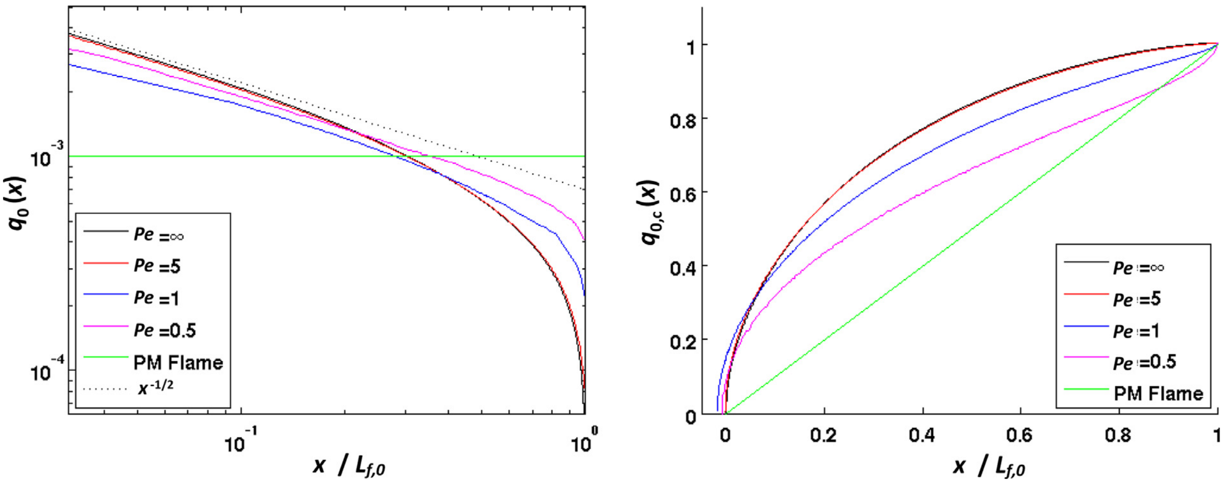

Fig. 26. Local heat release solutions from Model Problem C, showing axial dependence of steady state heat release, both distributed (left) and cumulative (right), for Z_{st}= 0.3 and various *Pe* values (Reprinted from Magina et al. [95] with permission of Elsevier).

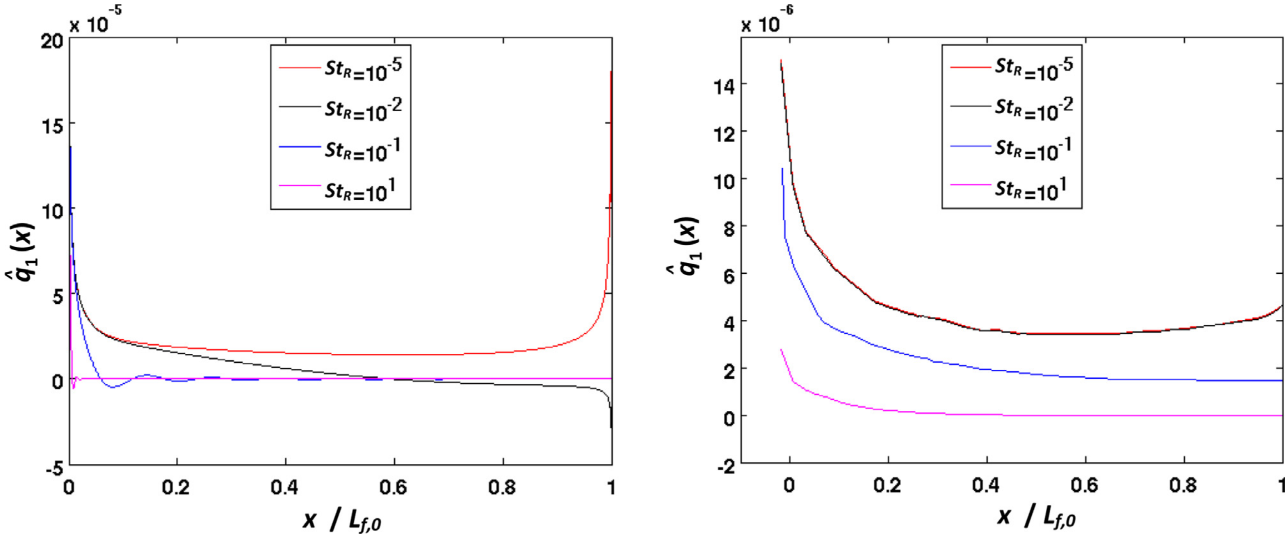

Fig. 27. Local heat release solutions from Model Problem C, showing axial dependence of fluctuating heat release distributions for *Pe* values of 25 (left) and 1 (right) and various values *St* (Reprinted from Magina et al. [95] with permission of Elsevier).

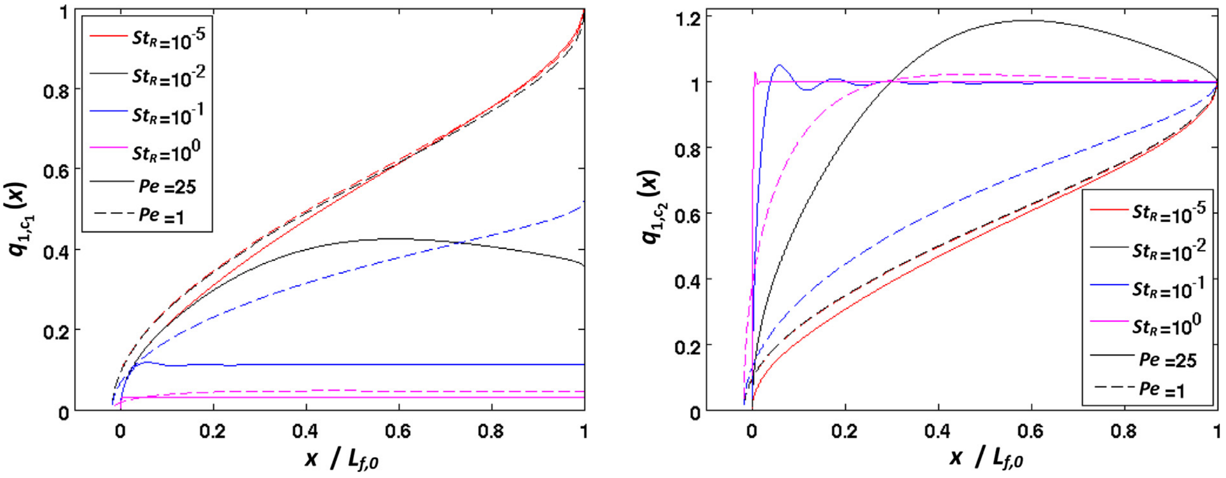

Fig. 28. Local heat release solutions from Model Problem C, showing axial dependence of normalized fluctuating cumulative heat release distributions $q_{1,c1}$(left) and $q_{1,c2}$ (right) for various values of *Pe* and *St* (Reprinted from Magina et al. [95] with permission of Elsevier).

$/ L_{f,0}=1$ corresponds to the flame transfer function's value (discussed in Section 4.2). The second normalization uses the spatially integrated unsteady heat release, so that its value at $x / L_{f,0}=1$ goes to unity, thus allowing for visualization as to which parts of the flame contribute to its unsteady heat release. Fig. 27 shows that for $Pe>>1$ and $St<<1$, the largest values of local fluctuating heat release occur at both the flame base, due to the sharp inlet gradient, and at the flame tip, due to the pulsing flame length. However, neither of these regions contributions to the cumulative heat release are dominant, as shown in Fig. 28. An additional subtlety, as discussed in Section 3.3, for Model Problem C the flame attachment point actually occurs at $x<0$, resulting to some heat release in that region.

For $Pe>>1$ and $St \sim O(1)$ or $>>1$, the local heat release at the tip diminishes, and the largest local values occur at the flame base. Moreover, the cumulative distributions show that the majority of the unsteady heat release occurs at the flame base – a fact which enables the development of simple asymptotic expressions for the $St>>1$ heat release, which is detailed in Section 4.2.1 [95]. The same St trends hold for lower finite Pe values, yet the base and tip (for low St values), contributions are reduced and the middle length of flame has a larger contribution due to axial diffusion.

4.2. Global heat release analysis

Oscillations in heat release generate acoustic waves via unsteady gas expansion, which are manifested as broadband noise and discrete tones, for unconfined and confined flames, respectively [4]. If the combustion region of interest is much smaller than an acoustic wavelength, then disturbances originating from different points in the flame arrive at the measurement location with negligible phase shift. This describes a "compact flame" in which the distribution of the heat release is unimportant; rather the quantity of relevance is the total, spatially integrated value [4]. This spatially integrated quantity is given by the following surface integral over the reaction sheet:

$$\dot{Q}(t) = \int\limits_{flame} q(\vec{x},t)dA = \int\limits_{flame} \dot{m}_F''(\vec{x},t)h_R(\vec{x},t)dA \tag{57}$$

It is useful to define the following (flame) transfer function, which quantifies the magnitude and phase sensitivity of the heat release to flow disturbances:

$$\mathscr{F}(\omega) = \frac{\hat{\dot{Q}}_1(\omega)/\dot{Q}_0}{\hat{\vec{u}}_1/\vec{u}_0} \tag{58}$$

where $\hat{\vec{u}}$ denotes a reference forcing velocity; for example, for axial bulk forcing this transfer function takes the form $\mathscr{F}=(\hat{\dot{Q}}_1/\dot{Q}_0)/(\hat{u}_{x,1}/U_0)$. Alternate definitions can be utilized for the other various heat release coupling mechanisms, such as pressure or equivalence ratio oscillations, where this parameter physically represents an input-output relation between the disturbance fluctuations and the resulting heat release fluctuations. Once again assuming constant composition reactants, as was done in Section 4.1 such that $\hbar_R$ does not vary, the results in Eq. (58) can be decomposed into contributions from mass burning rate and flame area fluctuations; i.e., $\mathscr{F}=\mathscr{F}_{mbr}+\mathscr{F}_{wa}$. This can be done by linearizing and expanding Eq. (48) as:

$$\dot{Q}(t) = \hbar_R \left[\underbrace{\int\limits_{flame} \dot{m}_{F,0}''\, dA_0}_{\dot{Q}_0} + \underbrace{\int\limits_{flame} \dot{m}_{F,1}''\, dA_0}_{\dot{Q}_{mbr}(t)} + \underbrace{\int\limits_{flame} \dot{m}_{F,0}''\, dA_1}_{\dot{Q}_{wa}(t)} \right] \tag{59}$$

which implicitly defines the fluctuating heat release as $\dot{Q}_1(t)=\dot{Q}_{mbr}(t)+\dot{Q}_{wa}(t)$.

The first term in Eq. (59) represents the mean spatially integrated heat release, similar to Eq. (55). The second term defines the mass burning rate term. For non-premixed flames, this contributes to heat release oscillations due to the fluctuations in spatial gradients of the mixture fraction. For premixed flames, the mass burning rate fluctuations are linked to the stretch sensitivity of the burning velocity (or due to oscillations in mixture composition), which fluctuates because of the oscillatory curvature of the wrinkled front [110]. The last term in Eq. (59) is a fluctuating area term, weighted by the time averaged burning rate. As discussed above (see Fig. 25 and Fig. 26), a major difference between the heat release response of premixed and non-premixed flames is that this weighting term is essentially a constant for premixed flames, whereas it varies strongly for non-premixed flames. If the time averaged burning rate is constant (a commonly studied case for premixed flames), then this term is given by:

$$Constant\ \dot{m}_{F,0}''\ (\text{“}unweighted\text{”}): \quad \dot{Q}_a(t) = \hbar_R \dot{m}_{F,0}'' \int\limits_{flame} dA_1 \tag{60}$$

There are significant variations in time-averaged heat release rate along the non-premixed flame (e.g., no heat release at the tip in the absence of axial diffusion, see Fig. 26), thus the weighting of flame area is a very significant effect influencing how area fluctuations lead to heat release. Indeed, it is common in premixed flame studies to directly equate heat release fluctuations to flame area fluctuations [8, 9, 11, 113]. However, this is not the case in non-premixed flames and is responsible for several critical differences in the heat release dynamics of these forced flames; even while Section 3 showed significant similarities in the space-time wrinkle dynamics of premixed and non-premixed flames, this section will show that their heat release dynamics are fundamentally different.

For example, the characteristics of the weighted, $\dot{Q}_{wa}(t)$, and un-weighted, $\dot{Q}_a(t)$, area transfer functions are essentially the same for premixed flames. In contrast, they are quite different for non-premixed flames, as illustrated by reference to a quasi-steady argument in Fig. 29. The first plot (on the left) shows the non-premixed mean flame position for two different mean flow velocities. As is expected, the higher velocity case produces a flame with a larger total area. However, Fig. 25 and Fig. 26 showed that for non-premixed flames, the near base-region is of greater importance, containing the dominant portion of the mean mass burning rate. Significantly, restricting our attention to the near-base region of the flame, i.e. the white region in Fig. 29, it can be observed that the resulting (weighted) area actually decreases with increasing mean flow velocities. The second plot (on the right) shows how for low forcing frequencies, the area contribution is in-phase with the velocity forcing, while the weighted area contribution is 180° out of phase – in other words, in the low Strouhal number limit, the non-premixed flame weighted and un-weighted area transfer functions differ in phase by 180° and have appreciably different magnitudes.

For the two-dimensional system considered in Section 3.1 thru 3.3, Eq. (57) can be written as:

$$\dot{Q}(t) = \int\limits_0^{L_f(t)} \frac{(1+\varphi_{Ox})^2}{\varphi_{Ox}} \rho \hbar_R \mathscr{D} \left(\frac{\partial \mathcal{Z}(x,\xi(x,t))}{\partial x} \frac{\sin\theta}{\cos\theta} - \frac{\partial \mathcal{Z}(x,\xi(x,t))}{\partial y} \right) dx \tag{61}$$

where the differential area is projected onto the axial direction. Furthermore, neglecting the axial diffusion terms, decomposing $\mathcal{Z}$, L_f, and ξ into their mean and fluctuating components, and lineariz-

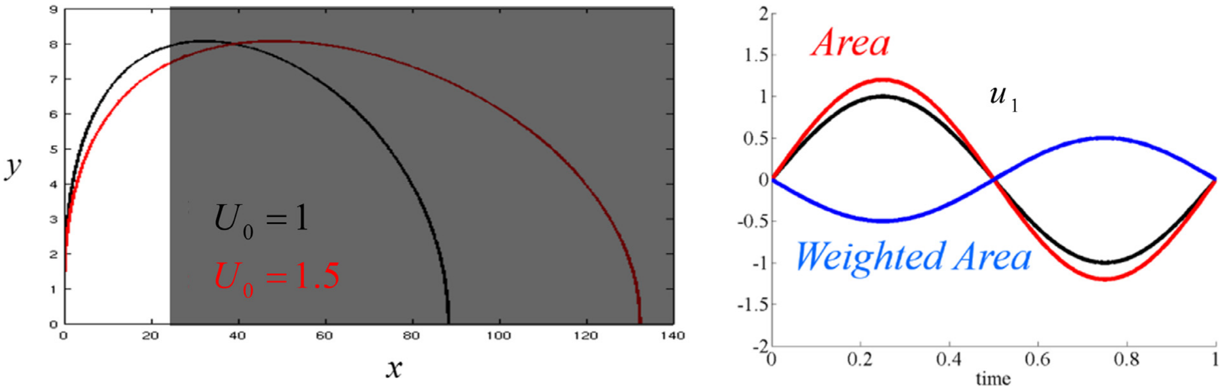

Fig. 29. Plots illustrating the behavior of the weighted area and area transfer functions by comparing quasi-steady area variations for two flow velocities. (left) Shows mean flame positions for two different mean flow velocities and (right) shows the fluctuations over one forcing cycle for the various terms.

Table 7
Heat release asymptotic result summary denoting roll off and transition values for the model problems listed in Table 4 [95].

Model Problem	$St << 1$, $Pe >> 1$	St_1	$St_1 < St < St_2$	St_2	$St >> 1$
A, B	$\mathcal{F} \sim 1$	$St_1 = 1/8$	$\mathcal{F} \sim 1/\ (St^{1/2})$	N/A	
C, D	$\mathcal{F} \sim 1$	$St_1 = 1/8$	$\mathcal{F} \sim 1/\ (St^{1/2})$	Eq. (76)	$\mathcal{F} \sim 1/St$

ing, results in[5]:

$$\dot{Q}(t) = \frac{-(1+\varphi_{Ox})^2}{\varphi_{Ox}}\rho h_R \mathcal{D}\left\{\underbrace{\int_0^{L_{f,0}} \frac{\partial \mathcal{Z}_0}{\partial y}dx}_{\dot{Q}_0} + \underbrace{\int_0^{L_{f,0}} \frac{\partial \mathcal{Z}_1}{\partial y}dx + \int_0^{L_{f,0}} \xi_1 \frac{\partial^2 \mathcal{Z}_0}{\partial y^2}dx}_{\dot{Q}_1(t)}\right\} \tag{62}$$

where the terms in brackets at each x location are evaluated at $y = \xi_0(x)$. The steady and fluctuating components are given by $\dot{Q}_0$ and $\dot{Q}_1(t)$, respectively. Note that fluctuations in L_f do not contribute to this linearized expression since $\partial \mathcal{Z}_0/\partial y$ is zero along the centerline and, therefore, at the flame tip if axial diffusion is neglected. The expressions including axial diffusion are much longer, including the additional set of terms related to $\partial \mathcal{Z}_0/\partial x$ from Eq. (51), and are presented in Magina et al. [93].

4.2.1. *Asymptotic transfer function characteristics*

Before presenting computational and experimental results for flame transfer functions, it is useful to consider various asymptotic limits and the processes controlling these limits. The various asymptotic limits for the four model problems listed in Table 4, as well as the Strouhal number demarcating the various limiting regimes, are summarized in Table 7.

The singularity in mixture fraction gradient in Model Problem A near $x = 0$ was shown to be of the form $x^{-1/2}$, and integrable – for this reason, significant insight into the spatially integrated heat release characteristics can be obtained from this simplest model problem. Utilizing Eq. (58) and the results from Section 3.1, the transfer function can be written as:

$$\textit{Model Problem A}: \quad \mathcal{F} = \frac{\int_0^{L_{f,0}{}_-^+} \left[\frac{-iR_f}{2\pi St}\right] g(x,\xi_0)\left\{1-\exp\left(i2\pi St\frac{x}{R_f}\right)\right\}dx}{\varepsilon\int_0^{L_{f,0}{}_-^+}\frac{\partial \mathcal{Z}_0(x,\xi_0)}{\partial y}dx} \tag{63}$$

where $g(x, \xi_0)$ is an axial distribution function defined as:

$$g(x,\xi_0) = \tan(\theta_0)\frac{\partial^2 \mathcal{Z}_0(x,\xi_0)}{\partial y^2} + \frac{d^2 \mathcal{Z}_0(x,\xi_0)}{dxdy} \tag{64}$$

Expanding $\mathcal{F}$, as given by Eq. (63), in powers of St, leads to [95]:

$$St << 1 \quad \mathcal{F} = 1 + iSt_{L_f}\frac{2\pi\int_0^{L_{f,0}} x\frac{\partial \mathcal{Z}_0(x,\xi_0(x))}{\partial y}\cdot dx}{L_{f,0}\int_0^{L_{f,0}}\frac{\partial \mathcal{Z}_0(x,\xi_0(x))}{\partial y}\cdot dx} + O\left(St_{L_f}^2\right) \tag{65}$$

Significantly, $|\mathcal{F}| = 1 + O(St^2)$ for $St_{Lf} << 1$. This value of unity can be understood physically from the fact that in the quasi-steady limit, the instantaneous heat release is proportional to the instantaneous mass flow rate of fuel and oxidizer into the combustion domain, i.e. across the inlet plane; in other words, a 1% fluctuation in velocity induces a 1% fluctuation in heat release [4]. For the same reason, there is no unsteady heat release induced by transverse bulk forcing, i.e. $\mathcal{F} = 0$, however, this conclusion applies for all Strouhal numbers. The justifications for these gain results apply for the same reasons to premixed flames. The transfer function gain need not converge to unity for Model Problems B, C, and D, because axial diffusion causes the convective and total mass flow rate to differ. However, it asymptotes to unity in the limit of $Pe >> 1$ for all the model problems.

A common unsteady heat release model used in larger thermoacoustics systems dynamics models is the η-τ model [115], where the unsteady heat release is related to the velocity through a gain, η, and time delay, τ, given by:

$$\dot{Q}_1(t)/\dot{Q}_0 = \eta u_1(t-\tau)/U_0 \tag{66}$$

or, equivalently written in terms of a transfer function as:

$$\mathcal{F} = \eta \exp[i\omega\tau] \tag{67}$$

We can use the above result to determine these η-τ parameters for non-premixed flames in the $St << 1$ limit. Inspecting Eq. (65), the gain is unity, i.e. $\eta = 1$, and the time delay is given by:

$$\tau = \left[\frac{\int_0^{L_{f,0}} x\frac{\partial \mathcal{Z}_0(x,\xi_0(x))}{\partial y}\cdot dx}{L_{f,0}\int_0^{L_{f,0}}\frac{\partial \mathcal{Z}_0(x,\xi_0(x))}{\partial y}\cdot dx}\right]\frac{L_{f,0}}{U_0} \tag{68}$$

This time delay is equivalent to replacing the distributed flame by a concentrated source at some fractional distance of the flame

---

[5] Comparing the terms in this expression to Eq. (58), there is an additional term, $\partial \mathcal{Z}_0/dx\sin(\theta_1)$, having equal and opposite magnitude in the mass burning rate and weighted area terms, thus cancelling in the Q_1 expression shown, as demonstrated by Magina *et al.* [93] Magina N, Acharya V, Sun T, Lieuwen T. Propagation, dissipation, and dispersion of disturbances on harmonically forced, non-premixed flames. Proc Combust Instit. 2015;35:1097-105..

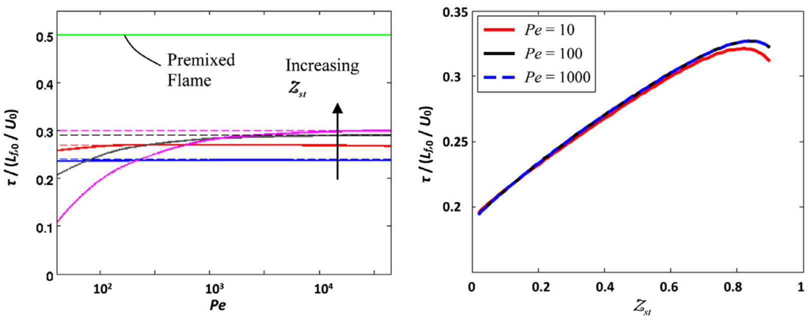

Fig. 30. Dependence of normalized time delay parameter, $\tau/(L_{f,0}/U_0)$ upon (left) *Pe* for various $\mathcal{Z}_{st}$ values (0.3, 0.6, 0.8, 0.9) for Model Problem C. The corresponding (based on geometry, assumptions, and configuration) premixed flame value is also displayed. For each $\mathcal{Z}_{st}$ value, the corresponding Model Problem A, i.e. $Pe \to \infty$, solution is shown by a dashed line. (right) Dependence upon $\mathcal{Z}_{st}$ for various *Pe* values.

length. While the gain is straightforward, the time delay is a complex function of parameters such as *Pe* and $\mathcal{Z}_{st}$, discussed in more detail by Magina [106]. These parametric dependencies of τ cannot be calculated analytically but must be extracted from the computations due to the implicit nature of the solution for mean flame position, at which these integrand values are evaluated.

Fig. 30 plots calculations of $\tau/(L_{f,0}/U_0)$ as a function of *Pe* and $\mathcal{Z}_{st}$ [95]. The corresponding constant burning velocity, premixed flame value is also plotted for reference. The solid lines indicate the numerical extended inlet results, i.e. Model Problem C, while the dashed lines show the corresponding $Pe \to \infty$ analytical results, given by Eq. (68), i.e. Model Problem A.

Note that the time delay value (normalized by $L_{f,0}$ / U_0), for example, is around 0.2 for a methane-air, non-premixed system, which has a $\mathcal{Z}_{st}$ value of 0.055 (see Table 3). For reference, the constant burning velocity two-dimensional bulk axially forced premixed flame result is $\tau/(L_{f,0}/U_0) \approx 0.5$ (assuming the flow velocity is much greater than the flame speed), showing that the non-premixed flame time delay is about a factor of two smaller than a premixed flame with the same length. This result directly follows from the concentration of heat release near the burner outlet, and the distributions shown in Fig. 26.

Additionally, in the low *St* limit, the ratio of weighted area contributions relative to mass burning rate contributions to the transfer function gain is of order $O(1/Pe^2)$ [95] – i.e., mass burning rate contributions dominate the unsteady heat release in $Pe >> 1$ flames. This point will be returned to in the next section.

Having considered the $St << 1$ limit of $\mathcal{F}$, we next consider the large *St* limit. Recall, Section 4.1 (see Fig. 28) showed that the high *St* limit, Eq. (63) was controlled by the features of $g(x, \xi_0)$ near $x = 0$ [95]. This fact can be exploited to expand Eq. (64) around $x = 0$ which, following Magina [106], becomes:

$$g(x, \xi_0) = \frac{1}{4\sqrt{R_f\pi/Pe}\,x^{3/2}} + O\left(x^{-1/2}\right) \tag{69}$$

Substituting this expression into Eq. (63) leads to the following large *St* result:

$$St >> 1 \quad \mathcal{F} \approx \frac{-(1+i)}{4\sqrt{St_{L_f}}} \tag{70}$$

This shows that the phase between the velocity and heat release has a constant value of 45° and that the gain rolls off as $1/(St^{1/2})$. As the flame transfer function amplitude was shown to be unity in the limit of low *St* values, the Strouhal number at which this first transition occurs, denoted St_1 in Table 7, from O(1) to $O(St^{-1/2})$, can be obtained via the intersection of these limits, as $St_1 = 1/8$. As shown in the next section, the $1/(St^{1/2})$ behavior of the heat release transfer function is a much slower roll off than the $1/St$ roll off that occurs to leading order in premixed flames, causing the heat release response of non-premixed flames to exceed that of premixed flames at high Strouhal numbers for this problem.

Recall, however, that $g(x, \xi_0)$, given by Eqs. (64) and (69), was obtained for Model Problem A, i.e. solutions in the $Pe \to \infty$ limit (no axial diffusion) utilizing the step inlet boundary, Eq. (8). There exists a third, even higher *St* asymptotic zone, that cannot be analyzed without inclusion of more realistic species inflow profiles. Note that oscillatory integrals of the following form:

$$\int_{x_1}^{x_2} f(x)\exp(iStx)\,dx \tag{71}$$

are controlled by the values of the integrand at the boundary, i.e., at $f(x_1)$ and $f(x_2)$, and generally lead to a $1/St$ asymptotic behavior. However, for Model Problems A and B the mass burning rate has an integrable singularity at the $x = 0$ inlet boundary due to the infinite transverse gradient in $\mathcal{Z}$ imposed by the step inlet boundary condition, a singularity that ends up controlling the heat release asymptotics, leading to the indicated $1/(St^{1/2})$ behavior. In other words, this singularity controls this asymptotic trend and causes it to exhibit a $1/St^{1/2}$ rather than a $1/St$ asymptotic behavior. Note, how this is still valid for Model Problem B, where axial diffusion effects were included in the governing equation, i.e. $b = 1$ in Eqs. (9) and (10). When axial diffusion effects are included and the inlet profile mixture fractions are not discontinuous, i.e., Model Problems C or D (discussed next), this $1/(St^{1/2})$ behavior persists for a range of Strouhal numbers where the convective wrinkle wavelength, U_0 / ω, is much longer than the thickness of the transition zone of fuel/oxidizer profiles at $x = 0$. However, once the convective wavelength becomes of the order of this layer, the standard $1/St$ behavior occurs, as expected for these oscillatory integrals. Thus, the Strouhal number at which the $1/St^{1/2}$ to $1/St$ transition occurs is a function of the thickness of this layer, which in turn, is a function of *Pe*.

This point can be demonstrated explicitly through Model Problem D, which excludes axial diffusion from the governing equation, but utilizes a finite thickness $\mathcal{Z}_0$ inlet transition layer, parameterized by δ [95]. In reality, the non-dimensional profile thickness parameter, δ, simulates the extent to which axial diffusion has altered the inlet boundary condition, and is proportional to the inverse of *Pe*. Fig. 31 demonstrates this point explicitly by showing extracted profile thicknesses from Model Problem C, for various *Pe* values, where δ is measured as the distance from $0.95 \times \mathscr{f}_0(y = 0)$ to $0.05 \times \mathscr{f}_0(y = 0)$ normalized by R_f.

Returning to Eqs. (63) and (64), which remain valid for this Model Problem formulation, the function $g(x, \xi_0)$ is given for the

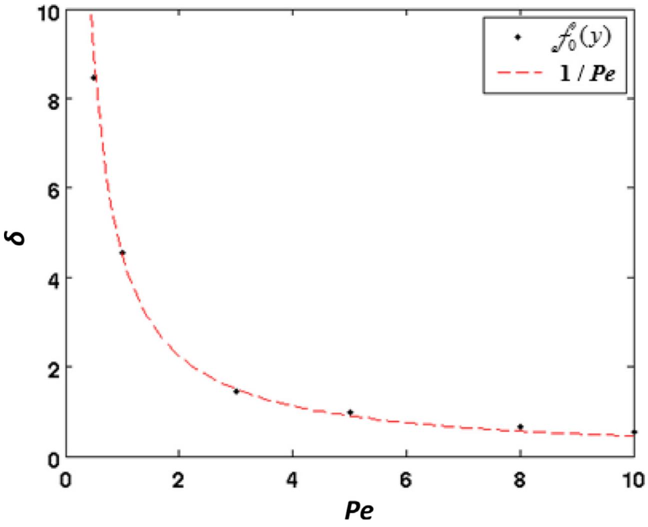

Fig. 31. Non-dimensional inlet profile thickness for Model Problem C, at select *Pe* values, for $R_w/R_f = 10$.

smoothed, piecewise-linear profile (visualized in Fig. 7) as [95]:

$$g(x,\xi_0) = \frac{1}{2x^{3/2}\sqrt{R_f\pi/Pe}} + \frac{1}{4\delta x} \tag{72}$$

Substituting this expression into Eq. (63) reveals that in the limit of large *St* :

$$St >> 1 \quad \mathcal{F} = \frac{C_1}{\sqrt{St_{L_f}}} + \frac{C_2}{St_{L_f}}\frac{1}{Pe\delta}\sqrt{\frac{PeL_f}{R_f}} \tag{73}$$

where

$$C_1 = \frac{-(1+i)}{4} \qquad C_2 = \frac{i\left[\lambda - 4\sqrt{\pi}\right]}{16\sqrt{\pi}} \tag{74}$$

and λ is Euler's constant, with numerical value $\lambda \simeq 0.577216$. Note how the leading order $St >> 1$ term is $O(1/St^{1/2})$, consistent with Eq. (70), while the next term is of $O(1/St)$. Thus, while a $1/St^{1/2}$ behavior occurs for the step inlet function profiles, a smooth mixture fraction at the base of the flame (resulting from finite *Pe* value effects) leads to the $1/St$ asymptotic behavior that one would expect of highly oscillatory integrals. For this model problem, we can develop an explicit expression for the Strouhal number at which the $1/St^{1/2}$ to $1/St$ transition occurs, denoted as St_2, by equating these two terms:

$$St_2 = \left(\frac{|C_2|}{|C_1|}\right)^2 \frac{1}{Pe^2\delta^2}\frac{PeL_f}{R_f} \tag{75}$$

Physically, this transition Strouhal number coincides with conditions where the convective disturbance wavelength is on the order of the axial extent required for fuel/oxidizer to diffuse across the inlet transition layer.

As was stated previously, the profile thickness parameter, δ, is proportional to the inverse of *Pe* under these conditions, a point which should make sense as the inlet profile, f_0, steepens and becomes thinner, as *Pe* is increased, converging to a step function in the $Pe\to\infty$ limit. Thus, if we substitute in $\delta\sim 1/Pe$ into Eq. (75), this shows that:

$$St_2 = \left(\frac{|C_2|}{|C_1|}\right)^2 \frac{PeL_f}{R_f} \tag{76}$$

4.2.2. Transfer function characteristics

Having considered the asymptotic tendencies of, $\mathcal{F}$, we next present computed and measured results. The majority of the calculated results are investigated numerically, due to the implicit nature of the flame location at which the values of the integral, i.e. Eq. (57), are evaluated at. Fig. 32 plots the computed amplitude and phase of $\mathcal{F}$ as a function of *St* for various *Pe* values, for Model Problem C, as well as the $Pe\to\infty$ result, for Model Problem A. For the amplitude, the most prominent difference between the results which include and neglect axial diffusion are the asymptotic characteristics discussed in Section 4.2.1; Model Problem A having a two-zone structure, while Model Problem C results show a three-zone asymptotic structure. The phase plot also shows some differences between the results, although they all appear qualitatively similar.

The solutions for the premixed flame transfer functions are simpler, as the unforced flame is flat in a uniform velocity field. Following Wang et al. [110], and retaining only leading order terms in Markstein length, the transfer function is given by:

$$\mathcal{F}_P = \underbrace{\left\{\hat{\sigma}_c\left(1+2\pi i St_p\hat{\sigma}_c\right)\left(1-e^{2\pi i St_p-4\pi^2\hat{\sigma}_c St_p^2}\right)\right\}}_{=\mathcal{F}_{P,mbr}} + \underbrace{\left\{-1/\left(2\pi i St_p\right)\left(1-e^{2\pi i St_p-4\pi^2\hat{\sigma}_c St_p^2}\right)\right\}}_{=\mathcal{F}_{P,a}} \tag{77}$$

where $\hat{\sigma}_c$ is given by $\hat{\sigma}_c = \sigma_c \sin\theta\tan\theta$.

Typical solutions for the overall unsteady heat release, as well as the contributions from flame area and mass burning rate, are shown in Fig. 33 for the non-premixed and premixed flame for Model Problem A. Both premixed and non-premixed transfer functions have magnitudes of identically unity at zero *St*, consistent with the η-τ discussion regarding Eq. (68), indicating the direct 1:1 relation between the fluctuation in velocity and induced fluctuation in heat release, and then roll off with increasing *St*, indicating a progressively smaller induced heat release fluctuation [4].

However, the dominant contributors to heat release are completely different. Starting with the left plot, note how the non-premixed flame heat release fluctuations for $St < < 1$ are dominated by mass burning rate fluctuations over the entire Strouhal number range (the ratio of mass burning rate to area contributions from the unsteady heat release being $O(Pe^2)$ in the low *St* limit [106]). In contrast, premixed flames at low and O(1) Strouhal numbers are dominated by area fluctuations, shown in the right plot. The mass burning rate fluctuations are a much smaller effect and only exert a comparable response as area fluctuations at high Strouhal numbers where $St_p \sim O(\hat{\sigma}_c^{-1})$[110].

Direct comparisons of the gain and phase response of the premixed and non-premixed flame results are shown in Fig. 34. Notably, these results show that non-premixed flames are significantly more sensitive to flow perturbations than premixed flames when $St_{L_f} > O(1)$, an important conclusion, and due to the fact that for $St > O(1)$, non-premixed flames roll off initially as $1/St^{1/2}$, while premixed flames go as $1/St$, as discussed in Section 4.2.1.

The corresponding phases of the premixed and non-premixed flame transfer functions are also included in Fig. 34. Both curves start at zero for low Strouhal numbers, indicating that low fre-

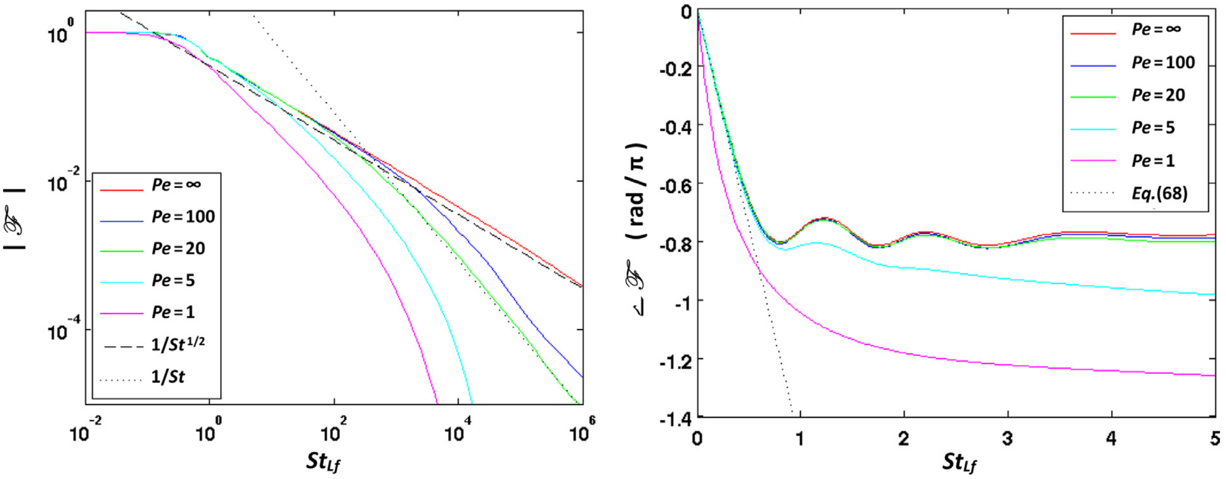

Fig. 32. Model Problem C results, showing heat release transfer function amplitude (left) and phase (right) as a function of St_{Lf} for Z_{st}= 0.3 for various Pe values. The $Pe\to\infty$ result from Model Problem A is also shown for comparison (Reprinted from Magina et al. [95] with permission of Elsevier).

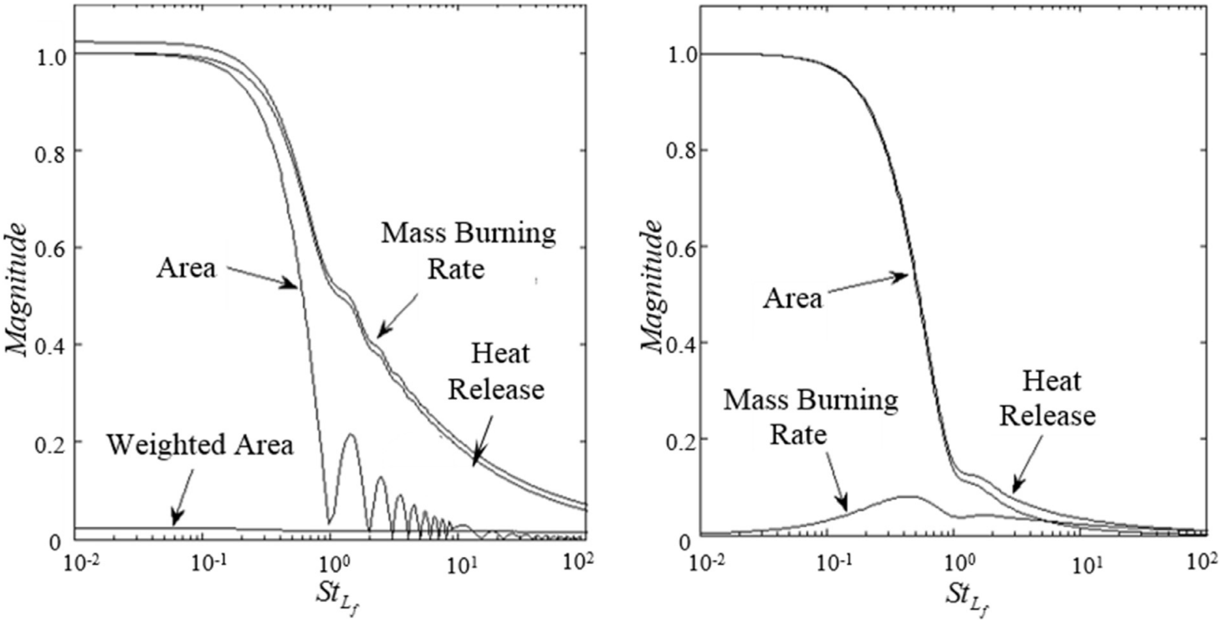

Fig. 33. Model Problem A results, showing the Strouhal number dependence of the magnitude of the heat release, area, and mass burning rate transfer functions for a (left) non-premixed flame with parameters $Z_{st}=0.06, Pe=10$, and (right) premixed flame with parameters $\hat{\sigma}_c$ = 0.05 and L_f/R_f= **932**(Reprinted from Magina et al. [92] with permission of Elsevier).

quency flow modulation induces heat release fluctuations that are in phase. The curves roll off with different slopes toward negative values and asymptote to −90° for the non-premixed flame and −45° for the stretch sensitive, premixed flame. This phase is a manifestation of the delay in heat release relative to the forcing, due to convection of disturbances along the front. Note also the nearly constant phase (at −45°) in the non-premixed flame in the intermediate Strouhal number range discussed above. The undulations in phase for the premixed flame correspond to ripples in the gain, and reflect the influence of interference processes in controlling the flame area. The differences in phase between the two flames again reflects the different processes controlling unsteady heat release.

Although limited in quantity, other researchers have measured transfer functions of a forced experimental system [33] – a key difference from the above results being that the experiments are for a round jet. Fig. 35 shows a measured flame transfer function gain comparison (see Kim et al. for phase [33]) with analytical results, specifically Eq. (63) for Model Problem A. The differing fuel compositions alter the details of the gain and phase oscillations, reflected as different Z_{st} values in the analytical study, however the trends remain comparable. The gain results are certainly consistent with the predicted O($1/St^{1/2}$) trends from expressions above, i.e. Eq. (70). It is not possible to directly compare the low St values; in addition, for these experiments the flames were highly corrugated and even multi-connected with high degrees of clipping. Note that no transition to the predicted $1/St$ is observed in these data; this is likely due to the fact that this transition occurs at a Strouhal number that is larger than where data was acquired (our estimate of St_2 using Eq. (76) and quoted flame lengths is $St_2=190$).

We close this section by considering bulk transverse forcing of the flame. Unlike the space-time dynamics conclusions from Section 3, where flame wrinkling was fundamentally the same with a subtle change in the forcing-flame front orthogonal direction, the heat release results are quite different. In this configuration, in the $Pe\to\infty$ limit, for all St values the area and mass burn-

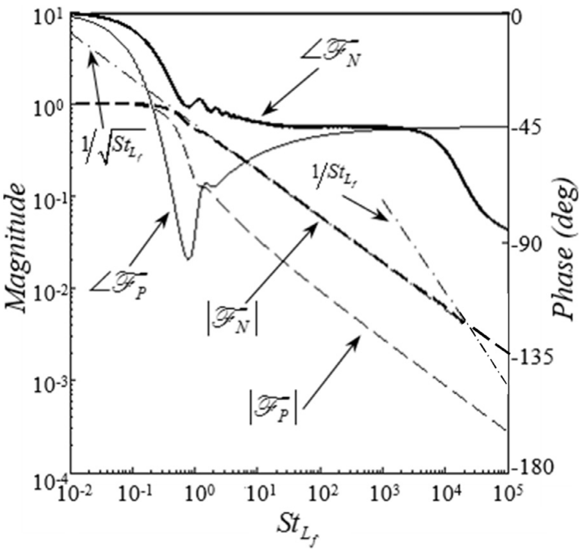

Fig. 34. Strouhal number dependence of the magnitude and phase of the heat release transfer function for a non-premixed and premixed flame with the same properties as Fig. 33 (Reprinted from Magina et al. [92] with permission of Elsevier).

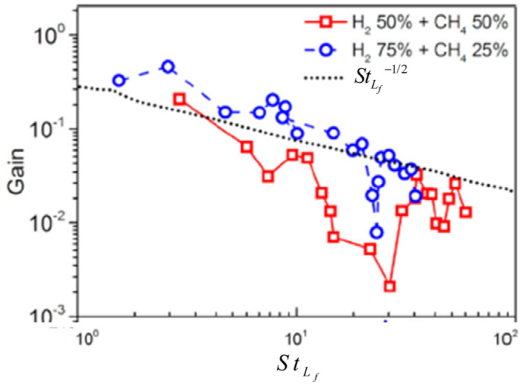

Fig. 35. Non-premixed flame transfer function gain comparison at 1.0 m/s for the analytical [93] and experimental [33] results (Reprinted from Kim et al. [33] with permission of Elsevier).

ing rate contributions from the two branches have the same magnitude but are out of phase by 180°, resulting in no unsteady heat release for one-half of the flame [93, 96]. This result could be anticipated, at least in the low Strouhal number limit, as transverse forcing causes no fluctuation in fuel and oxidizer flow rate into the domain. Since the heat release in the quasi-steady limit is directly proportional to the fuel flow rate into the domain, transverse fluctuations consequently lead to no heat release oscillations. Similar conclusions were developed for transversely forced premixed flames by Acharya et al. [113]. Significantly, this point emphasizes the important distinction between local and global heat release fluctuations. As was discussed in Section 4.1, even though there are no global heat release fluctuations, the local heat release by each segment of flame is fluctuating, as is the instantaneous flame position.

4.2.3. Round jet characteristics

This section presents the transfer function characteristics of round jets exposed to disturbances and compliments Section 3.4, which identified several canonical forcing configurations, characterized by the forcing velocity field sets shown in Table 6 - bulk axial, bulk transverse, and convecting helical disturbances. For bulk axial fluctuations, the flame transfer function for the round jet is qualitatively similar to that summarized above in the two-dimensional analysis. For the transversely forced configuration, similarly to the two-dimensional case, heat release oscillations cancel each other on opposite sides of the flame, thus resulting in no unsteady heat release. For helical disturbances, this same cancellation occurs for all mode numbers except for the $m=0$, axisymmetric mode. Thus, as is the case for premixed flames, the $m=0$ mode is the sole contributor to the heat release oscillations, with k_c (see disturbance form in Table 6) being the only new parameter influencing the transfer functions [112]. Moreover, the flame transfer function is not explicitly a function of the swirl (although, implicitly the unforced flame position is). Thus, the final discussion of this section presents analytical results for the response of a jet flame to a convecting, axisymmetric disturbance. Note that the axial bulk case corresponds to $k_c=\infty$.

Fig. 36 shows heat release transfer function magnitude and phase results from the three-dimensional variant of Model Problem A for various values of k_c, the normalized disturbance phase speed. It shows that the gain starts at unity and rolls off, with the details of the roll off varying with disturbance phase speed. The modulation in gain and phase reflects the influence of interference between phase cancellation/reinforcement of different regions on the flame.

Recall from Section 3.4.1, specifically Eq. (47), that for a swirling flow, a non-axisymmetric mode, m_s, dominated the flame wrinkle response amplitude [106]. This is significant given the fact that only the axisymmetric mode, $m=0$, contributes to the global spatially integrated heat release fluctuations. Thus, different measures of the flame response, such as local wrinkling, local heat release, and global heat release, have very different sensitivities to swirl and different azimuthal modes.

5. Concluding remarks

It has been discussed how velocity forcing of non-premixed flames leads to the excitation of wrinkles that convect downstream and lead to local and spatially integrated heat release fluctuations. The amplitude of these wrinkles is proportional to the magnitude of flow displacement fluctuations normal to the flame sheet. As these wrinkles are excited at every point along the flame with velocity fluctuations, the resultant flame wrinkle amplitude at any given position is superposition of the upstream forcing history, convection velocity of the flame, and decay rate of a given wrinkle. This leads to constructive and destructive interference behavior, causing flame wrinkling amplitude magnitudes to oscillate with downstream distance. Similarly, the convection of wrinkles by the flow, causes the phase of flame wrinkles to roll off roughly linearly with axial distance. While the resultant superposition of wrinkles can become more analytically complex when the forcing is three-dimensional (e.g., a helical vortex), and the flow is swirling (causing wrinkles to convect both azimuthally and axially), the basic physics remains the same. There are numerous analogies of these flame wrinkle behavior characteristics to premixed flames, and this review compares and contrasts these results throughout. The key difference between the premixed and non-premixed flame is that premixed flames propagate normal to themselves, which modifies the convection speed of a flame wrinkle causing it to differ from that of the local flow velocity, while non-premixed flames do not. Once wrinkles are excited on the flame, they decay at a rate that increases quadratically with frequency. In non-premixed flames, this occurs because of diffusion smoothing out space-time variations in mixture fraction, while in premixed flames with positive Markstein lengths, this occurs because of the dependence of the flame speed on curvature.

Local heat release on the flame is directly proportional to the local mass consumption rate of reactants. In non-premixed flames,

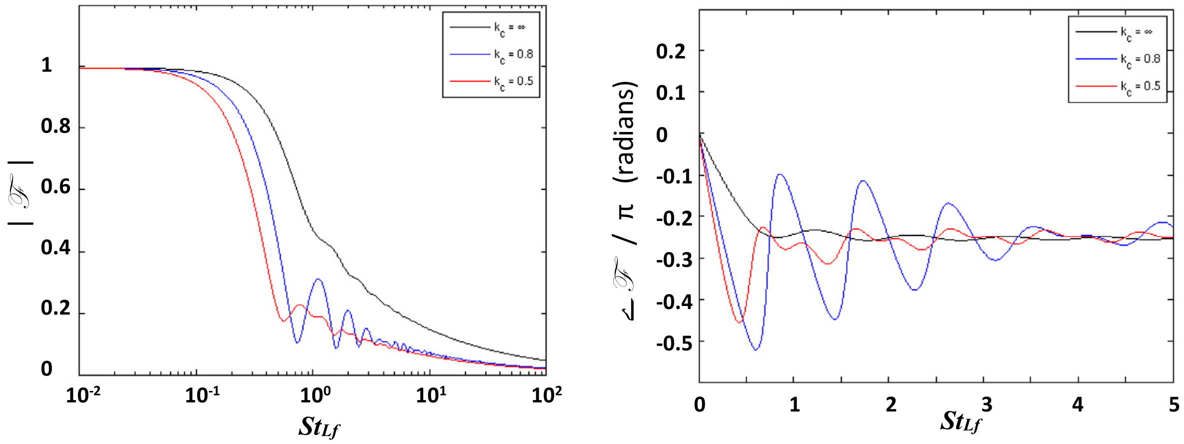

Fig. 36. Convecting helical disturbance heat release transfer function magnitude (left) and phase (right) curves from Model Problem A for various values of k_c and parameters $Pe = 100$, $\varepsilon = 0.01$, $s = 0.1$, and $Z_{st} = 0.3$. The axial bulk case corresponds to $k_c = \infty$. .

the mass consumption rate is directly proportional to gradients in mixture fraction. These gradients can be very high near the burner outlet, where previously separate fuel and oxidizer species first meet, but smooth out with downstream distance. This causes the local mass burning rate to vary substantially in non-premixed flames in the axial directions, with the largest values encountered in the near-burner outlet region. In contrast, the mass consumption rate of premixed flames is proportional to the flame consumption speed which, except in highly curved/strained regions of the flame, is essentially constant. As such, the axial distribution of heat release in a premixed flame can be much more uniform than a non-premixed flame. These factors, in turn, directly influence the spatially integrated heat release, which is controlled by the near-burner outlet region in non-premixed flames and is more uniform in premixed flames. In the low Strouhal number regime, this causes the time delay between a velocity perturbation and the resultant heat release to be substantially shorter for non-premixed flames than premixed flames. Additionally, at low Strouhal numbers, the heat release is directly proportional to mass flow rate of reactants into the combustor domain for both non-premixed and premixed flames, causing their gain values to both have the same unity value. For the same reason, transverse forcing causes local flame wrinkling and heat release fluctuations, but no spatially integrated heat release fluctuations. The near discontinuity in mixture fraction also dominates the high frequency response of non-premixed flames, causing it to roll off as $1/St^{1/2}$. This leads to a much slower roll off of non-premixed flame gain with frequency than premixed flames, which roll off as $1/St$. Only at much higher Strouhal numbers, where the mixture fraction gradient becomes of the same order of magnitude as the convective wavelength, does the non-premixed gain roll off as $1/St$. These asymptotic tendencies of the non-premixed flame, as such, are largely controlled by the near burner exit region with high transverse gradients, and thus, are expected to be quite sensitive to burner exit details and finite chemistry effects (which would lead to extinction)).

We close this review with suggestions for needed future work. Starting with modeling efforts, it is worth highlighting two key assumptions made in the model problems considered - constant diffusivity and infinite chemistry. Understanding the dynamics of forced flames with relaxation of these assumptions will be very interesting. Previous studies have found that finite rate effects have little to no effect on the natural flickering dynamics of non-premixed flames [116], and it seems unlikely that they would influence the basic wrinkle dynamic characteristics presented here, i.e. convection, dissipation, and dispersion. However, finite chemistry will thicken the flame, introducing additional chemical time delays and flame extinction near the burner outlet, where the largest gradients in mixture fraction and heat release occurs. Pushing the region of heat release downstream, where there is less spatial variation in heat release, would introduce significant differences to the results shown here, such as potentially eliminating the $1/St^{1/2}$ region of the transfer function. Similarly, it will be very interesting to determine what fundamental new characteristics appear with non-equidiffusive species. Lastly, alternate flame configurations, such as the unconfined jet and jet-in-crossflow, need further investigation, being of extreme relevance and potentially having more simplified analytical solution forms.

Experimentally, it is evident that there is a strong need for further studies. There is no analogue in the forced non-premixed literature to the enormous number of studies that have been reported in laminar and turbulent premixed flames, with a wide variety of configurations. Such studies are clearly needed. Foundational laminar studies are needed with different Damkohler numbers to provide benchmarking data on frequency effects, configuration effects, and finite chemistry effects. Following such work, analysis of turbulent non-premixed flames should be investigated – again over a range of forcing, configuration, and kinetic parameters are needed, but where turbulence intensities and length scales can be systematically varied.

Finally, additional fundamental studies of partially premixed flames are needed – a number of studies in liquid-fueled aircraft engines have been performed where the flame exists in varying degrees of premixedness, and further understanding of how to interpret such data, and their relationship to perfectly non-premixed and perfectly premixed results is needed.

Acknowledgements

This work has been partially supported by the Department of Energy under contract DE-FE0025174 (contract monitor Seth Lawson) and the National Science Foundation under contracts CBET-1235779 and CBET-1705649 (contract monitor Ruey-Hung Chen).

References

[1] Lieuwen TC. *Unsteady combustor physics*. Cambridge University Press; 2012.
[2] Magina N, Steele W, Emerson B, Lieuwen T. Spatio-temporal evolution of harmonic disturbances on laminar, non-premixed flames: Measurements and analysis. *Combust Flame* 2017;**180**:262–75.
[3] Lieuwen TC, Yang V. Combustion instabilities in gas turbine engines: operational experience, fundamental mechanisms and modeling 2005.

[4] Lieuwen T. *Unsteady combustor physics*. Cambridge Press; 2013.
[5] Lieuwen T. Modeling premixed combustion-acoustic wave interactions: A review. *J. Propuls Power* 2003;**19**:765–81.
[6] Baillot F, Durox D, Prud'Homme R. Experimental and theoretical study of a premixed vibrating flame. *Combust Flame* 1992;**88**(149-52):53–68 IN1.
[7] Huang Y, Yang V. Dynamics and Stability of Lean-Premixed Swirl-Stabilized Combustion. *Prog Energy Combust Sci* 2009;**35**:293–364.
[8] Preetham SH, Lieuwen T. Dynamics of laminar premixed flames forced by harmonic velocity disturbances. *J. Propuls Power* 2008;**24**:1390–402.
[9] Schuller T, Durox D, Candel S. A unified model for the prediction of laminar flame transfer functions: comparisons between conical and V-flame dynamics. *Combust Flame* 2003;**134**:21–34.
[10] Boyer L, Quinard J. On the dynamics of anchored flames. *Combust Flame* 1990;**82**:51–65.
[11] Fleifil M, Annaswamy AM, Ghoneim ZA, Ghoneim AF. Response of a laminar premixed flame to flow oscillations: A kinematic model and thermoacoustic instability results. *Combust Flame* 1996;**106**:487–510.
[12] Matalon M. Flame dynamics. *Proc Combust Instit* 2009;**32**:57–82.
[13] Candel S, Durox D, Schuller T, Palies P, Bourgouin J-F, Moeck JP. Progress and challenges in swirling flame dynamics. *Comptes rendus mecanique* 2012;**340**:758–68.
[14] Candel S, Durox D, Schuller T, Bourgouin J-F, Moeck JP. Dynamics of swirling flames. *Annu Rev Fluid Mech* 2014;**46**:147–73.
[15] Lee JG, Santavicca DA. Experimental diagnostics for the study of combustion instabilities in lean premixed combustors. *J. Propuls Power* 2003;**19**:735–50.
[16] Lee JG, Kim K, Santavicca DA. Measurement of equivalence ratio fluctuation and its effect on heat release during unstable combustion. *Proc Combust Inst* 2000;**28**:415–21.
[17] Palies P, Durox D, Schuller T, Candel S. The combined dynamics of swirler and turbulent premixed swirling flames. *Combust Flame* 2010;**157**:1698–717.
[18] Durox D, Schuller T, Noiray N, Candel S. Experimental analysis of nonlinear flame transfer functions for different flame geometries. *Proc Combust Instit* 2009;**32**:1391–8.
[19] Kornilov VN, Rook R, ten Thije Boonkkamp JHM, de Goey LPH. Experimental and numerical investigation of the acoustic response of multi-slit Bunsen burners. *Combust Flame* 2009;**156**:1957–70.
[20] Giauque A, Selle L, Gicquel L, Poinsot T, Buechner H, Kaufmann P, et al. System identification of a large-scale swirled partially premixed combustor using LES and measurements. *J Turbulence* 2005 N21.
[21] Truffin K, Poinsot T. Comparison and extension of methods for acoustic identification of burners. *Combust Flame* 2005;**142**:388–400.
[22] Shreekrishna HemchandraS, Lieuwen T. Premixed flame response to equivalence ratio perturbations. *Combust Theory Model* 2010;**14**:681–714.
[23] Preetham ThumuluruSK, Santosh H, Lieuwen T. Linear Response of Laminar Premixed Flames to Flow Oscillations: Unsteady Stretch Effects. *J. Propuls Power* 2010;**26**.
[24] Hemchandra S, Peters N, Lieuwen T. Heat release response of acoustically forced turbulent premixed flames—role of kinematic restoration. *Proc Combust Inst* 2011;**33**:1609–17.
[25] Shreekrishna, Lieuwen T. High Frequency Response of Premixed Flames to Acoustic Disturbances. *15th AIAA/CEAS Aeroacoustics Conference Miami, FL*; 2009.
[26] Palies P, Schuller T, Durox D, Candel S. Modeling of premixed swirling flames transfer functions. *Proc Combust Instit* 2011;**33**:2967–74.
[27] Ducruix S, Schuller T, Durox D, Candel S. Combustion instability mechanism in premixed combustors. *Combustion instabilities in gas turbine engines: operational experience, fundamental mechanisms and modeling*. Lieuwen T, Yang V, editors. American Institute of Aeronautics and Astronautics; 2005.
[28] Schuller T, Ducruix S, Durox D, Candel S. Modeling tools for the prediction of premixed flame transfer functions. *Proc Combust Instit* 2002;**29**:107–13.
[29] Acharya V, Emerson B, Mondragon U, Shin D-H, Brown C, McDonell V, et al. Velocity and flame wrinkling characteristics of a transversely forced, bluff-body stabilized flame, Part II: Flame response modeling and comparison with measurements. *Combust Sci Technol* 2013;**185**:1077–97.
[30] Acharya V, Malanoski M, Aguilar M, Lieuwen T. Dynamics of a transversely excited swirling, lifted flame: flame response modeling and comparison with experiments. *J Eng Gas Turbines Power* 2014;**136**:051503.
[31] Matalon M. Intrinsic flame instabilities in premixed and nonpremixed combustion. *Annu Rev Fluid Mech* 2007;**39**:163–91.
[32] Shaddix CR, Harrington JE, Smyth KC. Quantitative measurements of enhanced soot production in a flickering methane/air diffusion flame. *Combust Flame* 1994;**99**:723–32.
[33] Kim T, Ahn M, Hwang J, Kim S, Yoon Y. The experimental investigation on the response of the Burke–Schumann flame to acoustic excitation. *Proc Combust Instit* 2016.
[34] Lingens A, Neemann K, Meyer J, Schreiber M. Instability of diffusion flames. In: *Symposium (International) on Combustion*. Elsevier; 1996. p. 1053–61.
[35] Chamberlin D, Rose A. The flicker of luminous flames. *Industr Eng Chem* 1928;**20**:1013–16.
[36] Buckmaster J, Peters N. The infinite candle and its stability—a paradigm for flickering diffusion flames. In: *Symposium (International) on Combustion*. Elsevier; 1988. p. 1829–36.
[37] Boulanger J. Laminar round jet diffusion flame buoyant instabilities: Study on the disappearance of varicose structures at ultra-low Froude number. *Combust Flame* 2010;**157**:757–68.
[38] Kukuck S, Matalon M. The onset of oscillations in diffusion flames. *Combust Theory Model* 2001;**5**:217–40.
[39] Matalon M, Ludford G, Buckmaster J. Diffusion flames in a chamber. *Acta Astronautica* 1979;**6**:943–59.
[40] Chen Ll-W, Wang Q, Zhang Y. Flow characterisation of diffusion flame under non-resonant acoustic excitation. *Exp Therm Fluid Sci* 2013;**45**:227–33.
[41] Huang HW, Wang Q, Tang HJ, Zhu M, Zhang Y. Characterisation of external acoustic excitation on diffusion flames using digital colour image processing. *Fuel* 2012;**94**:102–9.
[42] Wang Q, Huang HW, Tang HJ, Zhu M, Zhang Y. Nonlinear response of buoyant diffusion flame under acoustic excitation. *Fuel* 2013;**103**:364–72.
[43] Chrystie R, Chung SH. Response to Acoustic Forcing of Laminar Coflow Jet Diffusion Flames. *Combust Sci Technol* 2014;**186**:409–20.
[44] Williams TC, Shaddix CR, Schefer RW, Desgroux P. The response of buoyant laminar diffusion flames to low-frequency forcing. *Combust Flame* 2007;**151**:676–84.
[45] Juniper MP, Li LKB, Nichols JW. Forcing of self-excited round jet diffusion flames. *Proc Combust Instit* 2009;**32**:1191–8.
[46] Li LKB, Juniper MP. Lock-in and quasiperiodicity in hydrodynamically self-excited flames: Experiments and modelling. *Proc Combust Instit* 2013;**34**:947–54.
[47] Saito M, Sato M, Nishimura A. Soot suppression by acoustic oscillated combustion. *Fuel* 1998;**77**:973–8.
[48] Ferreira D, Lacava P, Ferreira M, de Carvalho J,JA. NOx and CO emissions and soot presence in partially premixed acoustically excited flames. *J Energy Instit* 2009;**82**:123–32.
[49] Chung S, Law C. Burke–Schumann flame with streamwise and preferential diffusion. *Combust Sci Technol* 1984;**37**:21–46.
[50] Mohammed RK, Tanoff MA, Smooke MD, Schaffer AM, Long MB. Computational and experimental study of a forced, timevarying, axisymmetric, laminar diffusion flame. In: *Proc Combust Instit*. Elsevier; 1998. p. 693–702.
[51] Siwatch V, Lawrence B, Kuchibhatla S, Annamalai K, Ranjan D. Excess Air, Schmidt Number, and NOx Formation in Laminar Jet Flames. *Combust Sci Technol* 2014;**186**:1936–53.
[52] Lakshminarasimhan K, Ryan MD, Clemens NT, Ezekoye OA. Mixing characteristics in strongly forced non-premixed methane jet flames. *Proc Combust Instit* 2007;**31**:1617–24.
[53] Dworkin S, Cooke J, Bennett B, Connelly B, Long M, Smooke M, et al. Distributed-memory parallel computation of a forced, time-dependent, sooting, ethylene/air coflow diffusion flame. *Combust Theory Model* 2009;**13**:795–822.
[54] Jocher A, Foo KK, Sun Z, Dally B, Pitsch H, Alwahabi Z, et al. Impact of acoustic forcing on soot evolution and temperature in ethylene-air flames. *Proc Combust Instit* 2017;**36**:781–8.
[55] Foo KK, Sun Z, Medwell PR, Alwahabi ZT, Dally BB, Nathan GJ. Experimental investigation of acoustic forcing on temperature, soot volume fraction and primary particle diameter in non-premixed laminar flames. *Combust Flame* 2017;**181**:270–82.
[56] Marr KC, Clemens NT, Ezekoye OA. Mixing characteristics and emissions of strongly-forced non-premixed and partially-premixed jet flames in crossflow. *Combust Flame* 2012;**159**:707–21.
[57] De-Hua C, Ta-Hui L, Shuhn-Shyurng H. Flame synthesis of carbon nano-onions enhanced by acoustic modulation. *Nanotechnology* 2010;**21**:435604.
[58] Hou S-S, Chen K-M, Yang Z-Y, Lin T-H. Enhanced Synthesis of Carbon Nanomaterials Using Acoustically Excited Methane Diffusion Flames. *Materials.* 2015;**8**:4805–16.
[59] Hu W-C, Sari S, Hou S-S, Lin T-H. Effects of Acoustic Modulation and Mixed Fuel on Flame Synthesis of Carbon Nanomaterials in an Atmospheric Environment. *Materials.* 2016;**9**:939.
[60] Kim JS, Williams FA. Contribution of strained diffusion flames to acoustic pressure response. *Combust Flame* 1994;**98**:279–99.
[61] Sohn CH. Unsteady analysis of acoustic pressure response in N2 diluted H2 and air diffusion flames. *Combust Flame* 2002;**128**:111–20.
[62] Welle EJ, Roberts WL, Carter CD, Donbar JM. The response of a propane-air counter-flow diffusion flame subjected to a transient flow field. *Combust Flame* 2003;**135**:285–97.
[63] Dworkin S, Connelly B, Schaffer A, Bennett B, Long M, Smooke M, et al. Computational and experimental study of a forced, time-dependent, methane–air coflow diffusion flame. *Proc Combust Instit* 2007;**31**:971–8.
[64] Hou SS, Chung DH, Lin TH. Experimental and numerical investigation of jet flow and flames with acoustic modulation. *Int J Heat Mass Transfer* 2015;**83**:562–74.
[65] Strawa AW, Cantwell BJ. Visualization of the structure of a pulsed methane–air diffusion flame. *Phys Fluids* 1985;**28**:2317–20.
[66] Lee KM, Kim TK, Kim WJ, Kim SG, Park J, In Keel S. A visual study on flame behavior in tone-excited non-premixed jet flames. *Fuel* 2002;**81**:2249–55.
[67] Hertzberg JR. Conditions for a split diffusion flame. *Combust Flame* 1997;**109**:314–22.
[68] Gore J, Minis I. Acoustically modulated free jet flames. *28th Aerospace Sciences Meeting*. American Institute of Aeronautics and Astronautics; 1990.
[69] Carpio J, Sánchez-Sanz M, Fernández-Tarrazo E. Pinch-off in forced and non–forced, buoyant laminar jet diffusion flames. *Combust Flame* 2012;**159**:161–9.
[70] Jiang J, Jing L, Zhu M, Jiang X. A comparative study of instabilities in forced reacting plumes of nonpremixed flames. *J. Energy Instit* 2016;**89**:456–67.
[71] Sawarkar P, Sundararajan T, Srinivasan K. Effects of externally applied pulsations on LPG flames at low and high fuel flow rates. *Appl Thermal Eng* 2017;**111**:1664–73.

[72] Kim TK, Park J, Shin HD. Mixing Mechanism near the Nozzle Exit in a Tone Excited Non-Premixed Jet Flame. *Combust Sci Technol* 1993;**89**:83–100.
[73] Oh SK, Shin HD. A visualization study on the effect of forcing amplitude on tone-excited isothermal jets and jet diffusion flames. *Int J Energy Res* 1998;**22**:343–54.
[74] Magri L, Juniper MP. Global modes, receptivity, and sensitivity analysis of diffusion flames coupled with duct acoustics. *J Fluid Mech* 2014;**752**:237–65.
[75] Chen L-W, Zhang Y. Experimental observation of the nonlinear coupling of flame flow and acoustic wave. *Flow Measurement Instrum* 2015;**46**:12–17.
[76] Chen S, Zhao D, Li HKH, Ng TY, Jin X. Numerical study of dynamic response of a jet diffusion flame to standing waves in a longitudinal tube. *Appl Thermal Eng* 2017;**112**:1070–82.
[77] Illingworth SJ, Waugh IC, Juniper MP. Finding thermoacoustic limit cycles for a ducted Burke-Schumann flame. *Proc Combust Instit* 2013;**34**:911–20.
[78] Buckmaster J, Clavin P, Linan A, Matalon M, Peters N, Sivashinsky G, et al. Combustion theory and modeling. *Proc Combust Instit* 2005;**30**:1–19.
[79] Buckmaster JD. Edge Flames. *J Eng Math* 1997;**31**:269–84.
[80] Pope S. The evolution of surfaces in turbulence. *Int J Eng Sci* 1988;**26**:445–69.
[81] Law C, Chung S. Steady state diffusion flame structure with Lewis number variations. *Combust Sci Technol* 1982;**29**:129–45.
[82] Chen LD, Seaba J, Roquemore W, Goss L. Buoyant diffusion flames. In: *Symposium (International) on Combustion*. Elsevier; 1989. p. 677–84.
[83] Wang Q, Yang J, Huang HW, Zhang Y, Zhao C. Three-dimensional investigation of the dynamics of a propane diffusion flame. *Fuel* 2014;**116**:448–54.
[84] Delichatsios MA. Air entrainment into buoyant jet flames and pool fires. *Combust Flame* 1987;**70**:33–46.
[85] Delichatsios M. Transition from momentum to buoyancy-controlled turbulent jet diffusion flames and flame height relationships. *Combust Flame* 1993;**92**:349–64.
[86] Farhat S, Kleiner D, Zhang Y. Jet diffusion flame characteristics in a loudspeaker-induced standing wave. *Combust Flame* 2005;**142**: 317–323.
[87] Balasubramanian K, Sujith R. Nonlinear response of diffusion flames to uniform velocity disturbances. *Combust Sci Technol* 2008;**180**:418–36.
[88] Balasubramanian K, Sujith R. Non-normality and nonlinearity in combustion-acoustic interaction in diffusion flames. *J Fluid Mech* 2008;**594**:29–58.
[89] Tyagi M, Chakravarthy S, Sujith R. Unsteady combustion response of a ducted non-premixed flame and acoustic coupling. *Combust Theory Model* 2007;**11**:205–26.
[90] Tyagi M, Jamadar N, Chakravarthy S. Oscillatory response of an idealized two-dimensional diffusion flame: Analytical and numerical study. *Combust Flame* 2007;**149**:271–85.
[91] Magri L, Balasubramanian K, Sujith R, Juniper MP. Non-normality in combustion-acoustic interaction in diffusion flames: a critical revision. arXiv preprint arXiv:13100238. 2013.
[92] Magina N, Shin D-H, Acharya V, Lieuwen T. Response of non-premixed flames to bulk flow perturbations. *Proc Combust Instit* 2013;**34**:963–71.
[93] Magina N, Acharya V, Sun T, Lieuwen T. Propagation, dissipation, and dispersion of disturbances on harmonically forced, non-premixed flames. *Proc Combust Instit* 2015;**35**:1097–105.
[94] Miklavčič M, Wichman IS. Theoretical and numerical analysis of oscillating diffusion flames. *Combust Flame* 2016;**173**:99–105.
[95] Magina NA, Lieuwen TC. Effect of axial diffusion on the response of diffusion flames to axial flow perturbations. *Combust Flame* 2016;**167**:395–408.
[96] Magina N, Lieuwen T. *Response of over-ventilated non-premixed flames to transverse flow perturbations*. Eastern States Section of the Combustion Institute; 2013.
[97] Peters N. *Turbulent combustion*. 1 ed. Cambridge University Press; 2000.
[98] Do Carmo MP, Do Carmo MP. *Differential geometry of curves and surfaces*. Prentice-hall Englewood Cliffs; 1976.
[99] Ducruix S, Schuller T, Durox D, Candel S. Combustion dynamics and instabilities: Elementary coupling and driving mechanisms. *J. Propuls Power* 2003;**19**:722–34.
[100] Kollmann W, Chen J. Dynamics of the flame surface area in turbulent non-premixed combustion. In: *Symposium (International) on Combustion*. Elsevier; 1994. p. 1091–8.
[101] Markstein G. *Nonsteady flame propagation: published for and on behalf of advisory group for aeronautical research and development*. Pergamon Press; 1964. North Atlantic Treaty Organization by.
[102] Williams FA. *Combustion theory*. 2nd ed. Ca: Benjamin: Cummings Publishing Co.; 1985. Menlo Park.
[103] Menon S, Jou W-H. Large-eddy simulations of combustion instability in an axisymmetric ramjet combustor. *Combust Sci Technol.* 1991;**75**:53–72.
[104] Burke S, Schumann T. Diffusion flames. *Industr Eng Chem* 1928;**20**:998–1004.
[105] Preetham T, Sai K, Santosh H, Lieuwen T. Linear Response of Laminar Premixed Flames to Flow Oscillations: Unsteady Stretch Effects. *J. Propuls Power* 2010;**26**:524–32.
[106] Magina N. Dynamics of Harmonically Forced Non-premixed Flames (PhD Thesis). Georgia Institute of Technology. 2016.
[107] Magina N, Acharya V, Lieuwen T. *Response of non-premixed flames to bulk flow perturbations*. Eastern States Section of the Combustion Institute; 2011.
[108] Shin D, Shanbhogue S, Lieuwen T. Premixed flame kinematics in an axially decaying, harmonically oscillating vorticity field, 44th AIAA/ASME/SAE/ASEE Joint Propulsion Conference & Exhibit. 2008.
[109] Li Y-Q, Cao H-L, Zhou H-C, Zhou J-J, Liao X-Y. Research on dynamics of a laminar diffusion flame with bulk flow forcing. *Energy.* 2017;**141**:1300–12.
[110] Wang HY, Law CK, Lieuwen T. Linear Response of stretch-affected premixed flames to flow oscillations. *Combust Flame* 2009:889–95.
[111] Magina N, Lieuwen T. Three-dimensional and swirl effects on harmonically forced, non-premixed flames. *9th US National Combustion Meeting*; 2015.
[112] Acharya VS, Shin D-H, Lieuwen T. Premixed flames excited by helical disturbances: Flame wrinkling and heat release oscillations. *J. Propuls Power* 2013;**29**:1282–91.
[113] Acharya V, Shin D-H, Lieuwen T. Swirl effects on harmonically excited, premixed flame kinematics. *Combust Flame* 2012;**159**:1139–50.
[114] Kaplan CR, Shaddix CR, Smyth KC. Computations of enhanced soot production in time-varying CH 4/air diffusion flames. *Combust Flame* 1996;**106**:392–405.
[115] Crocco L, Cheng S-I. *Theory of combustion instability in liquid propellant rocket motors*. Cambridge Univ Press; 1956.
[116] Katta V, Goss L, Roquemore W. Effect of nonunity Lewis number and finite-rate chemistry on the dynamics of a hydrogen-air jet diffusion flame. *Combust Flame* 1994;**96**:60–74.

Dr. Nicholas Magina received his PhD in Aerospace Engineering at the Georgia Institute of Technology in 2016. His expertise is in combustion instabilities, non-premixed flames, and thermo-acoustic wave interactions. He works as a Research Engineer at General Electric Corporate Research in the Thermosciences team.

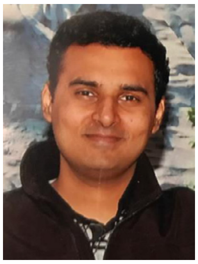

Dr. Vishal Acharya is a Research Engineer in the School of Aerospace Engineering at Georgia Institute of Technology. He works in the Aerospace Combustion Lab where he performs computational and mathematical modeling of unsteady combustion phenomena.

Dr. Tim Lieuwen is a Regents Professor, holder of the David S. Lewis, Jr., Chair in the School of Aerospace Engineering and the Executive Director of the Strategic Energy Institute at Georgia Tech. His research activities involve both theoretical and experimental work in combustion, flame-acoustic wave interactions, combustion noise, and turbulent combustion. Prof. Lieuwen is an elected member of the National Academy of Engineering, a Fellow of the ASME and AIAA, and has been a recipient of the AIAA Lawrence Sperry Award and the ASME Westinghouse Gold Medal.